Structural Dynamics of the Myosin Force-generating Region

A DISSERTATION
SUBMITTED TO THE FACULTY OF THE GRADUATE SCHOOL
OF THE UNIVERSITY OF MINNESOTA
BY

Roman Agafonov

IN PARTIAL FULFILLMENT OF THE REQUIREMENTS
FOR THE DEGREE OF DOCTOR OF PHILOSOPHY

David D. Thomas, advisor

December 2009

Acknowledgments

It has been said **"**Thou shall not make for yourself an idol", but there is an exception to every rule, and I was lucky enough to meet such an exception. Throughout my graduate training my advisor, **David Thomas**, provided me not only with guidance, but also with an example of a scientist and a person that I would like to become one day. His unique mentoring style contributed a lot to my development and led to many achievements including the work behind this dissertation.

My graduate school experience would undoubtedly be much less cheerful and productive without unwavering support from **Yuri Nesmelov**, whose optimism, creativity and scientific expertise strengthened my motivation and powered my research. Analytical thinking and secrets of EPR spectroscopy, which I learned from him, will remain my strongest skills for the rest of my life.

I appreciate the help from **Margaret Titus** and **Sarah Blakely**, whose tireless efforts to make a molecular biologist out of a Russian physicist significantly broadened my horizon and, perhaps, even prevented me from making a wrong turn in my scientific career. I am grateful to **Igor Negrashov**, whose engineering talent made possible most of my experiments, and whose critical mind has served me as a rare example of truly logical thinking. I thank **Ewa Prochniewicz** and **Piyali Guhathakurta**, who were always willing to share their actin and even the "know-how" of making it. I also thank **Luke Olson**, **Valerie Haug**, **Erin Hoffman**, **Benjamin Matzke, Eunice Song** and **Christina Yi** for excellent technical assistance and help with protein preparation.

For as long as I have known **David Kast**, he has been an irreplaceable source of knowledge and all the facts I ever wanted to know. His encyclopedic brain saved me from many pitfalls and troubles. I enjoyed my prolonged scientific discussions with **Joe Muretta**, whose affection for science and inclination to unconventional thinking have impressed me profoundly. Exemplarily organization and people skills of **Octavian Cornea** greatly simplified my life and were a source of my admiration for several years.

I will always remain grateful to **Jenny Klein** for her invaluable lessons on biochemistry and life that made me a more evolved human being. I have not met any other person with such a balanced view of the world, and I will never give up my attempts to achieve the same level.

I truly enjoyed working with **Zach James,** whom I most likely would confuse with a Russia-born person, if it wasn't for his ability to casually use unpronounceable 8-syllable English words.

A special thanks to **Ryan Mello** for help with spectra analysis and spiritual guidance. If it wasn't for Ryan, I would never learn that it is possible to use ten different words to identify a cookie, and would be stuck with mushy and tasteless microwaved pop-tarts for the rest of my life.

I enjoyed the company of **Robyn Stoller**, whose openness and sense of humor often made the biochemistry lab a brighter place.

Dedication

T. E., T. M. A. G. I. T. W.,
F. W. I. L. S. M.

Abstract

Myosin is a molecular motor that generates force on actin using energy from ATP hydrolysis. Myosin plays a key role in muscle contraction and is responsible for a variety of motility processes at the cellular level. It works cyclically, changing its conformation during the power stroke and the recovery stroke. X-ray crystallography has provided information about the structural organization of myosin in different biochemical states (as defined by bound nucleotide), inspiring several structural models that could explain the molecular mechanism of myosin's function. Spectroscopy, in combination with site-directed labeling and transient experiments, can test and refine these models and provide information about myosin's dynamic properties (1).

The goal of this project was to determine the structural dynamics of the myosin force-generating domain and study coupling mechanisms between this domain and the myosin active site. We have chosen *Dictyostelium discoideum* (*Dicty*) as our experimental system since it provides multiple advantages in comparison with the muscle myosin. In particular, it is possible to manipulate the *Dicty* DNA sequence, engineering labeling sites at desired locations and introducing functional mutations at the points of interest. As a first part of the project, we have tested *Dicty* myosin in comparison with myosin purified from rabbit skeletal muscle, and have shown that structural changes in the force-generating domain of *Dicty* and rabbit myosin are identical. We then focused on specific elements within the force-generating domain, relay helix and relay loop, as these elements appeared to be crucial for interdomain coupling and force generation. Using time-resolved EPR and FRET, we have developed a spectroscopic approach to determine the conformation of the relay helix. We have also developed a novel technique that we called transient time-resolved FRET [$(TR)^2$FRET], which allowed us to monitor structural changes within the relay helix in real time. We then studied the relationship between the state of the myosin active site (which is determined by the bound ligand) and the structure of the relay helix. To obtain insights about regulatory mechanisms, we have investigated the effect of a mutation that is known to abolish myosin motor function, despite leaving enzymatic activity intact. These experiments revealed important coupling mechanisms between the relay loop and relay helix, providing a structural explanation for

the previously observed functional effects and a model for power stroke activation in myosin.

Table of contents

List of Tables.

List of Figures

List of Abbreviations

A, actin
ADP, adenosine diphosphate
ADP.V, ADP and vanadate
AlF, aluminum fluoride (AlF_4^-)
BeF, beryllium fluoride
ATP, adenosine triphosphate
CW-EPR, continuous wave EPR
DABCYL, 4 - ((4 - (dimethylamino)phenyl)azo)benzoic acid
DEER, diploar electron-electron resonance
Dicty, *Dictyostelium discoideum*
EGTA, ethyleneglycol-bis-(2-aminoethyl ether)*N*,*N*,*N*,*N*-tetraacetic acid
EPR, electron paramagnetic resonance
FRET, fluorescence resonance energy transfer
FWHM, full width at half maximum of Gaussian distribution of distances
IADEANS, 5-((((2-iodoacetyl) amino) ethyl) amino) naphthalene-1-sulfonic acid
IASL, iodoacetamideTEMPO spin label
IRF, Instrument Response Function
L50k, Lower 50 kDa domain
MD, computational molecular dynamics
MSL, N-(1-oxy-2,2,5,5-tetramethyl-4-piperidinyl)maleimide
P_i, inorganic phosphate
PDB, protein data bank
R_0, Förster distance
RMSF, root mean square fluctuation
S1, subfragment 1 of muscle myosin
S1dC, subfragment 1 of *Dictyostelium* myosin II
SDSL, site-directed spin labeling
TR-FRET, time-resolved fluorescence resonance energy transfer,
T_1, spin lattice or longitudinal relaxation time
T_2, spin-spin or transverse relaxation time
U50, Upper 50 kDa domain
WT, wild-type

Chapter 1. Introduction.

1.1 Myosin.

The capacity for self-propelled movement is one of the key features that distinguish living beings from non-living. Remarkably, muscle contraction in the human body, movement of single-cell organisms and even motion of cellular components is often facilitated by the same protein: myosin. Myosin is a molecular motor that produces mechanical work on actin using energy from ATP hydrolysis. The myosin family consists of many members; in this work we focus on myosin II, which accounts for all myosin involved in muscle contraction, as well as a wide range of nonmuscle functions.

1.1.1 Acto-myosin ATPase cycle

In its cyclic interaction with actin, myosin undergoes structural changes that result in propulsion of actin filaments. A widely accepted model depicting the essential steps of the actomyosin ATPase cycle is illustrated in **Fig. 1** (1). The key step is the ***power stroke*** (top), in which the release of phosphate from myosin triggers the transition from a weakly bound state (bent myosin head, upper left) to a strongly bound state (straight head, upper right), moving actin toward the center of the sarcomere. ATP greatly decreases myosin affinity for actin (lower right), and ATP hydrolysis induces the ***recovery stroke***, changing myosin conformation back to the bent state (lower left), an energized conformation in which myosin is ready to perform work. The cycle is complete when this state binds to actin, in preparation for the next power stroke.

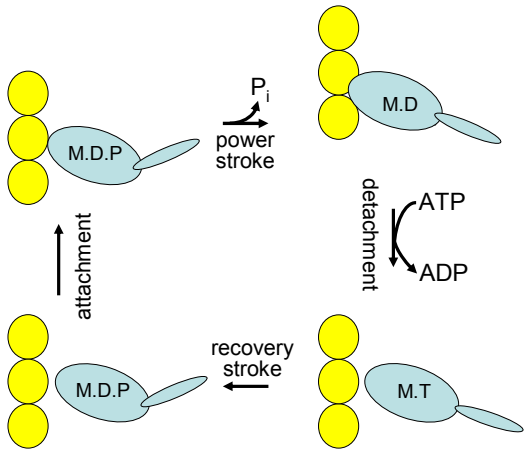

Fig. 1. Schematic representation the of acto-myosin cycle. Yellow: actin. Blue: myosin head, T - ATP, D -ADP, P_i-inorganic phosphate.

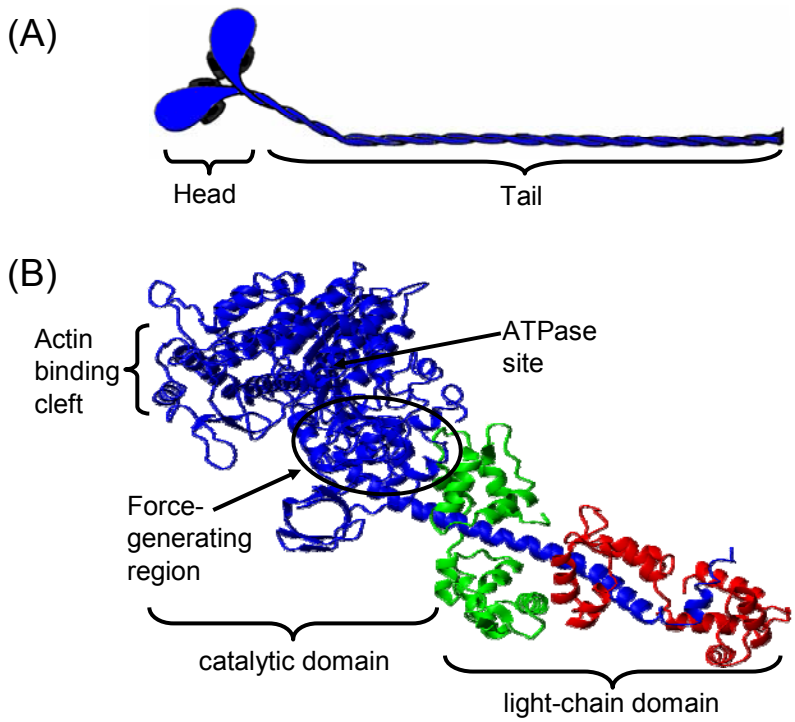

Fig. 2. Structure of myosin II.
(A): Schematic representation of myosin, consisting of two heads and a long tail; (B): Crystal structure of the myosin head, S1 (2), consisting of the heavy chain (blue) and two light chains (green and red).

1.1.2 Myosin structure.

Although during the acto-myosin interaction both proteins change structure (3), the leading role in force generation belongs to myosin, with actin serving as a responsive load. Each myosin molecule consists of two structurally distinct regions: an N-terminal "head" (also known as motor domain or S1) and a C-terminal "tail" (**Fig. 2A**). The head is a fully functional actin-activated ATPase that can move actin in in-vitro motility assays, and in complex with actin it is often considered as a minimal model for muscle (4).

The first crystal structure of myosin motor domain was solved by Rayment and coworkers in 1993 (2). It revealed key elements of the myosin structure and provided the basis for understanding its function on the submolecular level. The head is composed of one heavy chain and two light chains, and structurally can be divided into two regions: the catalytic domain and the light-chain domain (**Fig. 2B)**. The catalytic domain contains all the key elements of the structure (e.g. actin-binding site, ATP-binding site), and the

primary function of the light-chain domain, often referred to as “lever arm”, is to amplify conformational changes in the catalytic domain increasing the size of the power stroke. Phosphorylation of the light chains can play a regulatory role in some myosin isoforms.

1.1.3 Myosin catalytic domain.

Within the catalytic domain, several subdomains responsible for specific function have been identified (**Fig. 3**). Upper and lower 50k domains form the so called actin-binding cleft, which is responsible for acto-myosin interaction. This cleft undergoes open-to-closed transitions (5), which affect myosin affinity for actin and result in acto-myosin binding and dissociation throughout the cycle (**Fig. 2**). Switch I, switch II and the P-loop form the nucleotide-binding pocket (**Fig. 3**, yellow) and are responsible for interaction with nucleotide. In a catalytically active state, both switch I and II are closed and several hydrophobic bonds are formed. Gly457 and Phe458 of switch II form a bond with an oxygen atom of the γ-phosphate and Ser181 of the P-loop, respectively, and Glu459 coordinates a water molecule that attacks ATP, enabling hydrolysis (6-8). The relay helix (**Fig. 3**, red), relay loop (**Fig. 3**, red) , SH1-SH2 helices (**Fig. 3**, blue) and the converter domain (**Fig. 3**, green) form the force-generating region and are involved in communication between the active site and the lever arm. The N-terminus of the relay helix is a continuation of switch II and at its C-terminus interacts with the converter through a number of hydrophobic residues. The converter is covalently bound to the light-chain domain and controls its motion during the recovery and power strokes. The relay loop originates from the C-terminus of the relay helix and goes back to the lower 50k domain, providing coupling

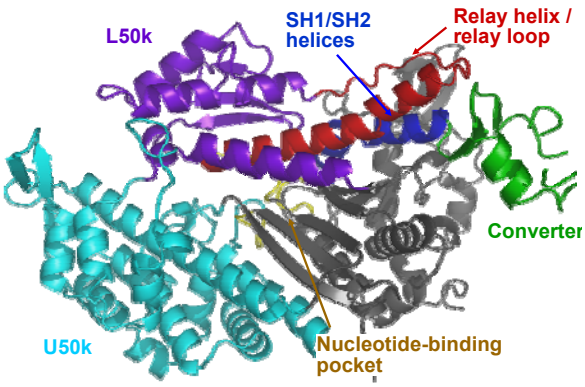

Fig. 3: Structure of the myosin catalytic domain (pdb: 1VOM).
The upper 50kD domain (cyan) and lower 50kD domain (purple) are responsible for actin binding. The nucleotide-binding site (yellow) is involved in ATP binding and hydrolysis. The relay helix (red), the SH1 helix (blue) and the converter domain are parts of the force-generating region that transmit information from the nucleotide-binding site to the light-chain domain (not shown).

with actin-binding elements of the structure. SH1-SH2 helices are located at the myosin "fulcrum point" and according to molecular dynamics simulations (8, 9) push the converter domain during the recovery stroke.

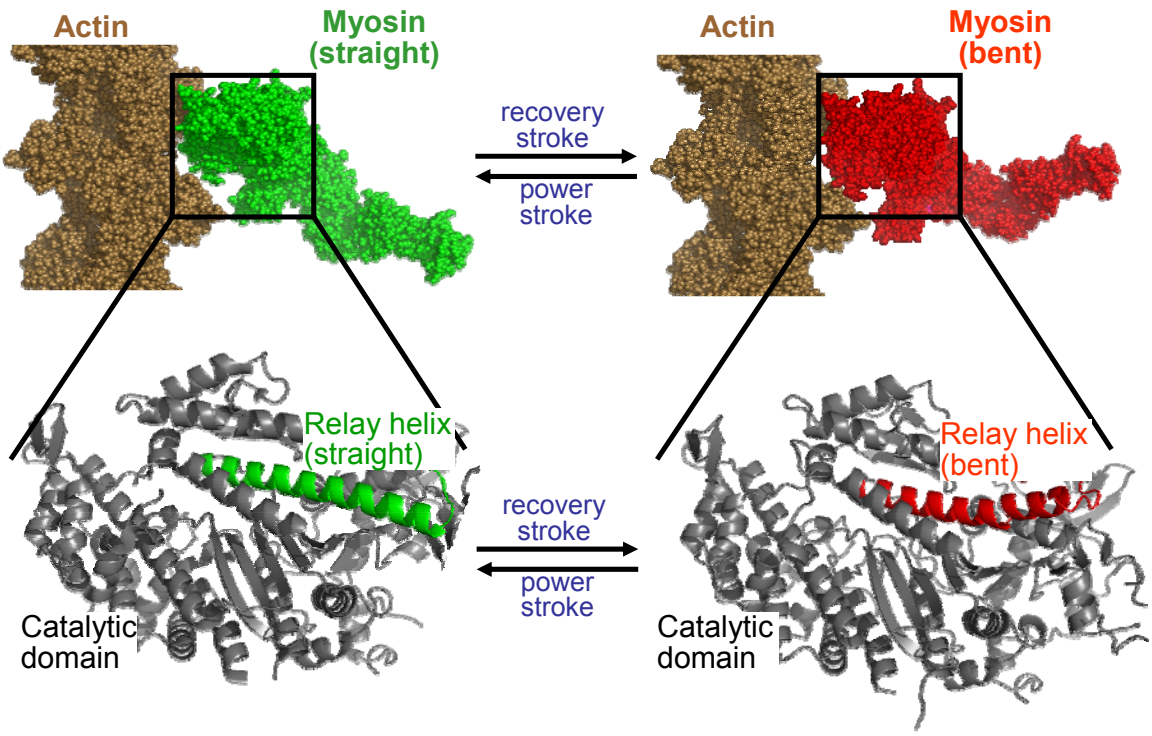

Fig. 4: Acto-myosin complex (top) and myosin catalytic domain (bottom) in the pre- and post-recovery states.
Myosin (top) appears straight in the pre-recovery (left) and bent in the post-recovery (right) state. Transition between the two states corresponds to the recovery (from left to right) and the power (right to left) strokes Myosin bending is recapitulated in the shape of the relay helix that also appears bent and straight (bottom).

1.1.4 Interdomain coupling.

One of the most intriguing questions that remains unanswered is how changes from the ATP-binding pocket propagate throughout the myosin head and result in the swing of the lever arm (**Fig. 4, top**). It has been proposed that the relay helix (Fig. 3, red) plays a key role in communication between the nucleotide pocket and the lever arm (through the converter), since this helix is straight in the apo ("pre-recovery") crystal structure 1FMV (**Fig. 4B, green**), and the helix is bent in the ADP.V ("post-recovery") crystal structure 1VOM (**Fig. 4B, red**). This remarkable correlation between the structure of the whole myosin head and the structure of the relay helix (**Fig. 4**, compare structures

on the left and on the right) provides strong support for the hypothesis, but it needs to be validated by assays capable of detecting structural changes in the relay helix in solution in response to nucleotide binding and dissociation. In addition, the proposed bending of the helix needs to be considered in the context of other structural changes in myosin (e.g. nucleotide pocket closure) and the sequence of structural transitions needs to be established to elucidate cause and effect relationships within the myosin motor.

Mutational analysis has provided valuable information about myosin domain interactions. The Spudich group created a double cysteine mutant with one cysteine located at the C-terminal end of the relay helix (position 499) and another cysteine within the converter domain (position 738) (**Fig. 5**) (10). Disulfide cross-linking of these cysteines created a covalent bond between the relay helix and the converter, presumably forcing them to move together. This cross-linking had minimal effects on acto-myosin interaction (rates of binding and dissociation) and actin-activated ATPase activity. These experiments demonstrated that the relay-converter interface remains intact throughout the myosin ATPase cycle. However, experiments by Sutoh and coworkers (11) showed that mutation of the same residue (I499) into alanine resulted in a marked increase of the basal ATPase activity (activity in the absence of actin) and complete loss of myosin motor functions. Interestingly, the F692A mutation (within the SH1 helix, **Fig. 5**) had a very similar effect, highlighting the importance of hydrophobic interactions between the converter, the relay and SH1-SH2 helices. The Manstein group came to a similar conclusion, analyzing F506A and F506G substitutions within the relay loop (**Fig. 5**). Myosin with these mutations also could not support multicellular development or move actin filaments (12).

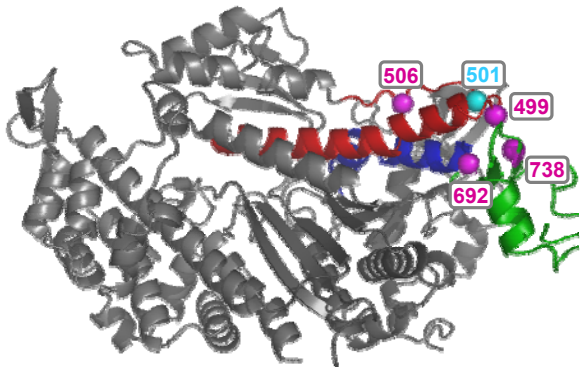

Fig. 5: Known important residues of the myosin force-generating region.
Magenta – functionally important amino acids identified in the previous mutagenesis studies, cyan – tryptophan 501 used to monitor conformation of the force-generating region. Red - the relay helix and relay loop, blue - the SH1 helix, green - converter domain.

Mutational analysis identified many important interactions within the myosin catalytic domain, but could not provide structural information. Solution experiments that could detect structural changes in different domains are required for additional insights (1). Early kinetic experiments in the 1970s (14, 15) showed that intrinsic tryptophan (Trp) fluorescence of myosin changes as myosin goes through the ATPase cycle. These observations were used to detect structural transitions and estimate their rates. A similar approach was exploited by Malnasi-Csizmadia and colleagues, who engineered a *Dicty* myosin mutant with a single Trp501, located at the relay loop – relay helix junction (Fig. 5). Upon binding of ADP and during the initial phases of ATP binding, myosin fluorescence decreased by about 5%, but during steady-state ATP hydrolysis, fluorescence increased by ~15-20% (16). These experiments revealed that during ATP hydrolysis, significant structural changes take place in the local area around Trp501, but they provided no direct structural information about the relay helix and other elements of the structure, since Trp fluorescence is affected by many factors (solvent accessibility, local electric fields, etc) and can not be used to define a specific conformational change. A different approach was used by Suzuki et al (13). They engineered a *Dicty* construct with green fluorescent protein (GFP) attached to the N-terminus of the catalytic domain and blue fluorescent protein (BFP) attached to the converter domain (**Fig. 3**) and observed a decrease in the efficiency of fluorescence resonance energy transfer between these two proteins after addition of ATP or ADP.P_i analogs. These experiments supported the idea that conformational changes within the catalytic domain result in the converter rotation, which then can be transmitted to the lever arm. But, again, these experiments could not provide the structural resolution necessary to identify structural transitions of individual

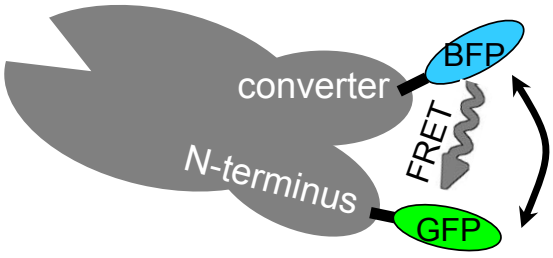

Fig. 6: *Dicty* myosin chimera with introduced blue (BFP) and green (GFP) fluorescent proteins. Decrease in FRET efficiency observed after addition of nucleotide analogs showed movement of the converter domain away from the myosin N-terminus. (Adapted from (13)).

parts of the catalytic domain - information necessary for elucidating the mechanism of energy transduction in myosin.

1.1.5 Biochemical and structural states of myosin

Another open question in the myosin field is the relationship between the biochemical state of the myosin (defined by the bound ligand) and its structural state (defined by the 3D arrangements and motions of atoms). According to the classic Lymn-Taylor model, these two states are tightly coupled -- any structural change corresponds to a change in the occupant of the active site (nucleotide binding, hydrolysis or dissociation) (**Fig. 1**). This idea is supported by most crystal structures, which can be roughly divided into two classes. In the first class, obtained with ADP.P_i analogs, the nucleotide pocket is closed and the force-generating domain is in the post-recovery state (relay helix is bent, converter is up). The second class of structures, obtained with ATP analogs, shows an open nucleotide pocket and the force-generating region is in the pre-recovery state (relay helix is straight, converter is down). These observations suggest that there is a direct correlation between the nature of the bound nucleotide and myosin structure. However, crystal structures in both classes have been reported with a bound ATP analog, ADP.BeF_x, supporting an alternative "loose-coupling" hypothesis, in which multiple conformations (structural states) can coexist in solution in the presence of a single nucleotide (biochemical state) (1). This idea is supported by experiments with spin-labeled ADP and nucleotide analogs (17), which showed that the nucleotide pocket can be in equilibrium between open and closed structural states when a single nucleotide is bound. Similarly, distance and accessibility measurements performed at the actin-binding cleft revealed an equilibrium between the open and the closed state of the actin-binding cleft (5). These solution experiments suggest that there is not a direct correlation between the bound nucleotide and the structure of myosin.

The relationship between myosin biochemical and structural states is reminiscent of a broader question raised by two somewhat competing models of protein-ligand interactions, often referred to as "conformational selection" and "induced fit". For many years these models remained a source of speculation in enzymology and chemical biology. In the most simplistic form, the essence of the question is what happens first: "a

protein adopts a suitable conformation to which a ligand can later" or "ligand binds first, forcing protein to adopt a specific conformation". The latter model treats a protein like a mechanical machine that switches between different conformations depending on external factors, while the former model considers proteins as a "soft material" that can sample multiple conformations around the average structure, and conformational transitions are determined by the multidimensional energy landscape, which is affected but not defined entirely by the ligand (18). Thus understanding mechanisms that govern structural transitions in myosin, for instance answering the question whether or not ATP hydrolysis is required for myosin to adopt a "closed" (post-recovery state) conformation, has significant implications for our understanding of fundamental principles of enzymes functioning.

1.1.6 Research goals.

The goal of this project was to combine molecular biology, spectroscopic and transient kinetics techniques to gain insights into the molecular mechanisms of myosin function. The focus of the work was the myosin force-generating region and its coupling with the myosin active site. Previous spectroscopic studies have shown dramatic structural changes in the force-generating region during ATPase cycle, but failed to identify structure of individual elements and establish interaction mechanism between them. In this work we have used *Dicty* myosin as a muscle myosin analog. We provided evidence that structure of the force-generating region of these two isoforms is virtually identical (Chapter 2). We then developed an approach that allowed us to determine the structure of a single myosin subdomain. Using this approach, we determined the structure of the relay helix as a function of bound nucleotide (Chapter 3) and using the stopped-flow technique we observed relay helix structural transitions after rapid mixing with ATP in real time (Chapter 4). Finally, by studying myosin functional mutation, we proposed a mechanism for the observed uncoupling of myosin motor and enzymatic functions, establishing the importance of the relay helix – relay loop interaction and suggesting the possible role of the relay loop in regulation of force generation (Chapter 5).

1.2. Electron paramagnetic resonance (EPR).

1.2.1 Basic principles of EPR spectroscopy.

EPR (electron paramagnetic resonance) spectroscopy is a technique that detects unpaired electrons in chemical compounds, biomolecules and macromolecular complexes. EPR was first observed by Y. Zavoisky in Kazan, Russia, in 1944, and is based on the Zeeman effect. If an electron is placed in a static magnetic field, the degeneracy in the electron's state is lifted, producing two states with different energies **(Fig. 7).** If an additional oscillating electromagnetic field with the frequency matching the energy gap between the states **(Eq. 1)** is applied, it will stimulate transitions between the low- and high-energy states and result in the absorption of applied electromagnetic power. This absorption can be detected yielding information about the spins and their environment.

$$h\nu = g\beta H_0 \qquad \textbf{Eq. 1}$$

where h is a Plank's constant, ν – frequency of the electromagnetic filed, g – electron g-factor, β - Bohr magneton, and H_0 is the value of the static magnetic field.

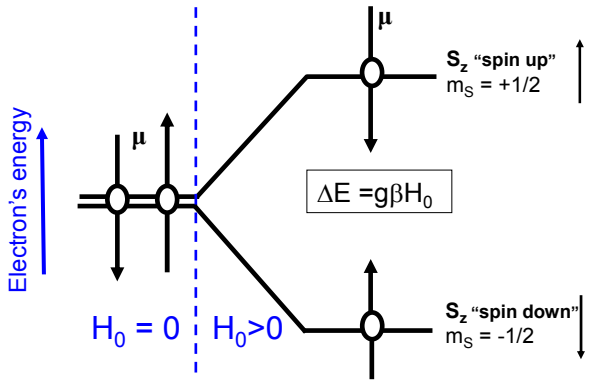

Fig. 7. Splitting of the electron's energy levels in a static magnetic field.
Static magnetic field creates two population of spins, aligned and counter-aligned with the field, that have smaller and higher energy level respectively. This creates an energy gap between the two possible electron states. (Adapted from (19))

Local fields, generated by the electron's environment, further reduce the degeneracy of the electron's state and create additional energy levels. In case of the nitroxide probes, used in the most biological studies, the largest effect is due to the magnetic moment of nitrogen nucleus (with nuclear spin of one), which splits each

original energy level into three new levels (**Fig. 8**). This effect is known as hyperfine splitting. Transitions, stimulated by the applied electromagnetic field, must obey the selection rules, which dictate that the spin of the nitrogen nucleus can not change during the electron transition. Consequently, there are only three "allowed" transitions between the six existing states, and they give rise to a 3-component EPR spectrum (**Fig. 8**).

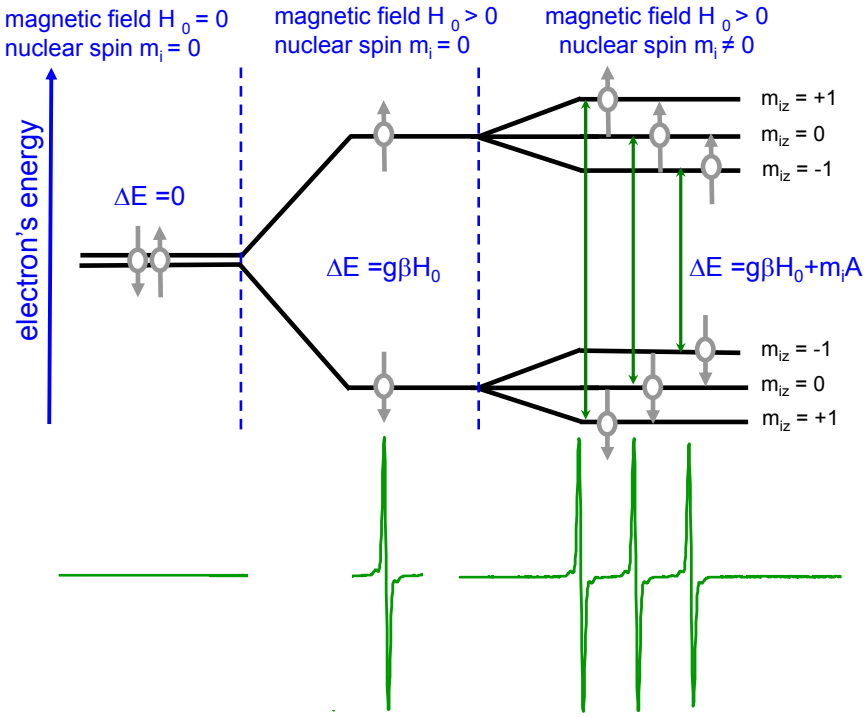

Fig. 8. Hyperfine splitting of EPR spectra.
Local magnetic field generated by nitrogen nucleus of nitroxide spin labels splits the original energy levels into three, giving rise to a three-component EPR spectrum

The Hamiltonian that describes the behavior of the spin label unpaired electron can be written as

$$H = g\beta H_0 + m_i A\,, \qquad \textbf{Eq. 2}$$

where m_i is the nuclear spin quantum number, and A is the energy of the hyperfine interaction. The first term in the Hamiltonian describes the interaction of the electron with the external magnetic field, and the second term is due to the interaction of the electron with magnetic momentum of the nitrogen nucleus. Both g and A depend on orientation of the spin label with respect to the external magnetic field providing sensitivity of EPR spectra to the protein and spin label orientation.

1.2.2 EPR sensitivity to protein orientation and dynamics.

The asymmetry of the π-orbital, which contains most of the unpaired electron spin density in a nitroxide spin label (**Fig. 9A**), leads to angular dependence of *g* and *A* values and orientational dependence of the EPR spectrum. Spin label orientation is usually expressed in polar coordinates (**Fig. 9B**) with *x*-axis aligned with N-O bond and *y*-axis going through the plane of the aromatic ring. The label's orientation affects the position of the spectrum center: hν/[g(θ,ϕ)ß], and the splitting between the lines of the spectrum: A(θ,ϕ)/[g(θ,ϕ)ß]. When the magnetic field is oriented parallel to the z axis, the splitting is greatest and the center is shifted to the right; when field is oriented along X axis splitting becomes smaller and all peaks are shifted to the left (**Fig. 9C**).

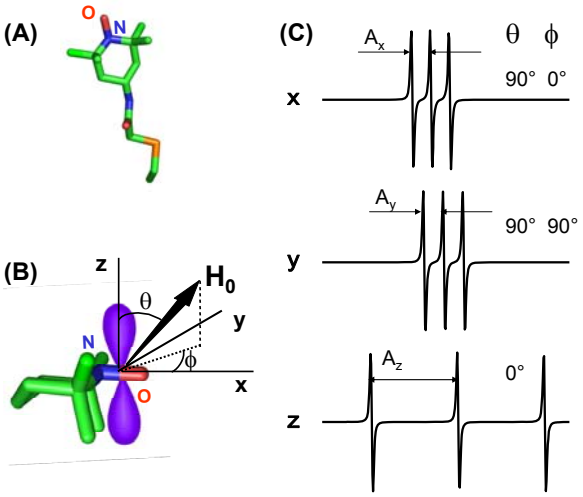

Fig. 9. Orientational sensitivity of EPR spectra. **(A)** Nitroxide spin label; **(B)** Fragment of the spin label and angles that define its orientation with respect to the external magnetic field; **(C)** EPR spectra of the nitroxide spin label for magnetic field parallel to x, y and z axis of the label.

Most biological systems are not perfectly oriented. Fortunately EPR spectra provide information not only about orientation of the sample, but also about the amount of disorder present in the system (**Fig. 10**). Spectrum (A) corresponds to the spin label oriented at the fixed angle with respect to the magnetic field, spectrum (B) – to the label that can fluctuates within a small cone (cone angle ~5º) and spectrum (C) represents a

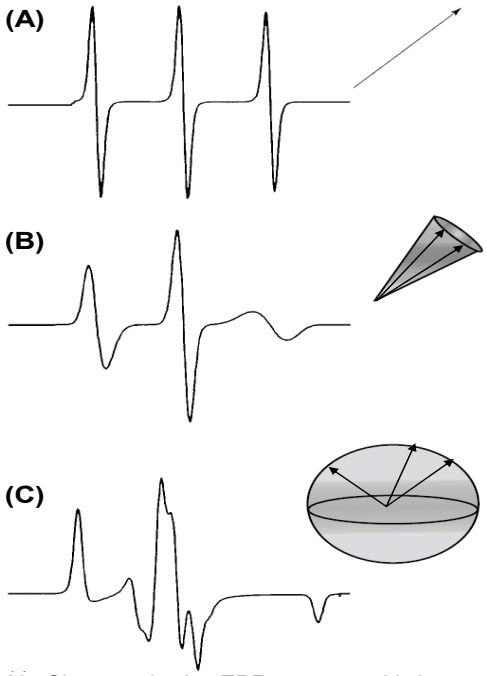

Fig. 10. Changes in the EPR spectra with increasing static disorder. **(A)** ordered system; **(B)** low degree of disorder, and **(C)** completely disordered system

completely disordered system with random orientation of the label. A change in EPR spectra is a consequence of *A* and *g* angular dependence. In a completely ordered system all spins have the same direction relative to the magnetic field and, consequently, have the same value of *g* and *A,* thus experiencing resonance at the same value of H_0. In disordered systems a variety of orientations is available for the spin label, and every orientation is associated with its own *g* and *A*. As a result, the spectrum is a superposition of a large number of spectra that are centered at different values of magnetic field and have different splittings between peaks.

Apart from orientational sensitivity, EPR is also sensitive to the motion dynamics. Depending on the rate of motion three different regimes can be defined: fast ($\tau_c \sim 10^{-11}$-10^{-9}), slow ($\tau_c \sim 10^{-9}$-10^{-7}) and very slow ($\tau_c > 10^{-7}$), where τ_c is the rotational correlation time. These regimes are chosen in comparison with the average life-time of the exited state, which in the case of biological samples is usually determined by the spin-spin relaxation (~10ns). Typical EPR sample (such as the isolated spin-labeled protein in solution) contains labels with all possible orientations and in the absence of motion would give spectrum similar to the one on **Fig. 10C**, but the label's motion partially or completely averages values of the *g*-factor and values of hyperfine splitting *A*. As a result of this averaging, peaks become more narrow and move toward the center of the spectrum, and, in the limit of the very fast motion, spectrum has lineshape typical for a single probe with $g = \frac{1}{3}(g_x + g_y + g_z)$ and

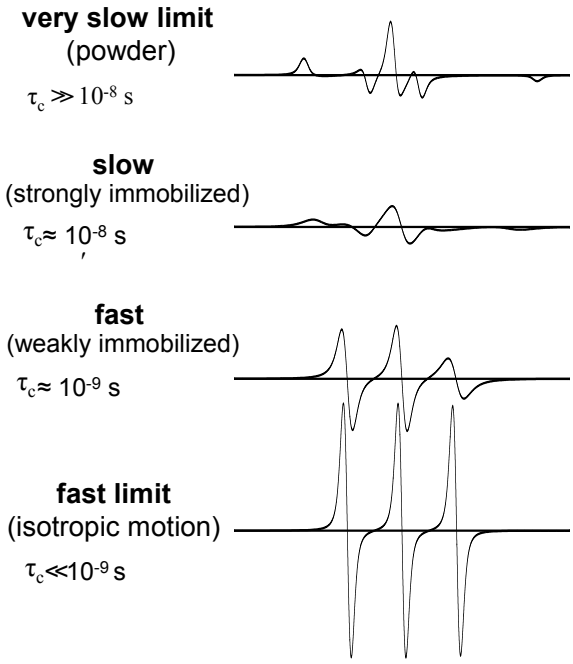

Fig. 11. Effect of rotational dynamics on EPR line-shape.
With an increased rate of motion (decrease in rotational correlation time) values of *g* and *A* become more and more averaged, and in the limit of very fast motion produce a 3-component EPR spectrum with $g=1/3(g_x+g_y+g_z)$ and $A=1/3(A_x+A_y+A_z)$

$A = \frac{1}{3}(A_x + A_y + A_z)$. **Fig. 11** shows changes in EPR spectrum as rate of motion increases from the very slow or no motion (in frozen samples) to fast isotropic motion.

1.2.3 Simulation of EPR spectra

EPR sensitivity to both orientation and dynamics makes it a powerful experimental tool, but at the same time, it considerably complicates data analysis, since contribution from both effects should be taken into account. Some information can be extracted from EPR spectra by directly measuring parameters of the spectrum (line width, amplitude of the components, etc). A better approach is to simulate the spectrum and then fit it to the experimental one. Unfortunately, due to the many factors contributing to the line-shape the exact mathematical equation that could describe the spectrum does not exist, making EPR spectra simulations a nontrivial problem, so some approximations need to be made.
As discussed above, **Eq. 3** defines the resonance value of the magnetic field.

$$H_{res} = \frac{h\nu - m_i A}{g\beta}, \qquad \textbf{Eq. 3}$$

In real systems due to relaxation processes, variation of local magnetic field within a sample and other factors every peak in EPR spectrum gets broadened, and, in the first approximation, the EPR line-shape can be described by the first derivative of the Lorentzian line:

$$Y(H) = \frac{(H - H_{res})\Delta H_{pp}}{\left[(H - H_{res})^2 + \Delta H_{pp}^2\right]^2}, \qquad \textbf{Eq. 4}$$

where $\Delta H_{pp} = \frac{2}{\sqrt{3}\gamma T_2}$ depends on spin-spin relaxation time T_2 and H_{res} is given by equation **Eq. 3**). Through the values of *g* and *A* the resonance field H_{res} (and thus *Y*(*H*) as well) depends on polar angles θ and ϕ that describe the orientation of the spin label with respect to the magnetic field. To simulate EPR spectra one needs to integrate the equation **Eq. 4**), weighted by the spin label orientational distribution ρ(θ,ϕ), over all space.

$$V(H) = \int Y(\theta,\phi) \bullet \rho(\theta,\phi) d\theta d\phi, \qquad \textbf{Eq. 5}$$

To perform the integration knowledge of the spin label orientational distribution is required. In the simplest approach the orientational distribution is considered to be symmetric with respect to the Z-axis, and θ-angle dependence is assumed to be Gaussian

$$\rho(\theta) = \exp\left[-\ln 2 \frac{(\theta - \theta_0)^2}{\Delta\theta^2} \right] \qquad \textbf{Eq. 6}$$

In real systems symmetry requirements assumed in **Eq. 6** are usually not satisfied and more complex distribution functions are needed. A more rigorous approach was developed by Freed and colleagues (20), and it considers an expansion of ρ(θ,ϕ) in a harmonic function series:

$$\rho(\theta,\phi) = \sum_{k,l} C_{kl} D_k^l(\theta,\phi) \qquad \textbf{Eq. 7}$$

Coefficients C_{kl} are optimized during fitting routing and determine the spin label orientation in space. With this approach not only the "traditional" EPR parameters, such as rotational correlation time and order parameter, can be determined but also equilibrium distribution of the spin label orientations, which can be used to elucidate restrictions imposed by protein and eventually to obtain information about protein's conformation. Application of this approach will be discussed in chapter 2.

1.2.4 Dipolar electron-electron resonance (DEER).

Dipolar electron-electron resonance (DEER) is a pulsed EPR technique that detects distance between two spins. It is sensitive in the range 2-6 nm and under certain condition can yield information about distance distribution with ~1Å resolution. If two spins are located in a close proximity, magnetic field of one of them will affect the other. The extent of interaction depends on interspin distance and mutual orientation. In contrast to the continues-wave EPR (CW-EPR) discussed above, in the pulsed EPR electron

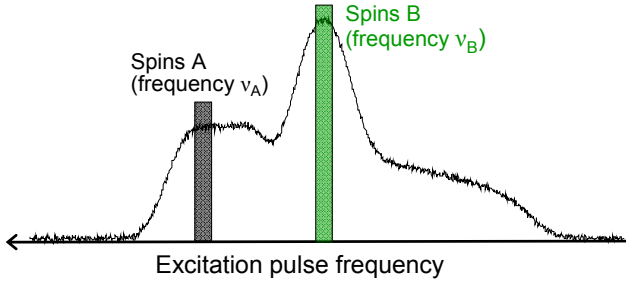

Fig. 12. Typical EPR absorbance spectrum.
Position of the observation pulse (used to excite spins A) and the pump-pulse (used to excite spins B) are indicated with grey and green rectangulars.

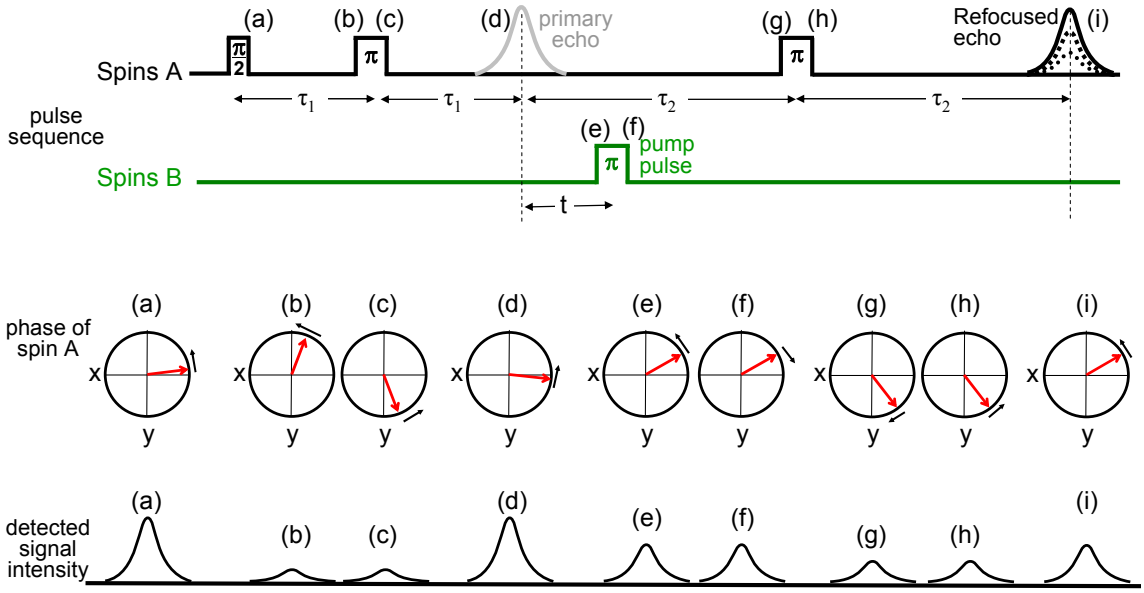

Fig. 13. A 4-pulse DEER experiment.
Top: pulse sequence used to initiate spin transitions. **Middle:** Spin A phase time evolution; black arrows indicate the direction of rotation, and projection of the spin (red arrows) on the X-axis determines the signal intensity. **Bottom:** Intensity of the EPR signal at different time point of the experiment

transitions are stimulated by short electromagnetic pulses and relaxation processes are analyzed to extract information about the system. To understand the idea behind DEER experiment imagine two spins A and B separated by distance *r* and placed into a

magnetic field oriented along the Z-axes. During the experiment spins A are excited at the frequency ν_A with a series of pulses that in the absence of dipolar interactions would form a refocused echo of certain amplitude (**Fig. 13, top**). If during the experiment spins B are independently excited at a frequency ν_B (Fig. 12), then the intensity of spins A refocused echo will be affected. The extent of echo modulation will vary depending on the timing *t* (**Fig. 12**) of the pump-pulse (pulse used to excite the spins B). This dependence can be used to extract the information about the interspin distance.

Conventional 4-pulse DEER sequence is shown on (**Fig. 13**). First, spins A are excited with a $\pi/2$ pulse that tips the spins into an XY plane generating the EPR signal, which is proportional to the projection of the magnetic moment onto the X-axis (**Fig. 13(a)**). Because of inhomogeneities in the local magnetic field spins begin to dephase, decreasing the signal intensity. For example, if the magnetic field generated by spins B result in dephasing with the angular frequency ω_{AB}, the accumulated phase difference after time t' is ($\omega_{AB} \cdot t'$) (**Fig. 13, b**). After the time τ_1 a second, π-pulse, is applied, it flips the spins A around the X-axis (**Fig. 13, c**) and refocuses spins forming the primary echo (**Fig. 13, d**). After the echo is formed, spins A begin to dephase again (**Fig. 13, e**), and another π-pulse (**Fig. 13,g,h**) reverses the process forming the refocused echo (**Fig. 13, i**). Finally, if at the time *t* after formation of the primary echo, a π-pulse at a different (pump) frequency is applied, it inverts the magnetization of the spins B and thus reverse the direction of rotation of the spins A (**Fig. 13, f**), preventing the full coherence recovery At the time of refocused echo formation, coherence will be restored only partially and phase difference will be $2\omega_{AB}(t-\tau)$. Since EPR signal V_{intra} is proportional to the projection of magnetization onto the X-axes, the observed signal will oscillate (depending on delay *t*) proportionally to the $\cos(2\omega_{AB}(t-\tau))$:

$$V_{intra}(t)=V_0 \cos(2\omega_{AB}(t-\tau)), \qquad \textbf{Eq. 8}$$

where V_0 is the echo amplitude and ω_{AB} is the dipolar coupling frequency given by

$$\omega_{AB}(r,\theta) = \frac{\mu_{Bohr}^2 g_A g_B}{\hbar r^3}(3\cos^2\theta - 1), \qquad \textbf{Eq. 9}$$

where r is the distance separating the spins, θ is the angle between the interspin vector and the applied magnetic field, μ_{Bohr} is the Bohr magneton, and g_A, g_B are the electrons g-values.

In most cases distance distribution can be assumed Gaussian (**Eq. 10**) and the sample to be randomly oriented (no preference in θ).

$$\rho(r) = \frac{1}{\sigma\sqrt{2\pi}} \exp\left(-\frac{(r-R)^2}{2\sigma^2}\right),\ \sigma = \frac{FWHM}{2\sqrt{2\ln 2}}, \qquad \textbf{Eq. 10}$$

Integration over r and θ gives the final signal due to the intramolecular interactions:

$$V_{intra}(t, R, \sigma) = \\ = \int_r \int_0^{\pi/2} \frac{1}{\sigma\sqrt{2\pi}} \exp\left(-\frac{(r-R)^2}{2\sigma^2}\right) \cdot \cos\left(\frac{2\mu_{Bohr}^2 g_A g_B}{\hbar r^3}(3\cos^2\theta - 1)(t-\tau)\right) d\theta dr \qquad \textbf{Eq. 11}$$

In addition to the interaction between spins A and B within one molecule or molecular complex, spin echo amplitude is affected by intermolecular interactions. If the concentration of spins in the sample is kept relatively small, then the average distance between spins will be sufficiently large and intermolecular interactions can be considered as DEER background signal that result in exponential decay of the echo intensity **Eq. 12** (21)

$$V_{inter}(t) = \exp\left[\frac{8\pi\mu_{Bohr}^2 g_A g_B}{9\sqrt{3}\hbar} \cdot CF_B |t-\tau|\right], \qquad \textbf{Eq. 12}$$

where C is the concentration of unpaired spins and F_b is the fraction of spins excited by the pump pulse.

Consequently, the experimental DEER signal is composed of two parts, osciallations due to interactions between coupled spins and exponential decay due to intramolecular interactions(21, 22).

$$V(t) = V_{inter}(t) \times V_{intra}(t) \qquad \textbf{Eq. 13}$$

In practice, the background signal does not carry any useful information and needs to be "subtracted" from the experimental data. This can be achieved by recording signal form a singly labeled sample (in such a case there will be no coupled spins) or by subtracting the simulated background during data analysis.

1.2.5 Practical aspects of DEER.

DEER provides a reliable and relatively simple way to measure interprobe distance distributions. One of the key features of this approach is that the width of the distribution can be determined as reliably as the mean interprobe distance. As a result, DEER yields information not only about the average protein structure, but also about its flexibility. Consequently this method can be used to determine dynamic properties of the system or detect order-to-disorder transitions that are known to be crucial for many biomolecules. To the first approximation, frequency of the oscillations (or decay rate) can be considered as a measure of the mean distance and the "quality" (amplitude of oscillations) as a measure of flexibility. High frequency of oscillations (fast decays) correspond to shorter distances and low frequency (slow decays) to the longer distances. Large amplitude of oscillations indicate narrow distribution width (rigid protein structure) and the absence of visible oscillations indicate large width (high degree of flexibility within protein) (**Fig. 14**).

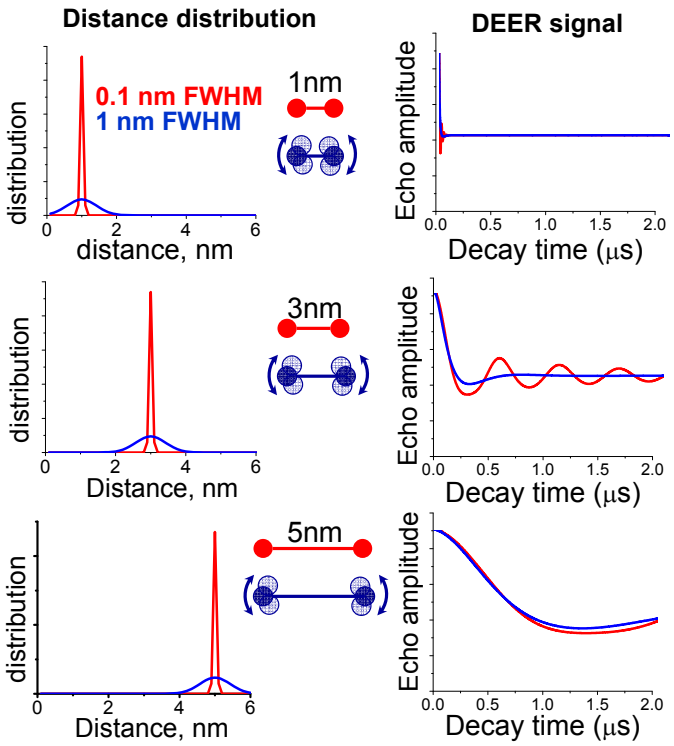

Fig. 14. Distance distributions (left) and corresponding simulated DEER signals (right).
Red - narrow distribution (FWHM=0.1nm), blue – wide distribution (FWHM=1nm). Short interprobe distance results in faster decays (compare top and bottom), and narrow distribution results in better pronounced oscillation (compare red and blue).

In comparison with other spectroscopic techniques (e.g. fluorescence resonance energy transfer, see section 1.3) DEER has several advantages. The smaller size of spin labels, compared to optical probes, ensures minimal structural perturbation of the system. DEER decays have a complex shape with multiple features, which facilitates analysis, resulting in a more reliable data interpretation. Finally, identical probes can be used for both labeling sites, which greatly

simplifies the sample preparation. The major disadvantage of the DEER is the necessity to perform experiments at cryogenic temperatures, typically ~65K. This requirement is due to a dramatic increase of spin-spin relaxation rates at ambient temperatures, which makes formation and detection of the spin echo virtually impossible.

Analysis of DEER decays is performed with one of the developed software packages such as DeerAnalysis (23). DEER signals are simulated (usually assuming multi-Gaussian distance distribution) and fit to the background corrected experimental data.

1.3. Time-resolved fluorescence energy transfer (TR-FRET).

1.3.1. Fluorescence.

Fluorescence is the process of emitting light when a fluorophore goes from an excited state to the ground state. The molecular events occurring during light absorption and emission are typically illustrated with the Jablonski diagrams (**Fig. 15**). If a photon's energy matches the energy gap between the two states of the fluorophore, the photon can be absorbed, and the molecule will go to an excited state. The transition typically happens to a higher vibrational level, but then the molecule rapidly (within 10^{-12}s or less) relaxes to the lowest vibrational level through a non-emitting process, called internal conversion. Return to the ground state also typically occurs to a higher vibrational level and is followed by a rapid relaxation to the equilibrium state. The complex structure of the vibrational levels determines the absorption and emission spectra of the molecule. Due to the internal conversion, part of the electrons energy is dissipated. Consequently, the energy of the absorbed photon is greater than the energy of the emitted photon. As a result, emission spectra are typically shifted to the right (longer wavelength) relative to the excitation spectra (**Fig. 16**). This implies that absorbed light has higher frequency (shorter wavelength) than the emitted light, shifting the spectrum to the right. This phenomenon is known as Stocks shift.

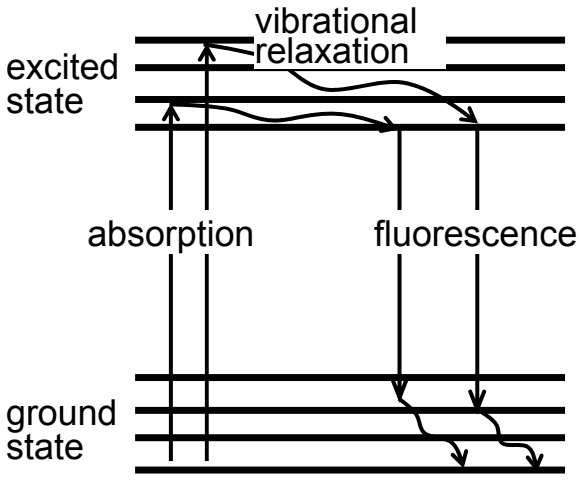

Fig. 15. Jablonski diagram.
Absorption of a photon initiates the transition of a dye to an excited state, from which it then relaxes back to the ground emitting light of a different color (different wavelength). Adapted from (24)

Electron transitions that occur during the fluorescence are transitions "allowed" by the selection rules, consequently corresponding rates of the processes are fast, typically on the order of 10^8s, and the life-time of a typical fluorophore is on the order of $1/10^8$ = 10ns. Fluorophore life-time also depends on solvent and presence of quenchers

that can increase the rate of relaxation. In addition to emitting light (radiative decay) fluorophore can go to the ground state through a so-called non-radiative decay. For instance, energy can be dissipated and converted into heat, or it can transferred to another molecule (of particular interest is the process of fluorescent resonance energy transfer discussed in section 1.3.2). The parameter that describes how much energy is emitted through the radiative processes is known as quantum yield *Q*. It is defined as number of photons emitted over the number of photons absorbed by a molecule: $Q=N_{em}/N_{abs}$. Alternatively, it can be found as $Q=\Gamma/(\Gamma+k_{nr})$, where Γ and k_{nr} are rates of radiative and non-radiative decays respectively. In terms of the life-times, which are inversely proportional to the decay rates ($\tau=1/\Gamma$), quantum yield can be expressed as $Q=\tau/\tau_r$, where τ_r is the radiative life-time (the life time that would exist if no non-radiative processes were present) and τ is the observed life-time. Radiative life-time τ_r is usually assumed to be a property of a fluorophore and independent of local environment, thus quantum yield provides information about other relaxation processes. In biological applications it is preferable to have a "brighter" fluorescent probe as it emits more light and provides higher signal to noise ratio, hence quantum yield is an important parameter, influencing the choice of the dye.

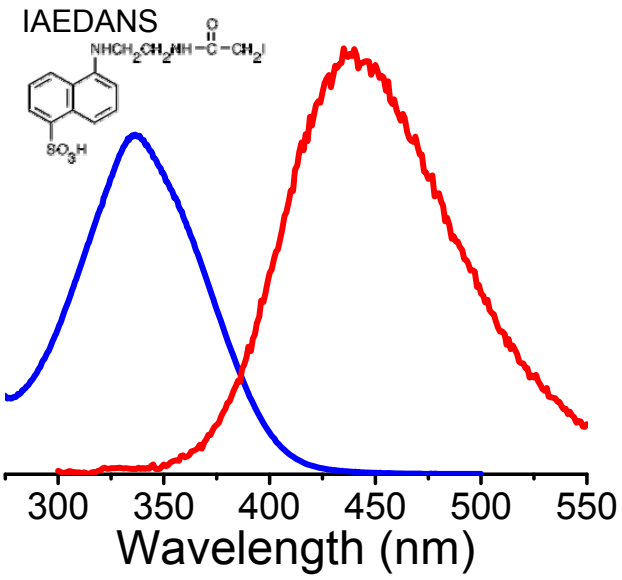

Fig. 16. Absorption (blue) and emission (red) spectra of the fluorescent probe IAEDANS.

1.3.2 TR-FRET

As discussed above, one possible way for a fluorophore to return to the ground state is to transfer the energy to a nearby molecule. Of particular interest is fluorescent resonance energy transfer (FRET), a process of non-radiative energy exchange between a donor molecule in the excited state and an acceptor molecule in the ground state. For FRET to

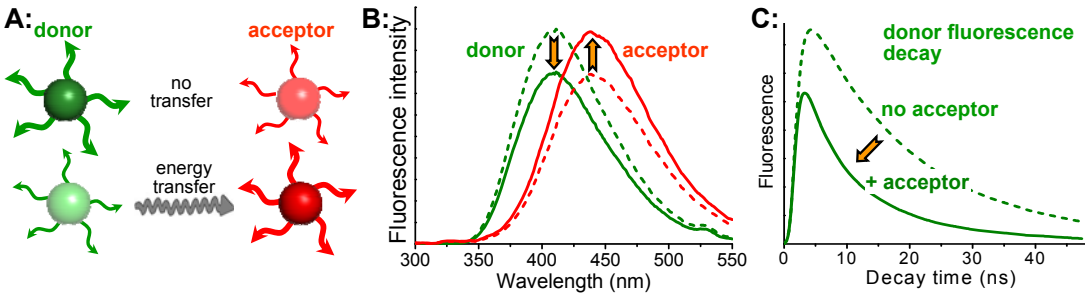

Fig. 17. Fluorescence resonance energy transfer.
(A) schematic representation of FRET effect on the donor and acceptor fluorescence intensity. (B) Changes in the donor and acceptor emission spectra (dashed lines – no FRET, solid lines with FRET). (C) Decrease of the donor fluorescence life-time in the presence of FRET.

occur the emission spectrum of the donor must overlap with the absorption spectrum of the acceptor, and efficiency of the transfer, among other factors, depends on the extent of the overlap. As result of the energy transfer integral intensity of donor's fluorescence decreases, resulting in simultaneous increase of the acceptor's fluorescence (**Fig. 17B**).

The ratio of donor fluorescence in the presence and the absence of the acceptor determines the FRET efficiency **Eq. 14**, which is related to the donor - acceptor distance according to **Eq. 15**.

$$E = 1 - \frac{F_{DA}}{F_D}, \qquad \textbf{Eq. 14}$$

$$E = \frac{R_0}{R_0 + R}, \qquad \textbf{Eq. 15}$$

where F_D and F_{DA} is donor florescence in the absence and presence of an acceptor, R is distance between the donor and the acceptor and R_0 is the Förster distance (defined as distance at which E=0.5).

The disadvantage of this approach is that only averaged information about the system can extracted. For instance if two populations of protein with two interprobe distances are present, only the averaged distance can be obtained from **Eq. 14** and **Eq. 15**. This handicap can be overcome with the time-resolved FRET. Presence of the acceptor not only decreases integral intensity of the donor, but it also decreases its life-time due to addition of an extra non-radiative process (**Fig. 17C**). Ratio of the donor life-times in the presence and absence of the acceptor can be used to calculate the interprobe distance. Fluorescence decay is typically multi-exponential and in the absence of the acceptor, donor decay can be described with (**Eq. 16**)

$$F_D(t) = \sum_{i=1}^{n} A_i \exp\left(-\frac{t}{\tau_{Di}}\right), \qquad \textbf{Eq. 16}$$

where τ_{Di} is an i^{th} component of the donor life-time.

In the presence of an acceptor an additional relaxation channel is created and life-time of the donor decreases. In this case donor fluorescence is given by the **Eq. 17**

$$F_{DA}(t,R) = \sum_{i=1}^{n} A_i \exp\left(-\frac{t}{\tau_{Di}} - \frac{t}{\tau_{Di}}\left(\frac{R_{0i}}{R}\right)^6\right), \qquad \textbf{Eq. 17}$$

where the second term describes the rate of the energy transfer **Eq. 18**

$$k(r) = \frac{1}{\tau_{Di}}\left(\frac{R_{0i}}{R}\right)^6, \qquad \textbf{Eq. 18}$$

where τ_{Di} is the life-time of the donor in the absence of the acceptor, R is the donor-acceptor distance, and R_{0i} is the Förster distance, given by **Eq. 19**

$$R_{0i} = 9786[J(\lambda)\kappa^2\eta^{-4}Q_{Di}]^{1/6}, \qquad \textbf{Eq. 19}$$

where $\kappa^2 = 2/3$ is the labels orientation factor, $\eta = 1.4$ is the index of refraction of the medium, Q_{Di} is the donor quantum yield given by $Q_{Di} = \langle Q_D\rangle * \tau_{Di}/\langle\tau\rangle$, where $\langle\tau\rangle = (1/n)\sum_{i=1}^{n} A_i\tau_{Di}$. $J(\lambda)$ is the spectral overlap integral between normalized donor emission spectrum $F_D(\lambda)$ and the acceptor absorption spectrum $\varepsilon_A(\lambda)$ (24).

To reflect protein flexibility distance distribution $\rho(r)$ is often used instead of a single discrete distance R. For a Gaussian distribution (**Eq. 10**) Eq. 17 transforms into

$$F_{DA}(t,R,FWHM) = \int_{-\infty}^{+\infty} \rho(r) \cdot \sum_{i=1}^{n} A_i \exp\left(-\frac{t}{\tau_{Di}} - \frac{t}{\tau_{Di}}\left(\frac{R_{0i}}{r}\right)^6\right) dr, \qquad \textbf{Eq. 20}$$

Eq. 20 can be used to simulate FRET signal for any R (mean interprobe distance) and FWHM (full width of the distribution at half maximum) and fit the experimental signal.

1.3.3 Practical aspects of TR-FRET

TR-FRET is another spectroscopic technique that yields information about the probe-to-probe distance distribution. Analogously to DEER, TR-FRET can resolve multiple populations and is sensitive to both mean distance and width of the distribution. Depending on the choice of the donor-acceptor dye pair, distances in the 2nm-10nm range can be reliably determined. For the optimum sensitivity the measured distance should be between $0.68R_0$ and $1.44R_0$, which corresponds to the 0.1-0.9 FRET efficiency (**Fig. 18**). If the distance is too short or too long, TR-FRET resolution capabilities will be reduced (**Fig. 19**)

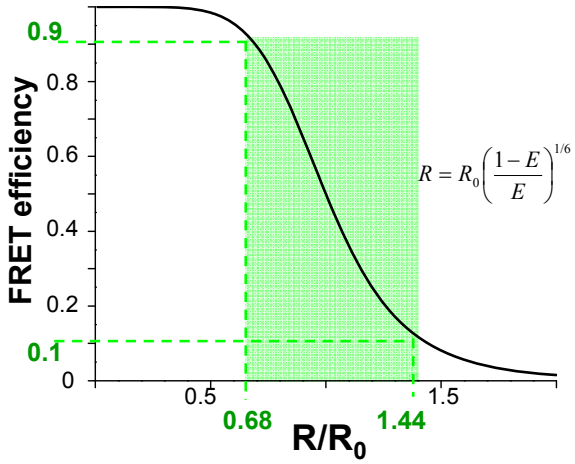

Fig. 18. Dependence of the energy transfer efficiency on the R/R_0 ratio (average distance over the Förster distance).
Optimal sensitivity is achieved in the 0.1-0.9 efficiency range, which corresponds to distances between $0.68R_0$ and $1.44R_0$.

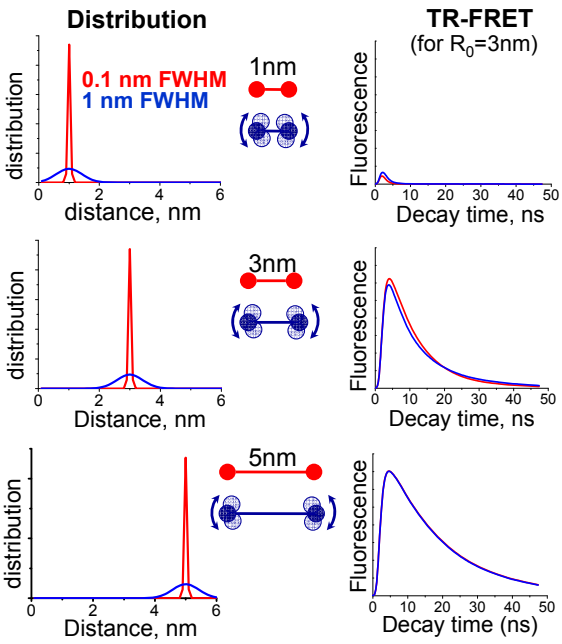

Fig. 19. Distance distributions (left) and corresponding simulated FRET signals (right).
Red - narrow distribution (FWHM=0.1nm), blue – wide distribution (FWHM=1nm). Optimum sensitivity (middle decays) is achieved only with a dye pair that has an appropriate Förster distance R_0.

TR-FRET is several orders of magnitude more sensitive than EPR, virtually noiseless fluorescence decays can be obtained in less than 1 second, and decays with sufficiently high signal-to-noise ratio can be obtained in 0.1ms. Such high sensitivity makes TR-FRET an ideal tool for kinetic experiments, where protein structure needs to be determined during the course of biochemical reaction with millisecond or even submillisecond resolution. An additional advantage of TR-FRET is the possibility to perform experiments at physiological temperatures.

Chapter 2. Muscle and nonmuscle myosins probed by a spin label at equivalent sites in the force-generating domain

Roman V. Agafonov[1†], Yuri E. Nesmelov[1†], Margaret A. Titus[2], David D. Thomas[1,*]

[1]Department of Biochemistry, Molecular Biology and Biophysics, [2]Department of Genetics, Cell Biology and Development, University of Minnesota Medical School, Minneapolis, MN55455

[†]R.V.A. and Y.E.N. contributed equally to this work

Published in *Proc Natl Acad Sci USA 1*05(36):13397-402. PMID:18765799

http://www.pnas.org/content/105/36/13397.full?sid=8513b649-e3dd-4e35-abab-4ad60b07cdd8

*To whom correspondence should be addressed

Abbreviations: EPR (electron paramagnetic resonance), SDSL (site-directed spin labeling), S1 (subfragment 1 of myosin heavy chain), IASL (iodoacetamideTEMPO spin label).

2.1 Overview

We have engineered a mutant of *Dictyostelium discoideum* (*Dicty*) myosin II that contains the same fast-reacting "SH1" thiol as in muscle myosin, spin-labeled it, and performed electron paramagnetic resonance (EPR) to compare the structure of the force-generating region of the two myosins. *Dicty* myosin serves as a model system for muscle myosin, due to greater ease of mutagenesis, expression, and crystallization. The catalytic domains of these myosins have nearly identical crystal structures in the apo state, but there are significant differences in ATPase kinetics, and there are no crystal structures of skeletal muscle myosin with bound nucleotides, so another structural technique is needed. Previous EPR studies, with a spin label attached to SH1 in muscle myosin, have resolved the key structural states of this region. Therefore, we have performed identical experiments on both myosins spin-labeled at equivalent sites. Spectra were identical for the two myosins in the apo and ADP-bound states. With bound ADP and phosphate analogs, (a) both proteins exhibit two resolved structural states (pre-powerstroke, post-powerstroke) in a single biochemical state (defined by the bound nucleotide), and (b) these structural states are essentially identical in the two myosins but (c) are occupied to different extents as a function of the biochemical state. We conclude that (i) myosin structural and biochemical states do not have a one-to-one correspondence, and (ii) *Dicty* myosin can serve as a good analog for structural studies of muscle myosin only if differences in the coupling between biochemical and structural states are taken into account.

2.2 Introduction

Myosin II is a motor enzyme involved in muscle contraction and cell motility through a cycle of actin-activated ATP hydrolysis. The coupling of ATP hydrolysis and force generation is determined by myosin's head domain, subfragment 1 (S1). The myosin ATPase cycle can be described to a first approximation by the following scheme:

$$M \xleftrightarrow{K_1} M*ATP \xleftrightarrow{K_2} M**ADP.P \xleftrightarrow{K_3} M*ADP \xleftrightarrow{K_4} M, \qquad \textbf{Scheme I}$$

where M, M*, and M** are myosin structural states, originally identified by intrinsic fluorescence (15). In this scheme, these structural states are assumed to be tightly coupled to biochemical states, which are defined by the nucleotide bound to the active site. Structural changes of muscle myosin have also been detected by electron paramagnetic resonance (EPR) of a nitroxide spin label (IASL) at SH1 (C707) (25-28), fluorescence of dyes attached to SH1 (29, 30), and fluorescence resonance energy transfer (FRET) between probes at SH1 and other sites (31, 32) or W510 (33). All these studies reflect structural changes of the force-generating region of myosin, which includes the converter domain, N-terminal domain, and the relay and SH1 helices. However, only EPR can resolve and quantify the distinct structural states depicted in **Scheme I** in solution (28).

The only crystal structure of myosin II from skeletal muscle was determined in the apo state (Rayment, et al., 1993). Other crystal structures of myosin II, from *Dictyostelium discoideum* [*Dicty*], scallop and smooth muscle, have been obtained from myosin trapped in different states with nonhydrolyzable nucleotide analogs. Although there is considerable variation among these structures in the force-generating region, they appear to be divided into two classes, often denoted as post-powerstroke and pre-powerstroke, which have been assigned to the M* and M** states. Thus in **Scheme I**, step 3 is the powerstroke (M** to M*) and step 2 is the recovery (repriming) stroke (M* to M**)(8). Crystal structures suggest that in the M*-to-M** transition, a kink is formed in the relay helix, and the converter domain, controlled by the relay helix, dramatically changes its orientation (7, 34, 35). These changes in the force-generating region are governed by ATP binding and hydrolysis, and it is accepted that they reflect allosteric effects from the nucleotide binding site.

However, the correlation between bound nucleotide (biochemical state) and structural state is not entirely consistent. *Dicty* and smooth muscle myosin complexed with the ADP.BeF_x nucleotide analog (34, 36) show a dramatic difference in crystal structure (M** in Dicty, M* in smooth); moreover, the same myosin isoform (*Dicty*), complexed with the same nucleotide analog (ADP.BeF_x), has been observed in both structural states in crystals (34, 37). It is not clear whether these differences reflect intrinsic properties of different myosins or they arise from different experimental conditions employed during protein preparation and crystal growth. These discrepancies must be resolved using structural methods that do not require crystallization. This is particularly important due to the frequent usage of *Dicty* myosin as a model system to study the mechanism of muscle contraction. Compared with muscle myosin, it is easy to express *Dicty* myosin in large quantities, create truncated versions of the protein to facilitate crystallization, and to mutate the protein for structure-function analysis and for site-directed labeling (34, 38-40). Nevertheless, the application of any model system requires validation. The high degree of homology between muscle and *Dicty* myosin II suggests that the two proteins have similar structures in solution; but direct experimental evidence is needed to test this assumption. The only crystal structure available for skeletal muscle myosin is the apo form (no nucleotide), which is nearly identical to the *Dicty* structure obtained under similar conditions (2, 35). However, some kinetic properties of *Dicty* and muscle myosin (based on intrinsic fluorescence, interaction with pyrene-labeled actin and MANT nucleotide) are different: *Dicty* myosin exhibits slower ATP hydrolysis (41), faster ADP release (41) and faster dissociation of phosphate analogs (42). It is not clear whether the observed differences are due to different kinetic constants or to different structural states in the two proteins. Unfortunately, most studies comparing *Dicty* and muscle myosins in solution are focused on kinetic aspects, rather than structural. Our study provides the missing information, providing high-resolution spectroscopic data in solution that clarifies greatly the extent to which *Dicty* is (and is not) a valid muscle myosin analog.

The goal of the present study is to determine to what extent the structural dynamics of the force-generating region of *Dicty* myosin resembles that of muscle myosin in solution, and thus to assess the validity of extending structural information available for *Dicty* onto

muscle myosin. *Dicty* myosin contains a Thr residue at position 688, which has been shown to be biochemically equivalent to the SH1 site (Cys 707) in skeletal myosin, since the mutation T688C permits Dicty myosin to undergo a similar nucleotide-dependent crosslinking reaction as observed for skeletal myosin (43). Therefore, starting from a *Dicty* construct lacking reactive Cys (40), we created a T688C mutant, attached a spin label (iodoacetamido-TEMPO, designated IASL) to both myosins, acquired EPR spectra in different biochemical states, and analyzed EPR spectra to determine the restriction of spin label rotational motion. The resolved EPR spectral components were assigned to structural (conformational) states, allowing us to compare the two myosins directly with respect to the structural states of the force-generating region and the coupling of these structural states to biochemical states. The results not only answer important questions about the similarities and differences of the two myosins, but also provide fundamental insights into the structural dynamics of force generation in myosin.

2.3 Results

Labeling Efficiency. The extent of protein modification by the spin label was determined by mass spectrometry (**Fig. 20**). The two peaks of skeletal myosin and the single peak of *Dicty* myosin were each shifted by 213 Da, the mass of the attached spin label. Negligible peak intensity was observed at positions corresponding to unlabeled S1. Control experiments with mixtures showed that unlabeled and labeled proteins (both muscle and *Dicty*) were detected with similar sensitivity by MS. These results confirm complete labeling of myosin with only one label reacting per protein molecule.

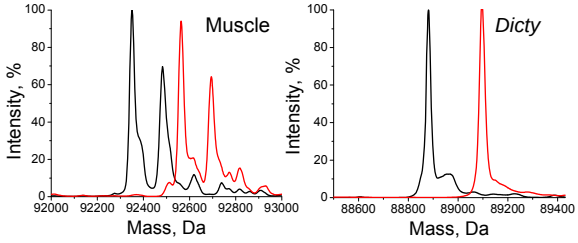

Fig. 20: MS spectra of unlabeled (black) and IASL labeled (red) S1.

Functional Properties of IASL-S1. High-salt (**Table 1**) and actin-activated (Table **2**) ATPase activities were measured to evaluate the effect of labeling on functional properties of myosin. The effects of labeling on high-salt ATPase activities are much less dramatic for *Dicty* than for muscle myosin – the decrease in the K/EDTA activity is less pronounced in *Dicty*, and the large increase of Ca activity is absent (**Table 1**).

Table 1. High-salt ATPase activity

Myosin	K/EDTA, s^{-1}		Ca, s^{-1}	
	Unlabeled	Labeled	Unlabeled	Labeled
Muscle	8.5 ± 0.5	1.4 ± 0.3	1.0 ± 0.1	11.2 ± 1.3
Dicty	0.32 ± 0.12	0.11 ± 0.09	4.2 ± 0.9	4.7 ± 2.1

Table 2. Actin-activated ATPase activity

Myosin	[a]V_{basal}, s^{-1}		[b]V_{max}, s^{-1}		[c]K_m, μM	
	Unlabeled	Labeled	Unlabeled	Labeled	Unlabeled	Labeled
Muscle	0.10±0.02	0.32±0.13	13.5 ± 0.5	2.4±0.2	13.8 ± 2.3	7.2 ± 0.3
Dicty	0.15±0.03	0.42±0.05	4.9 ± 0.8	1.9 ± 0.4	12.8 ± 1.8	8.8 ± 1.8

[a] In the absence of actin, [b]at saturating actin, [c]actin concentration at which V = 0.5V_{max}

Under physiological buffer conditions, the ATPase activities of the two myosins are quite similar, especially after spin labeling, which removes all significant differences between the two (**Table 2**). We confirm previous observations (27, 44) that modification of muscle myosin at the SH1 site alters its ATPase kinetics, and show that qualitatively similar effects take place for *Dicty* myosin, including a substantial decrease in V_{max}, the activity at saturating actin (**Table 2**). At the same time, these results demonstrate unambiguously that the completely labeled proteins (as shown by MS data in **Fig. 20**) are active and are activated by actin.

Binding of Nucleotide Analogs to IASL-S1. To ensure that the concentrations of nucleotide analogs (ADP plus phosphate analog, Table) used in our experiments were saturating and the myosin population was biochemically homogeneous, EPR spectra were recorded at different ligand concentrations. Increasing the concentration above 5 mM did not change EPR spectra, indicating that 5mM is indeed a saturating concentration in all cases. The rate of ATP hydrolysis was measured for these same samples under EPR conditions. Binding of nucleotide analogs abolishes myosin ATPase activity (45). We found that incubation of myosin with 5 mM nucleotide analog decreased the ATPase rate to less than 5% of the control value (Table S1 in Supporting Information, SI), confirming that essentially every myosin formed a complex with nucleotide analog.

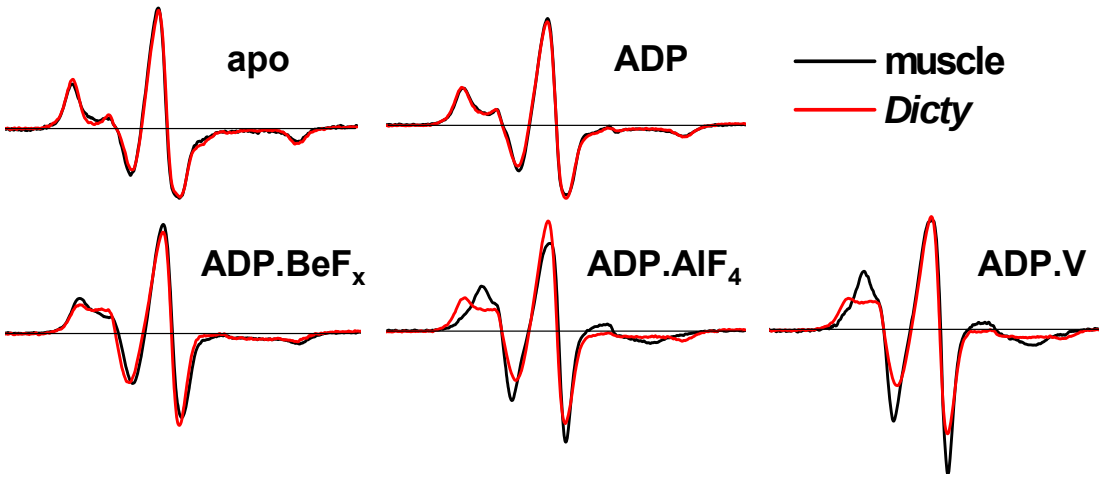

Fig. 21: EPR spectra of muscle and *Dicty* S1 in different biochemical states.

EPR of IASL-S1 Complexed with Nucleotide Analogs. EPR spectra were recorded under conditions (defined above) intended to trap intermediate biochemical states in the ATPase cycle. In the absence of nucleotide (apo state), muscle and *Dicty* myosin have virtually identical EPR spectra **Fig. 21** (M), indicating no difference in spin label dynamics and suggesting structural similarity of the force-generating regions. This agrees with crystallographic studies showing similar atomic structures for these proteins in the apo state (2, 35). The apo spectra are characteristic of strongly immobilized spin labels, having little or no ns mobility relative to the protein, as shown previously for muscle myosin (26). The binding of ADP causes a slight but significant narrowing of the spectrum (**Fig. 26**), as shown previously for muscle myosin (26), indicating slight mobilization of the label, but there is still no significant difference between muscle and *Dicty (***Fig. 21**, M.ADP). In contrast, there are clear differences between the two myosins in the presence of ADP and phosphate analogs (**Fig. 21**, bottom row). These differences are especially pronounced in the low-field portion of the spectrum. All of these spectra are significantly narrower than in the presence of ADP, indicating further mobilization of the spin label. The post-hydrolysis analogs (ADP.AlF_4 and ADP.V) induce greater probe mobility and show a larger difference between Dicty and muscle, compared with the prehydrolysis analog (ADP.BeF_x).

Quantitative Analysis of EPR Spectra: Resolved Structural States and their Mole Fractions. IASL-labeled muscle S1 exhibits single-component X-band EPR spectra in

apo and ADP-bound states, and two-component spectra in the nucleotide analog bound states (26-28). These spectra clearly resolve three structural states, presumably the same states detected by intrinsic fluorescence: M, M*, and M**. These three structural states have been resolved and characterized in terms of spin label rotational dynamics, based on EPR spectra obtained at both X (9.4 GHz) and W (94 GHz) band (Table 4 in (28)), reflecting the structure of the force-generating domain of muscle myosin. In the present study, experimental X-band EPR spectra, $V_{exp}(H)$ of muscle and *Dicty* myosins were fitted as a linear combination of previously determined spectral components V, V*, and V**, corresponding to structural states M, M*, and M**(28):

$$V_{exp}(H) = xV(H) + x^*V^*(H) + x^{**}V^{**}(H). \qquad \textbf{Eq. 21}$$

The only variable parameters in the fit were mole fractions (x, x*, and x**), and the quality of the fit was quantified with Pearson's χ^2 test. Variation of parameters related to spin label dynamics (rotational correlation times and order parameters) did not improve the fit. These fits confirmed that muscle and *Dicty* myosins have (a) a single structural state M (x = 1) in the apo biochemical state and (b) a single structural state M* (x* = 1) in the ADP-bound biochemical state. In biochemical states containing bound ADP and phosphate analogs, spectra all exhibit two components, a combination of M* and M** structural states, with different mole fractions (x* and x**) for muscle and *Dicty* myosins (**Table 3**). Experimental spectra and fits are shown on **Fig. 22**, and the mole fractions obtained from these fits are given in **Table 3**.

Table 3 Mole fractions of structural states derived from EPR spectra (Fig. 22)

myosin	apo	ADP	ADP.BeF_x	ADP.AlF_4	ADP.V
muscle	1, 0, 0	0, 1, 0	0, 0.84, 0.16	0, 0.15, 0.85	0, 0.15, 0.85
Dicty	1, 0, 0	0, 1, 0	0, 0.66, 0.34	0, 0.72, 0.28	0, 0.63, 0.37

Values are mole fractions (*x, x*, x***) of structural states (*M, M*, M***). Uncertainties are 0.02 to 0.04.

These results indicate that when myosin is trapped by ADP and a phosphate analog in a single biochemical state, there remain significant populations of both M* and M** structural states in equilibrium. Thus there is clearly not a one-to-one correspondence between myosin's biochemical and structural states. This is much more clear for *Dicty*, in which the minor component makes up about 1/3 of the population in these states, than for muscle, in which the minor component is about 1/6 (*Table 3*). We conclude that the coupling between biochemical and structural states (as revealed by the coupling between the nucleotide binding site and the force-generating region) is different for the two myosins. This difference in coupling is presumably related to the observed differences in ATPase kinetics between muscle and nonmuscle myosins (41, 46-48).

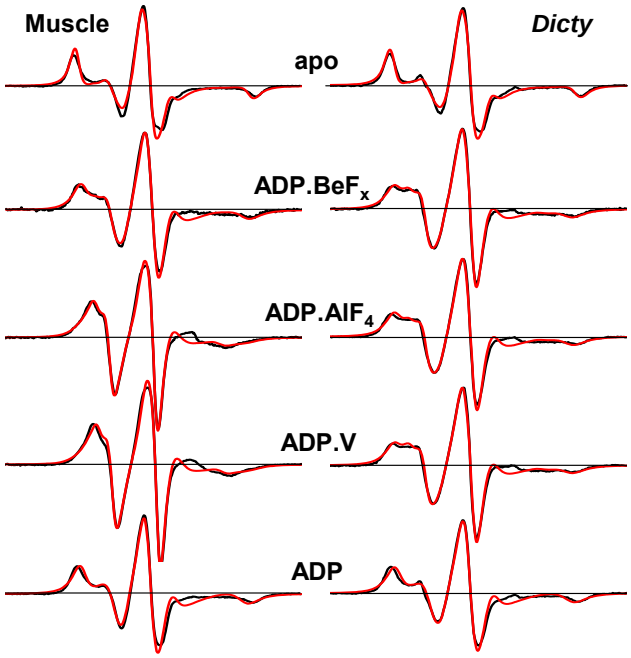

Fig. 22: Computational simulations of EPR spectra. Assuming a linear combination of spectra (Eq. 1), corresponding to M, M* and M** states of myosin. Mole fractions are given in *Table 3* Black – experiment, red – best-fit simulation.

Temperature Dependence and Thermodynamic Analysis. To test the hypothesis that the resolved spectral components observed in EPR experiments represent an equilibrium between structural states, we studied the effect of temperature on the distribution between the states (**Fig. 23**). It was previously demonstrated for muscle myosin (44) that an increase in temperature shifts the equilibrium from the pre-hydrolysis to the post-hydrolysis biochemical state. Our EPR experiments revealed a similar temperature dependence on the

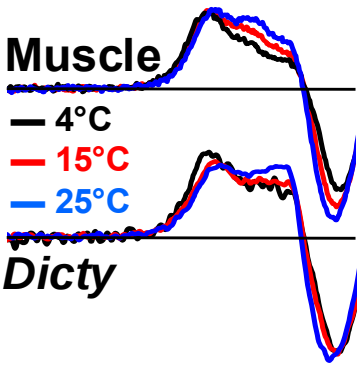

Fig. 23. Temperature dependence of EPR spectra (low-field region) of myosin with ADP.BeF$_x$ bound.

distribution between structural states, without a change in the biochemical state – the mole fraction x** of the M** population increased with temperature at the expense of the M* population. **Fig. 23** demonstrates this effect for S1ADP.BeF_x; the effect was similar for S1.ADP.AlF_4 (**Fig. 27**). Thus there is a temperature-dependent equilibrium between the M* and M** structural states within a single biochemical state.

By deconvoluting EPR spectra (Eq. 1), we determined the mole fractions x* and x** of M* and M** states as a function of temperature, and calculated the enthalpy and entropy of the M*-to-M** transition from the van't Hoff equation for both myosins (**Fig. 27** and **Fig. 28**). **Fig. 24** shows the changes in G, H, and S that occur at 20°C. Although the equilibrium between M* and M** is fairly well balanced (small ΔG in all cases), the values of ΔH and TΔS are large. This suggests that substantial structural changes occur in this transition, but in each case the unfavorable enthalpy change is balanced almost precisely by a favorable entropy change. Also, while the |ΔG| values are smaller for Dicty (more balanced equilibrium than in muscle), the |ΔH| and |TΔS| values are large for both myosins. I.e., even though the two biochemical states are more similar in Dicty than in muscle, the M*-to-M**structural transition is enthalpically and entropically large in both myosins.

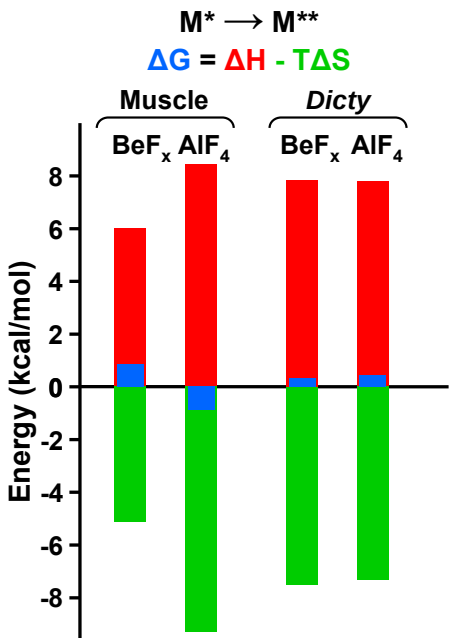

Fig. 24: Thermodynamics of the M*-to-M** transition at 20°C.
(based on van't Hoff plots (**Fig. 28**, Table 5).

Myosin Conformation During Steady-State ATP Hydrolysis. To confirm that the structural states M* and M**, trapped by phosphate analogs, also exist during the ATPase cycle, as suggested by **Scheme I**, we recorded EPR spectra in the presence of ATP (with addition of 40 mM creatine phosphate and 1mg/ml of creatine phosphokinase). The resulting spectrum for muscle myosin (**Fig. 25**, black) clearly shows the presence of two structural states M* and M** (69% and 31% respectively), in good agreement with previously published results (26). In the case of *Dicty* myosin, the EPR spectrum (**Fig. 25**, red) was remarkably similar to the one obtained for the ADP complex, showing (within experimental error, ± 6%) only the M* component. This result is not entirely surprising, since EPR of .the ADP.AlF_4 and ADP.V complexes (which predominantly generate the M** state in muscle myosin) showed a much larger fraction in the M* state for *Dicty*. It has been previously shown that the apparent forward rate constant of ATP hydrolysis (the step k_2 that populates the M** state in **Scheme I**), is significantly slower in *Dicty* S1 compared to muscle S1 (41, 46, 49). In addition, the steady-state rate of ATP hydrolysis (k_3 in **Scheme I**, since P_i release is rate-limiting) is greater for *Dicty* myosin (**Table 2**), again suggesting depopulation of M**, and modification of the SH1 site of muscle myosin shifts the equilibrium toward the M* state (27, 44). It appears that the combination of these factors leads to the domination of the M* conformation during steady-state ATP hydrolysis in *Dicty* S1.

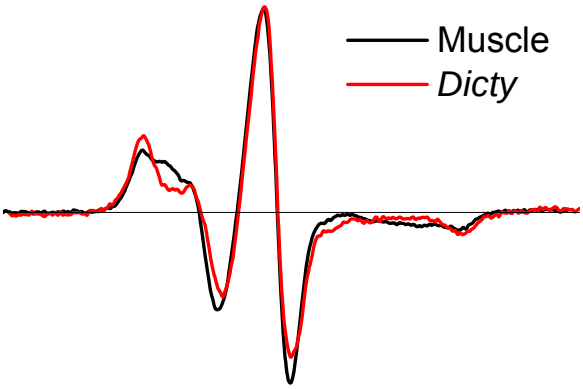

Fig. 25: EPR spectra during steady-state ATP hydrolysis.

2.4 Discussion

EPR Resolves Structural States. We have used site-directed spin labeling and EPR to compare the structure of the force-generating region of *Dicty* and muscle myosins in different states of the ATPase cycle under physiological conditions. Compared with other structural techniques, EPR offers the resolution to distinguish several populations with different structures. This structural resolution has allowed us to determine that myosin can adopt two different conformations (structural states) in the presence of one nucleotide analog (biochemical state). Although this effect is present in both isoforms, it is particularly clear for ***Dicty*** myosin (*Table 3*). Unfortunately, other structural techniques (e.g., crystallography, electron microscopy) tend to trap a single structural state of a protein, or they are not capable of resolving distinct structural populations and report only average properties (e.g., steady-state fluorescence). Time-resolved fluorescence previously resolved three conformations of the lever arm in Dicty myosin (40); the present study resolves three conformations of the force-generating region.

The Force-Generating Region of Muscle and Non-Muscle Myosin: Similar Structures, Different Kinetic Coupling. Quantitative analysis of EPR spectra reveals one structural state of the force-generating region in apo and ADP-bound biochemical states, and two structural states in the nucleotide analog-bound biochemical states of both muscle and *Dicty* myosin (Table 3). As in previous fluorescence and EPR studies (15, 26, 30), we assigned the structural state in apo S1 as M, in S1.ADP as M*, and two structural states with ADP and phosphate analog bound as M* and M**. As detected by the probe at SH1, the states M, M*, and M** are essentially identical in muscle and *Dicty* myosins, indicating that the structural states of the force-generating region of muscle and *Dicty* myosins are quite similar. The two myosins differ significantly in the populations of structural states in identical biochemical states (***Table 3***), demonstrating differences in kinetic coupling between biochemical and structural states in these myosins.

Thermodynamics of the Power Stroke: Disorder-to-Order Transition. Thermodynamic analysis shows that the M* to M** transition in the two myosins is remarkably similar: large unfavorable enthalpy and favorable entropy changes balance to

produce a small ΔG, and thus a poised equilibrium that significantly populates both states (**Fig. 24**). Since the reverse of this transition (M** to M*) probably represents the power stroke, **Fig. 24** is the most direct demonstration to date that the structural change occurring in the power stroke involves a small free energy change, driven by a large negative ΔH but balanced by a large negative ΔS. I.e., the disorder-to-order transition that occurs in the power stroke (50) plays an important thermodynamic role.

Myosin's Biochemical States are Distinct from Structural States. Our EPR results show that there is not a one-to-one correspondence between myosin's structural and biochemical states (*Table 3*), indicating that **Scheme I** requires more complexity, as previously suggested from kinetic studies. It has been proposed that myosin isomerization can precede the hydrolysis step, producing both M* and M** structural states with bound ATP (16, 51). Similarly, it has been suggested that M* and M** coexist in the post-hydrolysis state (with ADP.P as a ligand) (15, 44):

$$M \leftrightarrow M^{*}ATP \leftrightarrow M^{**}ATP \leftrightarrow M^{**}ADP.P \leftrightarrow M^{*}ADP.P \leftrightarrow M^{*}ADP \leftrightarrow M \quad \textbf{Scheme II}$$

In this scheme, M* corresponds to the post-power stroke (sometimes also designated "near-rigor") state of myosin, and M** corresponds to the pre-power stroke state detected in crystallography (7, 16, 34). It is widely accepted that the binding of ADP and BeF_x traps myosin in the M.ATP biochemical state. According to crystal structures, M.ADP.BeF_x can be in either M* or M** structural states (pdb: 1br4, kk8, 1mmd), suggesting the possibility of the M**.ATP structural state. This hypothesis is supported by the present study, in which EPR shows clearly that both M* and M** states coexist in the M.ADP.BeF_x biochemical state *in solution* (*Table 3*). This suggests that ATP binding is sufficient to switch myosin conformation; hydrolysis is not required to energize myosin, but is needed to continue the cycle. Similarly, our data demonstrate that both M* and M** structural states coexist in the M.ADP.V and M.ADP.AlF_4 biochemical states, supporting the hypothesis that both structural states M* and M** are populated in myosin's post-hydrolysis state (M.ADP.P) as well (15, 44), and P remains in the nucleotide binding pocket during at least part of the powerstroke.

The present study resolves ambiguities raised previously by crystallographic (34, 36, 52) and fluorescence experiments (13), which suggested the absence of a direct correlation between biochemical and structural states of myosin. The presence of a certain ligand at the active site does not necessarily imply a specific protein structure. This principle was previously demonstrated most clearly in muscle fibers, where mechanical strain produced direct evidence for kinetically inequivalent states having the same biochemical ligands (53). The present study shows this to be the case in solution, especially in *Dicty* myosin. This result emphasizes that caution should be exercised in assigning existing crystal structures to myosin conformations at certain steps of the ATPase cycle, and suggests that many of the structural differences observed for different isoforms are likely to be due to different experimental conditions, or to differences in kinetic coupling of structural states, rather than due to intrinsic differences in structural states.

2.5 Conclusions

Through protein engineering and the high resolution of EPR spectroscopy, we compared directly the structures of muscle and nonmuscle myosins in the force-generating region. We found that these myosins share the same three structural states during the ATPase cycle. However, the structural states are populated differently in the two myosins, suggesting differences in the kinetic coupling of biochemical and structural states. We observed two-component EPR spectra, showing that the biochemical state, defined by the bound nucleotide, does not correspond to a single structural state, and reflects rather a balanced equilibrium between structural states. We conclude that *Dicty* myosin can be considered as structurally similar to muscle myosin, when differences in the coupling between biochemical and structural states are taken into account. In both myosins, thermodynamic analysis reveals that the power stroke involves a large favorable enthalpy change that is balanced by a large entropy decrease, supporting the hypothesis that a disorder-to-order transition plays an important role in force generation.

2.6 Materials and Methods

Protein Preparation and Labeling. Actin and myosin were prepared from rabbit skeletal muscle(54), and myosin S1 was prepared and selectively labeled at SH1 (Cys 707) with IASL (28). The T688C mutant of Dictyostelium S1 was constructed and purified as described in (54), except that mutation was introduced at the T688 residue. The base construct for our studies was a Cys-lite S1 mutant that contains no reactive Cys residues (gift from James Spudich). Protein concentrations were determined spectrophotometrically assuming the following extinction coefficients A280nm=0.74 $(mg/ml)^{-1}cm^{-1}$ for skeletal S1, A280nm = 0.69 $(mg/ml)^{-1}cm^{-1}$ for Dicty S1 and A290nm = 0.63 $(mg/ml)^{-1}cm^{-1}$ for actin. Muscle S1 was (55). *Dicty* S1 was labeled at Cys688 with IASL by incubating 100μM S1 with 4-fold excess of IASL for 12 hours on ice. Labeling buffer contained 20mM EPPS (pH 8.0), 50mM KCl, 5mM MgCl2, 1mM EDTA.

Formation of Stable S1.ADP, S1.ADP.V, S1.ADP.AlF_4 and S1.ADP.BeF_x Complexes. Complexes of S1 with nucleotide analogs were obtained by incubation of S1 with 5 mM MgADP (or 5mM MgADP + 20 mM NaF in case of MgADP.AlF_4, and MgADP.BeF_x) for 5 min at 25°C. After that 5 mM $NaVO_4$ (or 5 mM $AlCl_3$, or 5mM $BeCl_2$) were added, and the incubation was continued at 25°C for additional 20 min.

EPR Spectroscopy. X-band EPR spectra were acquired with an E-500 spectrometer (Bruker Instruments, Billerica, MA) using a SHQ EPR cavity (ER4122 ST). Instrument settings were as follows: incident power 2mW, modulation amplitude 1G, modulation frequency 100kHz, scan width 120G, time constant 20.5ms, temperature 20°C. Buffer contained 20 mM EPPS (pH 8.0), 6 mM $MgCl_2$, 1mM EGTA; during steady-state ATP hydrolysis, 40 mM creatine phosphate and 1mg/ml (≥150 units/mg) creatine phosphokinase were also present. Before plotting, each spectrum was normalized by dividing by its double integral, and are all displayed at the same aspect ratio (vertical scale relative to horizontal scale).

Mass Spectrometry. Mass spectrometry employed a QSTAR quadrupole-TOF mass spectrometer with an electrospray ionization source. The protein sample (2mg/ml S1 in 10

mM NH_4HCO_3 buffer at pH 7.9) was injected into the solvent stream using a 10 µL injection loop installed in the integrated loop injector. 3 to 5 injections were performed for every sample with 2 min intervals between them. Data were acquired continuously during load buffer infusion and protein infusions over the range 500 – 2000 m/z. Spectra were analyzed with AnalystQS (Applied Biosystems) software.

Acknowledgements.

This work was supported by NIH grants AR32961 (DDT) and AR53562 (YEN), a grant from the Minnesota Medical Foundation (YEN), and the University of Minnesota Supercomputing Institute. We appreciate excellent technical assistance from Sarah Blakely, Erin M. Hoffman, Eunice Song, Igor V. Negrashov, and Octavian Cornea. Software was kindly provided by Dr. Z. Liang (Cornell University).

2.7 Supporting information

Results

Binding of Nucleotide Analogs to IASL-S1. Addition of 5 mM nucleotide analog to IASL-S1 under EPR conditions (as in **Table 2**) abolished virtually all myosin ATPase activity (**Table 4**), showing that IASL-S1 is saturated with these nucleotide analogs. This justifies our treating these complexes as distinct and homogeneous biochemical states.

Table 4. Mg-ATPase activity of S1 nucleotide analog complexes

Myosin	M.ADP.AlF_4	M.ADP.BeF_x	M.ADP.V
Muscle	1.4±0.3%	0.5±0.4%	3.2±1.6%
Dicty	0.2±0.3%	0%	3.4±0.7%

100% corresponds to the value in the absence of nucleotide analog (Table 2, $V_{basal,}$ labeled).

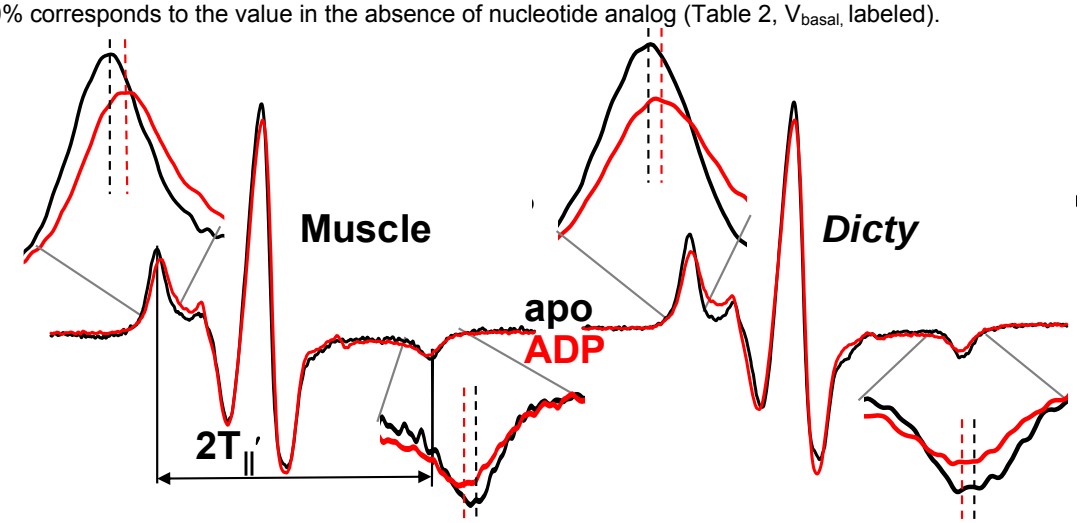

	Muscle		*Dicty*	
	$2T_{\|\|}'$	S	$2T_{\|\|}'$	S
apo	67.6 ± 0.2	0.957 ± 0.004	67.8 ± 0.2	0.960 ± 0.004
ADP	66.4 ± 0.2	0.936 ± 0.004	66.8 ± 0.2	0.943 ± 0.004

Fig. 26. EPR spectra of muscle (left) and *Dicty* (right) S1 in apo and ADP bound states.

Sensitivity of EPR Spectra to ADP. **Fig. 26** shows EPR spectra in the apo and ADP-bound states of myosin. While at first glance these spectra appear to show little or no effects of ADP, insets show the expanded low-field and high-field peaks, which show

clear ADP effects. This is important, because the splitting between the outer extrema can be used to quantitate spin label mobility. In particular, the order parameter (assuming subnanosecond rotational motion) can be calculated accurately from $S = (T_{\parallel}'-T_0)/(T_{\parallel}-T_0)$, where $2T_{\parallel}'$ is the observed splitting between the outer peaks, $2T_{\parallel}$ is the splitting for a completely immobilized label (frozen sample), and $2T_0$ is the isotropic splitting (free spin label in solution) (56). In both muscle and *Dicty*, ADP produces a narrower splitting, indicating increased spin label mobility (decreased order parameter) in this state. The position of each peak can typically be determined with an accuracy of 0.1G or less, so the value of the splitting ($2T_{\parallel}'$) can be determined with precision ± 0.2G. As the table in **Fig. 26** shows, there are no significant differences between muscle and *Dicty*, but in both cases the observed decrease in splitting due to ADP is quite significant and reflects a significant decrease in order parameter S and thus a change in myosin structure (opening of the spin label binding pocket) upon ADP binding (**Fig. 26**).

Temperature Dependence of the M*-M Transition: Calculation of Thermodynamic Parameters.** EPR spectra $V_{exp}(H)$ of myosin complexes with nucleotide analogs were recorded at different temperatures and deconvoluted to extract the mole fractions x* and x** of the spectral components corresponding to the M* and M** structural states (55) according to Eq. 22

$$V_{exp}(H) = x^*V^*(H) + x^{**}V^{**}(H), \qquad \textbf{Eq. 22}$$

where x* = [M*]/[M* + M**] and x** = 1-x* (**Fig. 27**). These mole fractions were then used to calculate the equilibrium constant K_{eq} for the reaction :

$$M^* \rightarrow M^{**}, \quad K_{eq} = [M^{**}]/[M^*] = x^{**}/x^*. \qquad \textbf{Eq. 23}$$

ΔG was calculated as $-RT \ln K_{eq}$, and the change in entropy (ΔS) and enthalpy (ΔH) between the two conformations was found by fitting the data with the the van't Hoff equation,

$$\ln K_{eq} = \Delta S/R - \Delta H/(RT), \qquad \textbf{Eq. 24}$$

as illustrated in **Fig. 28** and ***Table 3***.

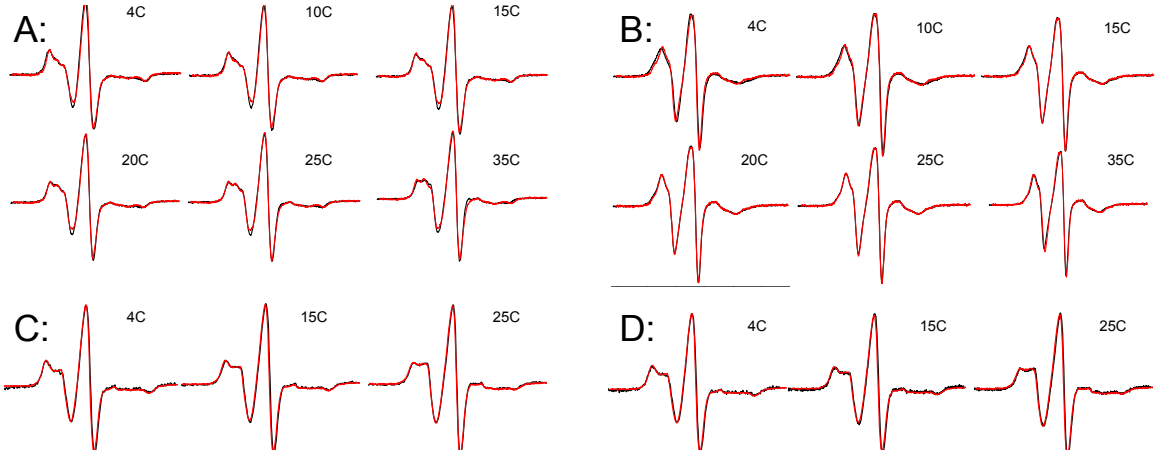

Fig. 27: EPR spectra at different temperatures.
Fit to a sum of M* and M** components **Eq. 22** obtained at the same temperature. Black: experiment. Red: best-fit simulation. A,B: muscle myosin, C,D: *Dicty* myosin; A,C: prehydrolysis analog (ADP.BeF_x), B,D: posthydrolysis analog (ADP.AlF_4).

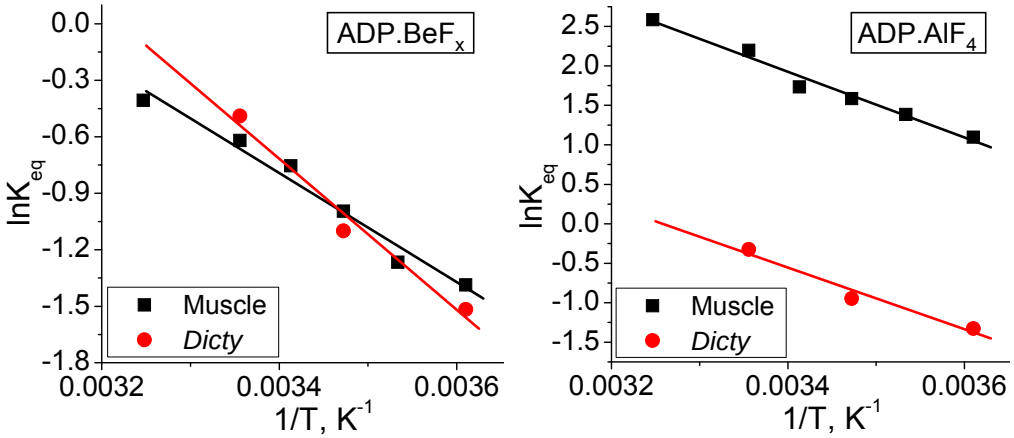

Fig. 28: Van't Hoff plots for the reaction M*→ M** (recovery stroke).
For muscle and *Dicty* myosins complexed with ADP.BeF_x (left) and ADP.AlF_4 (right). K_{eq} was determined from deconvolution of EPR spectra (**Fig. 27**), using **Eq. 22** and **Eq. 23**. Values for ΔH and ΔS, given in **Table 3**, were determined by fitting the data to Eq. **Eq. 24**, so the y-intercept is ΔS/R and the slope is -ΔH/R.

Table 5. Enthalpy (ΔH) and entropy (ΔS) change in the transition from the M* to M structural state (recovery stroke) in myosin complexed with nucleotide analogs.**

	ADP.BeF_x		ADP.AlF_4	
	ΔH, kcal/mol	ΔS, kcal/(mol·K)	ΔH, kcal/mol	ΔS, kcal/(mol·K)
Muscle	6.0±0.5	0.018±0.002	8.4±0.6	0.032±0.002
Dicty	7.8±1.2	0.026±0.004	7.8±1.5	0.025±0.005

SI Methods

ATPase assays. High-salt ATPase activity (reported in Table 1) was measured by phosphate liberation (57) at T = 25°C in buffers containing 50 mM MOPS, 5 mM EDTA, 0.6M KCl, pH 7.5 for K/EDTA ATPase, and 50 mM MOPS, 10 mM $CaCl_2$, 0.6M KCl, pH 7.5 for Ca/K ATPase (57). Myosin ATPase activity was measured under physiological conditions (T = 25°C in 10 mM Tris, 3 mM $MgCl_2$, 2.5 mM ATP, pH 7.5) in the presence and absence of actin, by the liberation of inorganic phosphate (57, Fiske, 1925 #24, 58). The dependence of S1 ATPase activity v on actin concentration was fitted to the Michaelis-Menten equation, to determine V_{max} (activity at saturating actin) and K_m (actin concentration when $v = 0.5V_{max}$), as reported in **Table 2**. Mg^{2+}-ATPase activity of IASL-S1 nucleotide analog-bound complexes was measured at T = 25°C in buffer containing 20 mM EPPS (pH 8.0), 6 mM $MgCl_2$, 1mM EGTA, 5 mM ATP, by the liberation of inorganic phosphate (57), as reported in Table S1.

Chapter 3. Structural dynamics of the myosin relay helix by time-resolved EPR and FRET

Roman V. Agafonov[1], Igor V. Negrashov[1], Yaroslav V. Tkachev[1,2], Sarah Blakely[1], Margaret A. Titus[3], David D. Thomas[1*], Yuri E. Nesmelov[1,*]

[1]Department of Biochemistry, Molecular Biology and Biophysics; [3]Department of Genetics, Cell Biology and Development, University of Minnesota Medical School, Minneapolis, MN55455
[2]Engelhardt Institute of Molecular Biology RAS Moscow, Russia

Accepted for publication in PNAS

doi: 10.1073/pnas.0909757106

http://www.pnas.org/content/early/2009/12/03/0909757106.full.pdf+html?sid=6cb96b04-0ed0-455d-896b-574352f20171

*To whom correspondence should be addressed

Keywords: myosin, relay, FRET, DEER, EPR, ESR

Abbreviations: EPR (electron paramagnetic resonance), SDSL (site-directed spin labeling), FRET (Fluorescence Resonance Energy Transfer), TR-FRET (time-resolved FRET), $(TR)^2$FRET (transient time-resolved FRET), DEER (Dipolar Electron-Electron Resonance), MSL (4-Maleimido-2,2,6,6-tetramethyl-1-piperidinyloxy spin label), IAEDANS (5-({2-[(iodoacetyl)amino]ethyl}amino)naphthalene-1-sulfonic acid), DABCYL (4 - ((4 - (dimethylamino)phenyl)azo)benzoic acid), IRF (Instrument Response Function), FWHM (full width at half maximum of Gaussian distribution of distances), RMSF (root mean square fluctuation)

3.1 Overview

We have used two complementary time-resolved spectroscopic techniques, DEER (dipolar electron-electron resonance) and FRET (fluorescence resonance energy transfer) to determine conformational changes in a single structural element of the myosin motor domain, the relay helix, before and after the recovery stroke. Two double-Cys mutants were labeled with optical probes or spin labels, and interprobe distances were determined. Both methods resolved two distinct structural states of myosin, corresponding to straight and bent conformations of the relay helix. The bent state was occupied only upon nucleotide addition, indicating that relay helix, like the entire myosin head, bends in the recovery stroke. However, saturation of myosin with nucleotide, producing a single biochemical state, did not produce a single structural state. Both straight and bent structural states of the relay helix were occupied when either ATP ($ADP.BeF_x$) or $ADP.P_i$ ($ADP.AlF_4$) analogs were bound at the active site. A greater population was found in the bent structural state when the post-hydrolysis analog $ADP.AlF_4$ was bound. We conclude that the bending of the relay helix in the recovery stroke does not require ATP hydrolysis but is favored by it. A narrower interprobe distance distribution shows ordering of the relay helix, despite its bending, during the recovery stroke, providing further insight into the dynamics of this energy-transducing structural transition.

3.2 Introduction

Myosin is a molecular motor that generates force on actin in muscle contraction, cell locomotion and intracellular trafficking. Myosin works cyclically, changing its structure twice per cycle, producing the power stroke and the recovery stroke. These structural changes are modulated by ATP binding and hydrolysis. X-ray crystal structures of myosin in different biochemical states, trapped with nucleotide analogs that are thought to mimic myosin structural intermediates, provide information about the molecular organization and sensitivity to nucleotide binding, but molecular mechanisms of structural transitions in solution remain unknown. Moreover, the relationship between the bound nucleotide and myosin crystal structure is not entirely consistent. For example, two distinct crystal structures were obtained for myosin complexed with ADP.BeF_x nucleotide analog (34, 37). It is not clear whether these differences reflect an intrinsic property of the myosin, or they simply arise from difference in crystallization conditions. As recently reviewed (1), additional insight demands site-directed labeling and spectroscopy, using crystallographic data as a starting point.

Based on myosin crystal structures (2, 7, 35) and spectroscopy (40, 59), it has been proposed that the light-chain-binding domain rotates relative to the catalytic domain, causing the myosin head to straighten in the power stroke and bend in the recovery stroke (**Fig. 29A**). These same crystal structures suggest that this transition between straight (M*) and bent (M**) structures reflects a remarkably similar transition in the relay helix (**Fig. 29B**), the 4.7-nm-long α-helix that couples

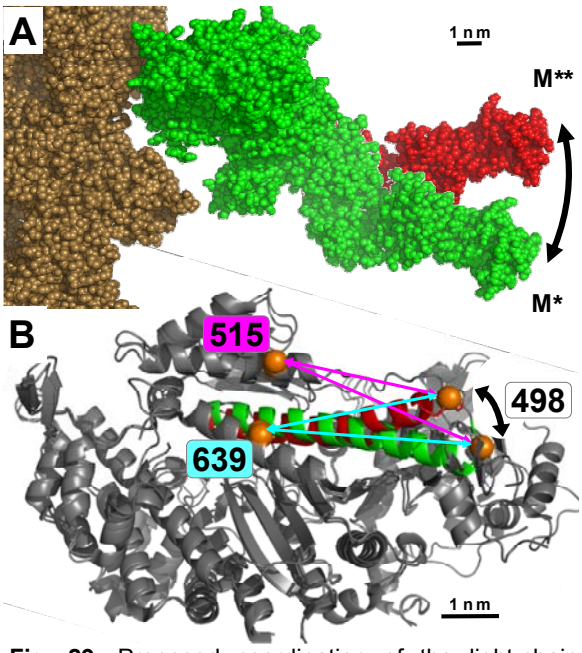

Fig. 29. Proposed coordination of the light-chain domain and the relay helix
(A) Myosin S1 bound to actin (brown) in the pre- (M*, S1 green) and post-recovery (M**, S1 red) states (1). **(B)** Myosin motor domain, overlay of crystal structures 1FMV (M*, relay helix green) and 1VOM (M**, relay helix red), showing proposed bending of the relay helix. Orange: engineered labeling sites, showing predicted shortening of distance between 639 and 498 (cyan arrows) and between 515 and 498 (magenta arrows) during the recovery stroke.

the nucleotide binding site to the light-chain domain through the converter domain (7, 35). The goal of the present study is to test this hypothesis directly in solution during the recovery stroke.

We engineered two double-Cys *Dictyostelium discoideum* (*Dicty*) myosin mutants, with one labeling site located at the C-terminus of the relay helix (K498C) and another within the stable helices on the lower 50K domain (D515C or A639C) (**Fig. 29B**). These cysteines were labeled either with a nitroxide spin label or with a donor-acceptor pair. We then measured the interprobe distances with time-resolved electron paramagnetic resonance (dipolar electron-electron resonance, DEER) and time-resolved fluorescence (fluorescence resonance energy transfer, FRET), to resolve the structural states of the relay helix in different biochemical states of myosin.

Site-directed spectroscopy has been used previously to detect nucleotide-dependent structural transitions within myosin. Fluorescence of single-Trp myosin mutants (16, 60) and EPR of spin labels attached to single-Cys sites (27, 61) have shown nucleotide-dependent changes in the local environment of labeled sites, and previous FRET studies (13, 40) have provided information about the structure of the whole myosin head, but none of these studies resolved the structural states of an individual structural element within myosin. In the present study, we have used time-resolved EPR and FRET to obtain the structural resolution needed to detect motion, disorder, and conformational heterogeneity within a single myosin subdomain - information needed to elucidate the mechanism of interdomain coupling and principles of energy transduction in myosin.

3.3 Results

Relay helix bending determined by DEER. DEER is a pulsed EPR spin echo technique that detects distance-dependent dipolar interactions between a pair of electron spins (62). Due to the R^{-3} dependence of the dipolar interaction and the time-resolved detection, this technique reports the distribution of spin-spin distances in the sample with high resolution in the range of 2 to 6 nm (5). Spin-labeled myosin was trapped in distinct biochemical states: M (apo), M.ADP, M.ATP (M.ADP.BeF_x), and M.ADP.P_i (M.ADP.AlF_4 or M.ADP.V_i), and the interprobe distance distributions were measured with DEER (**Fig. 30**). Data obtained for M.ADP.AlF_4 and M.ADP.V_i (trapping a biochemical state analogous to M.ADP.P_i) were virtually identical, so only the former analog is reported in this study. For both myosin mutants, nucleotide binding caused faster decay and oscillation of the spin echo amplitude, directly indicating a decrease in the interprobe distance. In comparison with the apo myosin state, ADP had the smallest effect on the DEER data, ADP.AlF_4 had the largest effect, and the effect of ADP.BeF_x (analog of ATP) was intermediate (**Fig. 30**).

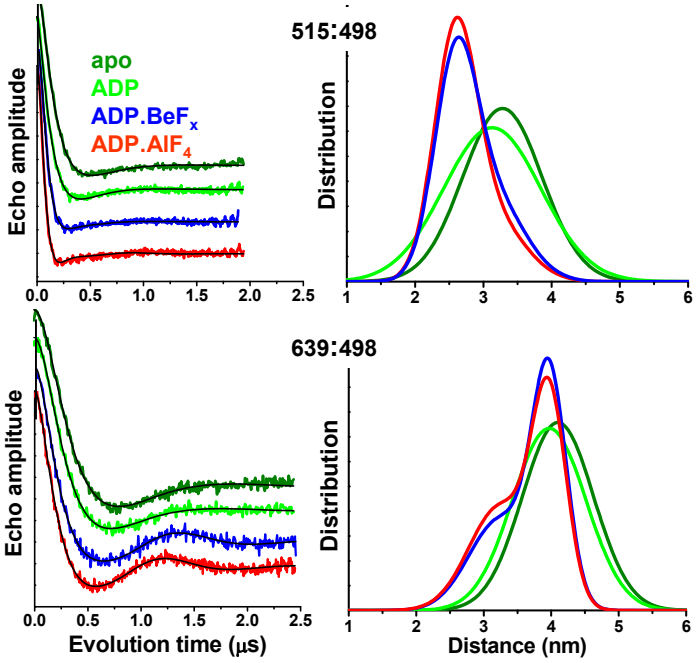

Fig. 30. Bending of the relay helix resolved by DEER. Left: Background-corrected DEER data, obtained from the indicated biochemical states, normalized to constant modulation depth and offset vertically for clarity; Right: distance distributions extracted from DEER data (M and M.ADP: one-Gaussian distribution, M.ADP.BeF_X, M.ADP.AlF_4: two-Gaussian distribution). Parameters of distributions are given in **Table 6**.

Spin echo signals were simulated and fitted to experimental data assuming Gaussian distributions of distances (**Eq. 10**). In the apo state or with bound ADP, a single Gaussian distance distribution was sufficient to produce a good-quality fit (Addition of a second Gaussian distance distribution did not improve the fit, (**Fig. 34**), indicating a single conformation of the relay helix (**Fig. 30**). The interprobe distance was longest in the apo

state, and there was a small but consistent decrease of the distance upon ADP binding. When myosin was complexed with ADP.BeF_x or ADP.AlF_4, satisfactory fits were obtained only with a two-Gaussian distance distribution, reflecting two structural states of myosin with longer and shorter distances between probes (**Fig. 34**). All long and all short distances extracted from the individual fits of the spin echo signals were similar between M.ADP, M.ADP.AlF_4, and M.ADP.Be.F_x complexes. Consequently, signals corresponding to these biochemical states were fitted globally, assuming that the same two states, M* and M** (characterized by the same interprobe mean distances *R** and *R***), were present (**Fig. 30**, **Table 6**). The quality of these fits, as judged from the χ^2 values, was comparable to that of unconstrained individual fits, indicating that only two distinct structural states were present (**Fig. 31A,C**).

Table 6. Distance distributions, R (FWHM), and mole fractions observed in each biochemical state, detected by DEER (Fig. 30).

		apo		ADP		ADP.BeF_x		ADP.AlF_4	
Con-struct	Structural state	Distance distribution R (FWHM), nm	Fraction	Distance distribution R (FWHM), nm	Fraction	Distance distribution R (FWHM), nm	Fraction	Distance distribution R (FWHM), nm	Fraction
515: 498	M	3.28 (1.36)	1.0	-	-	-	-	-	-
	M*	-	-	3.13 (1.53)	1.0	3.13 (1.10)	0.38	3.13 (1.10)	0.28
	M**	-	-	-	-	2.59 (0.73)	0.62	2.59 (0.73)	0.72
639: 498	M	4.10 (1.24)	1.0	-	-	-	-	-	-
	M*	-	-	3.97 (1.28)	1.0	3.97 (1.08)	0.58	3.97 (1.08)	0.52
	M**	-	-	-	-	3.24 (0.59)	0.42	3.24 (0.59)	0.48

R, mean distance; FWHM – full width of the Gaussian distribution at half maximum (Eq. 1); Fraction, mole fraction (X, X*, X**) of myosin occupying a given structural state (M, M*, M**).

Relay helix becomes more ordered during the recovery stroke. Nucleotide analogs of ATP and ADP.P_i clearly induce not only faster decay rates, but also more pronounced oscillations of the spin echo decay (especially for 639:498, **Fig. 30**, bottom), indicating narrower interprobe distance distributions, compared with apo or ADP-bound states (**Fig. 30**, right). As illustrated in **Fig. 31**, it was not possible to fit the data satisfactorily assuming that the widths of the distributions did not change during the myosin structural

transition (compare **Fig. 31A** and **Fig. 31B)**. If the width of the M* distribution was allowed to vary, the quality of global fits was equivalent to the quality of unrestricted fits (compare **Fig. 31A** and **Fig. 31C**). We found that structural flexibility (characterized by the width of the distance distribution) in the M* state was less in the M.ADP.BeF_x and ADP.AlF_4 complexes compared to the M.ADP complex. The width of the distance distribution was even narrower in the M** structural state (**Fig. 30**, right; and **Table 6**).

Relay helix bending determined by TR-FRET. FRET detects the distance R between donor and acceptor probes, coupled by nonradiative energy transfer. As a result of this energy transfer, the rate of the donor's fluorescence decay is increased in proportion to R^{-6}. In the time-resolved FRET (TR-FRET) experiment, the donor is excited with a nanosecond laser pulse, its fluorescence is detected with subnanosecond resolution, and the fluorescence lifetime τ is used to calculate the distance R. The major advantage of TR-FRET, compared to conventional FRET (where only steady-state fluorescence intensity is measured), is the ability to resolve multiple protein conformations with distinct interprobe distances, which result in distinct lifetimes(63). Fluorescence signals of donor only (IAEDANS) and donor-acceptor (IAEDANS-DABCYL) labeled myosin

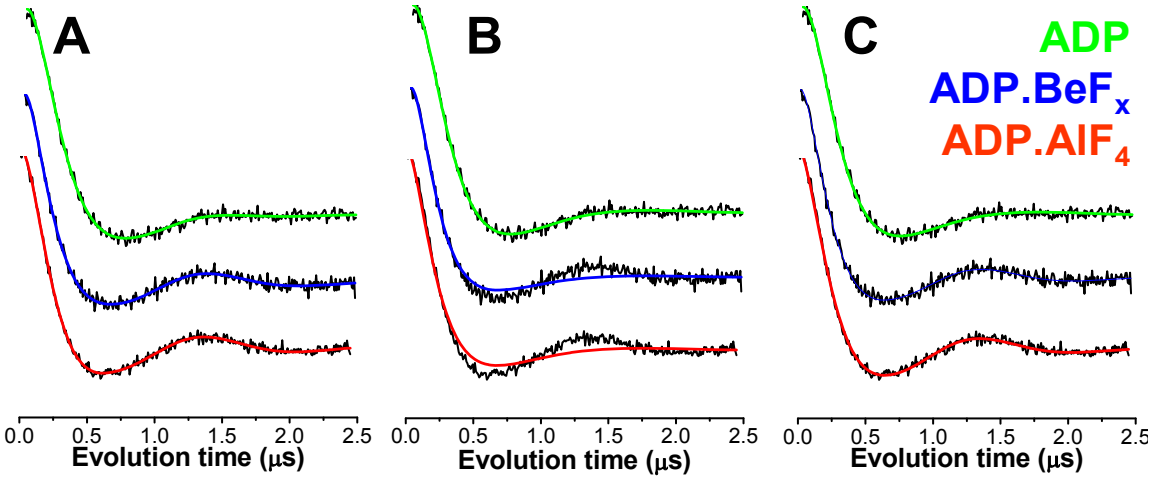

Fig. 31. Fitting of DEER signals in different biochemical states of myosin (639:498 mutant).
(A) Each signal was fitted independently. **(B)** All signals were fitted globally, using one set of parameters: R*, R**, FWHM*, FWHM**. **(C)** All signals were fitted globally using one set of parameters, except that FWHM* for M.ADP was allowed to be different from that for M.ADP.BeF_x and M.ADP.AlF_4. We conclude that the two structural states M* and M** have the same mean distances R* and R** in all three biochemical states, but the width FWHM* of the M* distribution is less in the nucleotide analog biochemical states. The parameters derived from these best fits are summarized in **Table 6**.

mutants were acquired in different biochemical states: apo, M.ADP, M.ADP.BeF_x (M.ATP) and M.ADP.AlF_4 (M.ADP.P) (**Fig. 32**, left). Unlike DEER, TR-FRET was insensitive to ADP binding (**Fig. 32**), probably due to FRET's inferior distance resolution and due to the larger size and greater flexibility of attached optical probes. However, binding of ADP.BeF_x and ADP.AlF_4 to myosin substantially decreased the donor lifetime, indicating an increase in FRET efficiency and shortening of the mean distance between probes (**Fig. 32**), as observed by DEER (**Fig. 30**).

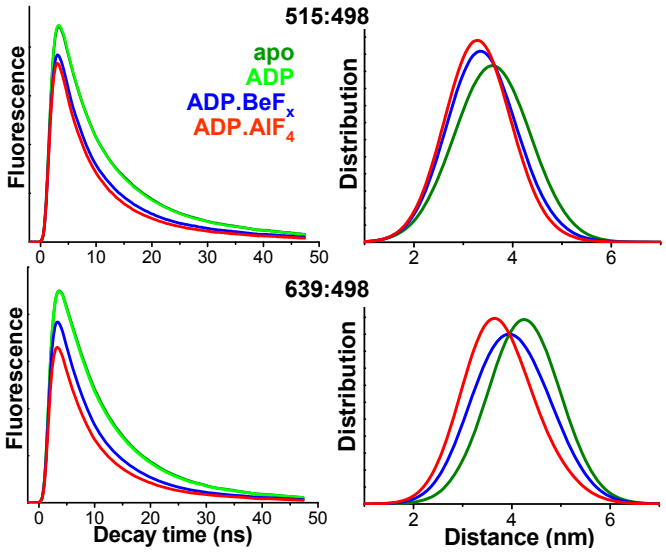

Fig. 32. Bending of the relay helix resolved by TR-FRET. Left: Fluorescence signals of donor-acceptor labeled myosin mutants in the biochemical states indicated. Right: distance distributions obtained by fitting fluorescence signals.

Donor fluorescence signals for all four biochemical states were fitted globally

Table 7 Distance distributions, R (FWHM), and mole fractions observed in each biochemical state, detected by TR-FRET (Fig. 32).

		apo		ADP		ADP.BeF_x		ADP.AlF_4	
Con-struct	Structural state	Distance distribution R (FWHM), nm	Fraction	Distance distribution R (FWHM), nm	Fraction	Distance distribution R (FWHM), nm	Fraction	Distance distribution R (FWHM), nm	Fraction
515: 498	M	3.59 (1.82)	1.0	-	-	-	-	-	-
	M*	-	-	3.59 (1.82)	1.0	3.59 (1.82)	0.45	3.59 (1.82)	0.21
	M**	-	-	-	-	3.24 (1.51)	0.55	3.24 (1.51)	0.79
639: 498	M	4.25 (1.73)	1.0	-	-	-	-	-	-
	M*	-	-	4.25 (1.73)	1.0	4.25 (1.73)	0.67	4.25 (1.73)	0.34
	M**	-	-	-	-	3.51 (1.46)	0.33	3.51 (1.46)	0.66

R, mean distance; FWHM – full width of the Gaussian distribution at half maximum (Eq. 1); Fraction, mole fraction (X, X*, X**) of myosin occupying a given structural state (M, M*, M**).

(assuming the presence of the same two structural states: M* and M**) according to **Eq. 26 - Eq. 30** (**Fig. 32**). Based on comparison of residuals and χ^2 values for a one- and two-Gaussian fits (**Fig. 36**) we concluded that a single structural state is populated in the apo and M.ADP biochemical states, and two structural states are populated with bound

$ADP.BeF_x$ and $ADP.AlF_4$. The mole fractions of myosin populations, interprobe distances, and distance distributions extracted from the fits are shown in (**Fig. 32**) and **Table 7**.

3.4 Discussion

The goal of this study was to determine the structure of the relay helix during the dynamic myosin-nucleotide interaction in solution. The relay helix, an essential element of the force-generating region of myosin, connects the nucleotide binding site and the converter domain. Crystal structures of myosin show two distinct conformations of the relay helix, dependent on the bound nucleotide analog. It is widely assumed that the transition between these myosin conformations, initiated by the myosin-ATP interaction, is the recovery stroke. In this study we ask the following questions: How many structural states are adopted by the relay helix in solution? Is there direct correlation between the state of the nucleotide-binding pocket and the state of the relay helix? How rigid is the relay helix? What initiates the myosin recovery stroke, ATP binding or ATP hydrolysis? We used two complementary spectroscopic probe methods, DEER and FRET, which both use pulsed excitation and time-resolved detection to obtain structural resolution. For both techniques, two pairs of labeling sites were used to triangulate probe positions in different biochemical states of myosin and unambiguously resolve myosin structural states.

Relay helix adopts two structural states in myosin-nucleotide complexes. Both DEER and TR-FRET data were in remarkable agreement (**Table 8**). Both techniques show the presence of two structural states of myosin (M* and M**) in a single biochemical (myosin-nucleotide analog) state. These structural states were populated differently, depending on the nucleotide analog bound ($ADP.AlF_4$, $ADP.BeF_x$). Apo myosin exhibited one distinct structural state, M. The myosin-ADP biochemical state exhibited a single structural state, M*. The interprobe distance in the M* state was only ~0.15 nm shorter than in the M state, indicating a subtle change in the

Table 8. Interprobe distances (nm) in pre- (M*) and post-recovery stroke (M) states of myosin determined by different techniques.**

		M*	M**	**M*- M****
515:498	X-Ray†	3.85	3.12	**0.73**
	DEER	3.13	2.59	**0.54**
	FRET	3.59	3.24	**0.35**
639:498	X-Ray†	3.89	3.27	**0.62**
	DEER	3.97	3.24	**0.73**
	FRET	4.25	3.51	**0.74**

†β-carbon – β-carbon distances from 1MMD & 1VOM structures

relay helix structure after binding of ADP. Only DEER resolves clearly the structural change between M and M* states, probably due to its superior distance resolution and to the smaller size of the spin label, compared to the FRET probes. The interprobe distance difference between M* and M** structural states is much more pronounced (~0.5 nm), reflecting a substantial conformational change of the relay helix. We conclude that there are only two distinct structural states of the force-generating region of myosin in M.ATP and M.ADP.Pi biochemical states, M* and M**. This observation resolves the controversy raised by the observation of two different crystal structures for the same myosin complexed with the same nucleotide analog (ADP.BeF_x) (34, 37). Our results show that both structural states are occupied in solution, so the structure trapped by crystallization probably depends on the specific experimental conditions used for protein preparation and crystal growth.

The force-generating region of myosin is more ordered in the post-recovery structural state. Analysis of the interprobe distance distribution in M* and M** structural states shows a narrower width in the post-recovery stroke state M**, indicating more order in the force-generating region of myosin. In agreement with these experimental results, the simulations of myosin molecular dynamics (MD) showed decreased backbone fluctuations in the relay helix in the transition from M* to M** **(Fig. 33)**. In contrast, MD showed no significant effect of this transition on backbone fluctuations at other sites in the lower 50K domain, including the D515 and A639 labeling sites. The N-terminal part of the relay helix is a continuation of the switch II loop, an essential structural element of the nucleotide-binding site of myosin; switch II is open in M* and closed in M**. The experimentally observed narrower distance distribution in the M** structural state (**Fig. 30**, **Table 6**), confirmed by decreased

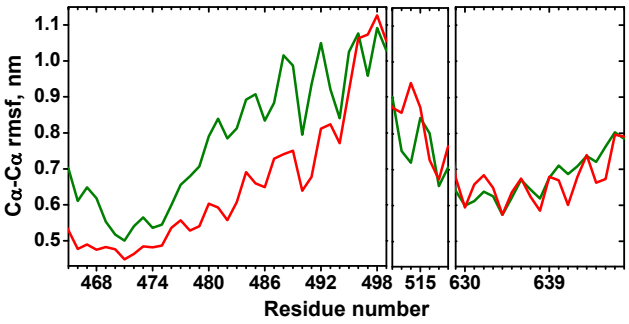

Fig. 33. Simulated backbone fluctuations in myosin. Pre- (green) and post-recovery stroke (red) structural states. Significant differences are seen only in the relay helix (residues 465 -499).

backbone RMSF in MD simulations, reflects the closure of switch II and stronger nucleotide binding.

ATP binding initiates the recovery stroke. Our results show that the relay helix responds to changes in the state of the nucleotide binding pocket and identify the relay helix as an interdomain linker that propagates changes from the active site to the converter domain of myosin. Strikingly, we found that with an ATP analog (ADP.BeF_x) bound at the active site, the myosin relay helix can adopt both pre- and post-recovery structural states. In contrast to the classic model of myosin function, in which ATP hydrolysis is coupled to a recovery stroke and serves as its driving force, our observations show that ATP binding plays the crucial role in the recovery stroke. The recovery stroke precedes hydrolysis and occurs with ATP bound in the active site. Consequently, hydrolysis is needed not to fuel the recovery stroke but to facilitate product release and continue the cycle. This hypothesis was previously proposed based on molecular dynamics simulations (9, 64)and crystal structures, which suggested that switch II in the nucleotide pocket must be closed for myosin to be in the catalytically active form (4, 7). Relaxation experiments with single Trp mutants and nucleotide analogs (65) showed changes in intrinsic myosin fluorescence after rapid jump in temperature or pressure. This was attributed to the presence of an equilibrium between the open (pre-recovery) and closed (post-recovery) conformations and was used to calculate the equilibrium constants between states. Our distance measurements provide the necessary dimensional details to resolve the two coexisting structural states and determine directly the position of the relay helix in each of the states.

DEER and TR-FRET are complementary. While the two methods both use pulsed excitation and time-resolved detection, and utilized the same labeling sites, each has distinct advantages. Compared to relatively simple exponential decays of donor fluorescence in FRET experiments, the complex shape of modulated echo intensity signals in DEER has more distinct spectral features that can be used to evaluate the quality of the fit, providing higher structural resolution. Another DEER advantage is in

labeling: the smaller probe size and the ability to use the same probe at both locations (compared to donor-acceptor pairs in FRET) simplify sample preparation and result in more reliable data interpretation. In particular, only DEER detected subtle (~0.1 nm) changes in structure upon binding of ADP, showed a significant decrease in distribution width in the M.ADP.BeF_x and M.ADP.AlF_4 states, and unambiguously resolved two structural states in myosin-nucleotide analog complexes. On the other hand, TR-FRET experiments can be performed at physiological temperatures and have several orders of magnitude higher sensitivity, yielding information about the distance distribution in a single 50 ns signal, detected with subnanosecond resolution. Thus FRET has the potential to provide this structural resolution in real time during a biochemical transient. In addition, the FRET measurements can be used to establish an upper bound for the transition rate between the resolved conformations, which is approximately the inverse of the average observed fluorescence lifetime. For example, the two conformations resolved in **Table 7** must be exchanging more slowly than approximately 10^8 s^{-1}.

3.5 Conclusions

We have designed myosin constructs to measure nucleotide-induced dynamics of the myosin relay helix, an important structural element in the force-generating region, connecting the nucleotide binding site and the lever arm. Combining protein mutagenesis, site-directed labeling, high-resolution pulsed EPR spectroscopy (DEER), and high-sensitivity fluorescence spectroscopy (TR-FRET) we (a) detected structural changes (bending and ordering) in the myosin relay helix in response to nucleotide analog binding, (b) resolved two structural states (straight and bent) of the relay helix in a single biochemical state of myosin with bound nucleotide analog, and (c) detected changes in order as well as in interprobe distances during the myosin–ATP interaction. Mutagenesis and labeling did not disturb myosin function significantly. We conclude that the bent state of the relay helix is populated immediately upon ATP binding to myosin, without requiring ATP hydrolysis. The wider distribution of interprobe distances in the pre-recovery stroke states indicates flexibility of the N-terminal part of the relay helix, when the switch II loop in the nucleotide binding site is open. These results provide direct

information about the structural dynamics of the relay helix in myosin in solution, providing insight into the interaction between myosin's active site and force-generating region.

3.6 Material and Methods

Protein Preparation and Labeling. Mutants of *Dictyostelium discoideum* myosin were constructed and purified as described previously(54). For DEER, the protein was labeled with MSL by incubating 100 μM myosin with 600 μM MSL for 12 hours on ice, resulting in labeling of over 90% of Cys, as measured by mass spectrometry and spectral intensity. For FRET, the protein was labeled in two steps. First, 50μM myosin was incubated with 45μM donor (IAEDANS) for 12 hours. Then this protein was diluted to 25 μM and incubated with 100μM acceptor (DABCYL). After each labeling step, unreacted label was removed with size-exclusion spin columns (Pierce). The extent of FRET labeling, determined from dye absorbance, was typically approximately 30-40% donor and 60-70% acceptor, with virtually all cysteines being labeled. Labeling buffer contained 20mM MOPS, 50mM KCl, 3mM $MgCl_2$, 1mM EDTA, pH 7.5. Complexes of myosin with nucleotide analogs were obtained as described previously(61). Unless indicated otherwise, all experiments were performed at 20C in a buffer containing 20mM EPPS, 6mM $MgCl_2$, 1mM EGTA, pH 8.0

ATPase assays. Myosin ATPase activity was measured in physiological buffer (T = 25°C in 10 mM Tris, 3 mM $MgCl_2$, 5 mM ATP, pH 7.5) in the presence and absence of actin, by the liberation of inorganic phosphate(57). The dependence of myosin ATPase activity on actin concentration was fitted by the Michaelis-Menten equation, to determine V_{max} (activity at saturating actin) and K_m (actin concentration at $V = 0.5V_{max}$) (details in **Table S1)**.

Interprobe distance distribution. To reflect flexibility in the protein structure, both DEER and FRET signals were simulated using a set of distance distributions rather than a set of discrete distances. The shape of each distribution was assumed to be Gaussian:

$$\rho(r) = \frac{1}{\sigma\sqrt{2\pi}} \exp\left(-\frac{(r-R)^2}{2\sigma^2}\right),\ \sigma = \frac{FWHM}{2\sqrt{2\ln 2}}, \qquad \textbf{Eq. 25}$$

where σ is the standard deviation and FWHM is the full width at half maximum.

DEER. Time-resolved dipolar electron-electron resonance signals were acquired with an Elexsys E580 spectrometer (Bruker Biospin, Billerica, MA) equipped with a dielectric resonator (MD-5, Bruker Biospin, Billerica, MA), using a 4-pulse DEER sequence (21) with a 16 ns $\pi/2$ pulse, and a 40-48 ns ELDOR pulse. The pump frequency was centered on the central resonance of the nitroxide spin label, and the observe frequency was set to the low-field resonance 67 MHz away. Temperature during the acquisition was set to 65° K. Myosin samples (50-75μM) were flash-frozen in liquid nitrogen before being placed in the spectrometer. Buffer contained 20 mM EPPS, 6 mM $MgCl_2$, 1mM EGTA and 10% glycerol (pH 8.0). Spin echo signals were analyzed with the DeerAnalysis software suite(23), which fits simulated DEER signals to the data, assuming one or two Gaussian interprobe distance distributions (**Eq. 10**).

TR-FRET. Fluorescence of AEDANS-myosin was excited with the 3rd harmonics of a passively Q-switched microchip YAG laser (NanoUV-355, JDS Uniphase), operated at a pulse repetition rate of 10 kHz, and selected with a 420 nm long-pass glass filter. To avoid anisotropy effects, fluorescence was passed through a polarizer oriented at the magic angle. Fluorescence signals were detected after every laser shot with a photomultiplier module Hamamatsu H5773-20 (rise time 0.78ns) and acquired with a transient digitizer (Acqiris DC252, Geneva, Switzerland) with sampling resolution 0.125 ns. The Instrument Response Function (IRF) was acquired with scattered light at the same instrument settings as in the fluorescence measurement, except that there was no emission filter and the emission polarization was vertical.

Analysis of TR-FRET data. The observed donor-only fluorescence signal $F_{\mathrm{Dobs}}(t)$ from labeled myosin was fitted by a simulation $F_{\mathrm{Dsim}}(t)$, consisting of a multiexponential decay $F_{\mathrm{D}}(t)$, convolved with the IRF:

$$F_D(t) = \sum_{i=1}^{n} A_i \exp\left(-\frac{t}{\tau_{Di}}\right), \qquad \textbf{Eq. 26}$$

$$F_{D,sim}(t) = \int_{-\infty}^{+\infty} IRF(t-t') \cdot F_D(t')dt' \ , \qquad \textbf{Eq. 27}$$

where τ_{Di} are the donor-only fluorescence lifetimes. We found that two exponential components ($n = 2$ in **Eq. 26**) were sufficient. I.e., addition of a third component to the fit did not reduce the residual or χ^2. For each biochemical state the fluorescence signal of donor-acceptor labeled myosin before convolution, $F_{DA}(t)$, was analyzed by assuming that the only change in $F_D(t)$ was an increased rate of decay due to energy transfer $k_T = \int k_{Di}[\rho(r)/R_{oi}]^{-6} dr$, where $\rho(r)$ is the donor-acceptor distance distribution (**Eq. 10**), $k_{Di} = 1/\tau_{Di}$, and R_{0i} is the Förster distance defined by (**Eq. 31**)

$$F_{DA}(t) = \int_{-\infty}^{+\infty} \rho(r) \cdot \sum_{i=1}^{n} A_i \exp\left(-\frac{t}{\tau_{Di}} - \frac{t}{\tau_{Di}} \left(\frac{R_{0i}}{r} \right)^6 \right) dr , \qquad \textbf{Eq. 28}$$

The observed donor-acceptor fluorescence signal before convolution, $F_{D+A}(t)$, was assumed to be a sum of three terms:

$$F_{D+A}(t) = X_D \cdot F_D(t) + X^* \cdot F_{DA}^*(t, R^*, FWHM^*) + X^{**} \cdot F_{DA}^{**}(t, R^{**}, FWHM^{**}), \qquad \textbf{Eq. 29}$$

$$F_{D+A,sim}(t) = \int_{-\infty}^{+\infty} IRF(t - t') \cdot F_{D+A}(t') dt' , \qquad \textbf{Eq. 30}$$

where X^* and X^{**} ($X^* + X^{**} = 1$) are mole fractions of myosin in the prerecovery (straight relay helix) and postrecovery (bent relay helix) state, and X_D is the mole fraction of donor-only labeled myosin ($X_D + X_{DA} = 1$).

Observed fluorescence signals in the presence and absence of acceptor were fitted globally (simultaneously) by the simulated expressions in **Eq. 27** and **Eq. 30**. Intensities A_i, lifetimes τ_i, distances R^* and R^{**}, widths FWHM* and FWHM**, and the fraction X_D of donor-only labeled myosin were linked and varied simultaneously. X^{**} (the fraction of the M^{**} structural state) was varied independently for every signal in the global fit.

Acknowledgments

This work was supported by NIH grants AR32961 (DDT) and AR53562 (YEN), and a grant from the Minnesota Medical Foundation (YEN). MD simulations were performed using computational resources of the University of Minnesota Supercomputing Institute. We appreciate excellent technical assistance from Eunice Song and Octavian Cornea.

Author contributions

Y.E.N, R.V.A., and D.D.T designed the research; R.V.A. and Y.E.N. performed the experiments; I.V.N. designed and constructed the TR-FRET instrument, S.B. and M.A.T. contributed new reagents/analytic tools, Y.V.T. performed MD simulations and analysis; R.V.A. and Y.E.N. analyzed data; and R.V.A., D.D.T. and Y.E.N wrote the paper.

3.7 Supporting information

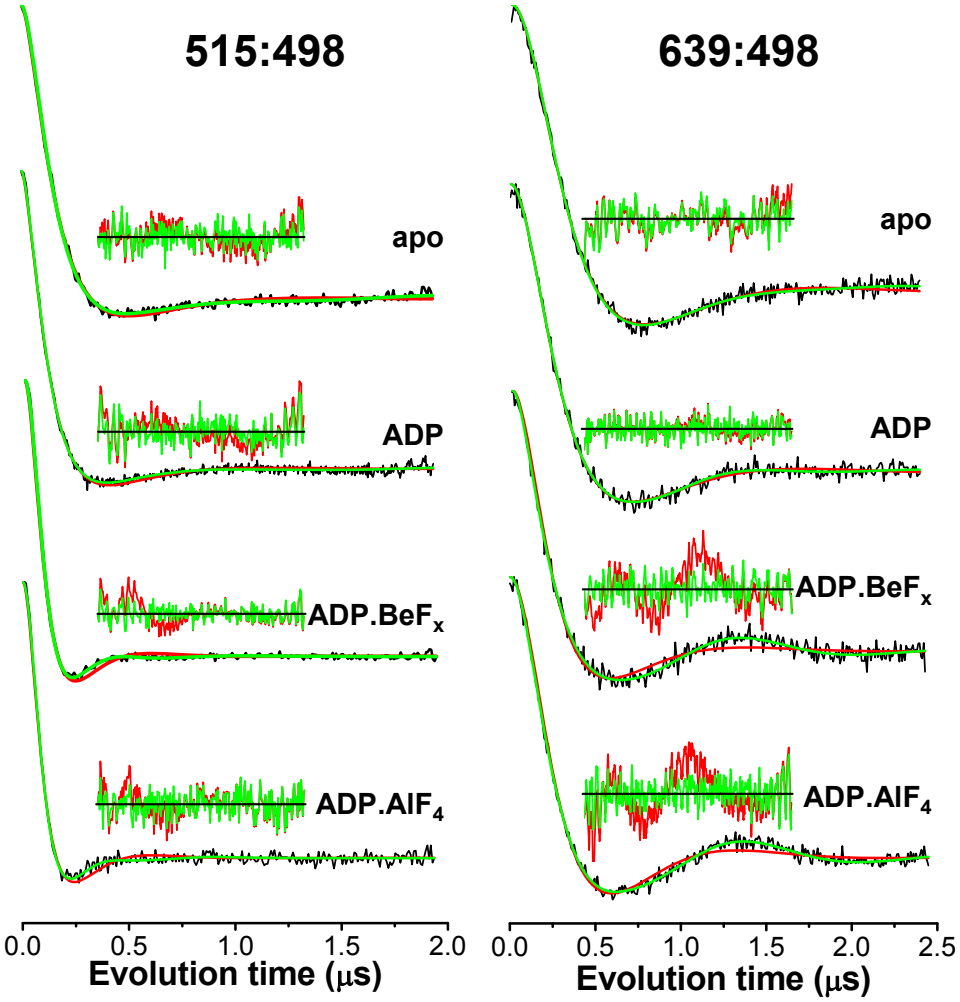

Fig. 34. Fitting DEER signals in different biochemical states of myosin.
Insets show residuals for fits to one (red) and two (green) Gaussian distance distributions (**Eq. 25**). These results show that one Gaussian (structural state) was sufficient to describe the apo and M.ADP biochemical states, but two Gaussians (structural states) were needed to describe the M.ADP.BeF_x and M.ADP.AlF_4 biochemical states. The parameters derived from these best fits are summarized in **Table 6**.

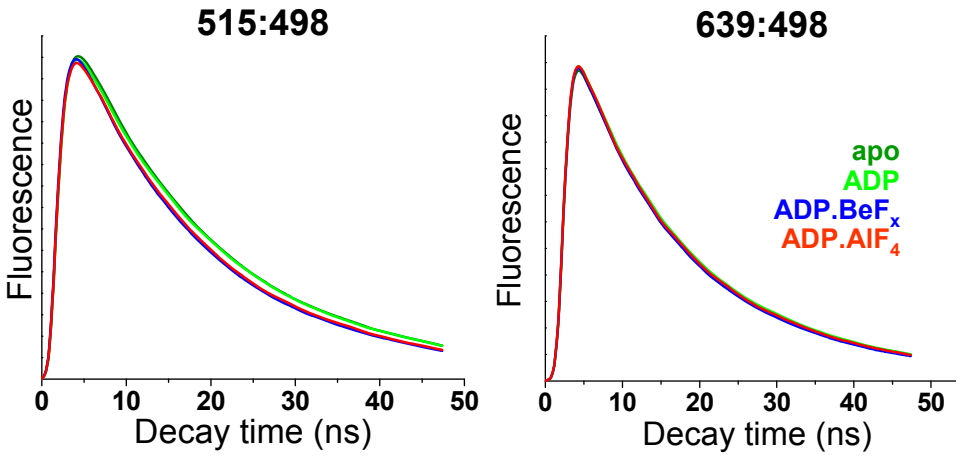

Fig. 35. Waveforms of the IAEDANS labeled myosin in different biochemical states. Binding of ADP and nucleotide analogs had marginal effect on fluorescence indicating minimal changes in the local environment.

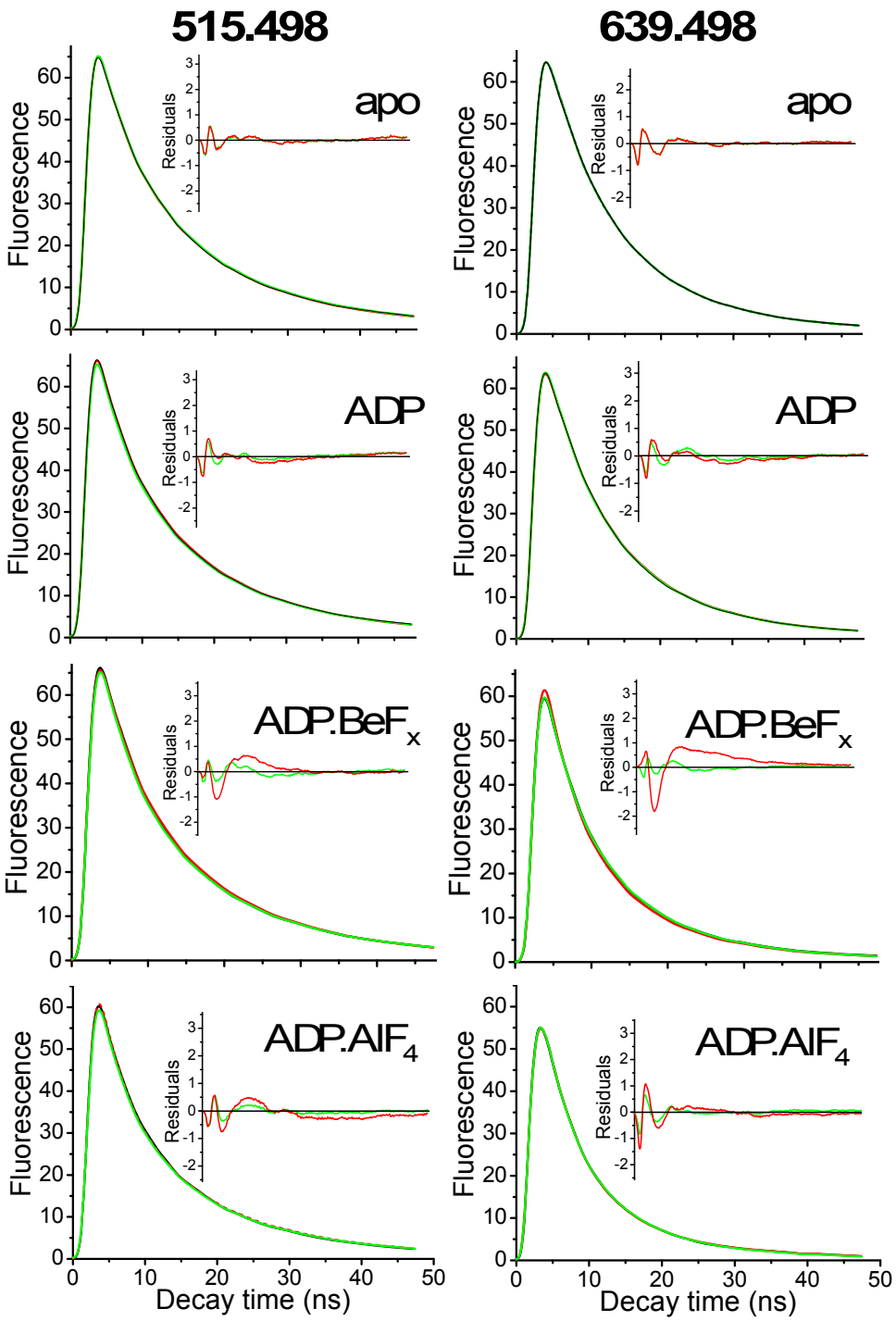

Fig. 36 Fitting FRET signals in different biochemical states of myosin, according to **Eq. 25**- **Eq. 30**.
Insets show residuals for fits to one (red) and two (green) Gaussian distance distributions. The parameters derived from these best fits are summarized in **Table 7**.

SI METHODS

Functional properties of labeled myosin

Myosin ATPase rates were measured to evaluate the effects of mutations and labels. Both basal and actin-activated ATPase activities were comparable (within a factor of 2) between unlabeled and labeled proteins and were also comparable to values reported for other *Dicty* constructs (0.04-0.15s^{-1} and 1.2-4.8 s^{-1} for basal and actin-activated ATPase rates respectively) (16, 46, 54, 61), indicating that neither mutations nor labeling caused substantial effects on myosin catalytic activity **(Table 9).**

Table 9 Effect of labeling on functional properties of *Dicty* myosin

ATPase rate	myosin	D515C:K498C	A639C:K498C
V_{basal}, s^{-1}	unlabeled	0.15	0.17
	labeled	0.08	0.10
V_{max}, s^{-1}	unlabeled	3.8	4.4
	labeled	2.5	5.1

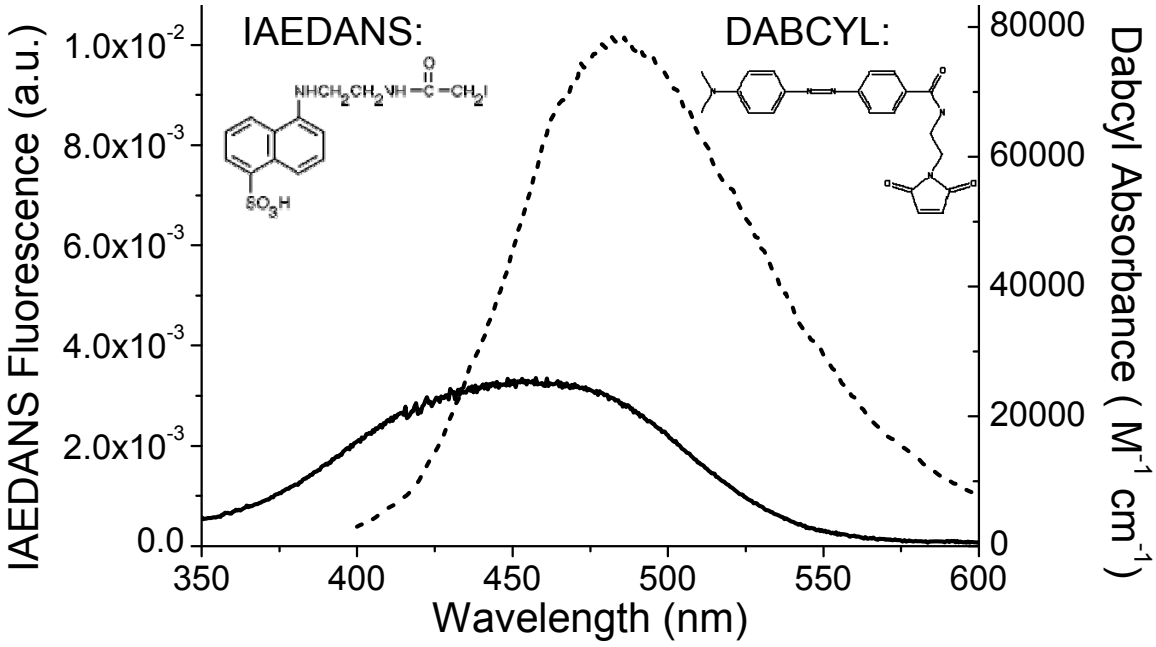

Fig. 37. Donor (IAEDANS) emission (dashed line)and acceptor (Dabcyl) absorbance (solid line) spectra.

Förster distance calculation. The Förster distance R_{0i} was calculated from

$$R_{0i} = 9786[J(\lambda)\kappa^2\eta^{-4}Q_{Di}]^{1/6}, \qquad \textbf{Eq. 31}$$

where λ is the wavelength, $J(\lambda)$ is the spectral overlap integral between normalized donor emission spectrum $F_D(\lambda)$ and the acceptor absorption spectrum $\varepsilon_A(\lambda)$ (**Fig. 37**), $\kappa^2 = 2/3$ is the labels orientation factor, $\eta = 1.4$ is the index of refraction of the medium, Q_{Di} is the donor quantum yield given by $Q_{Di} = \langle Q_D\rangle * \tau_{Di}/\langle\tau\rangle$, where $\langle\tau\rangle = (1/n)\sum_{i=1}^{n} A_i\tau_{Di}$. The mean quantum yield of donor-only labeled myosin ($\langle Q_D\rangle = 0.32 \pm 0.015$) was measured by comparison with the quantum yield of quinine sulfate in 0.05M H_2SO_4 at λ_{ex} = 347.5nm (Q_S=0.51 (66)), according to the equation: $Q_D = Q_S*(F_D(\lambda)/A_D(\lambda))/(F_S(\lambda)/A_S(\lambda))$, where $F_i(\lambda)$ is the integral emission and $A_i(\lambda)$ is the absorbance at the excitation wavelength of donor-labeled myosin or quinine sulfate.

Molecular dynamics simulations

The X-ray crystal structures of *Dicty* myosin II motor domain complexed with Mg ADP BeF_x and Mg ADP AlF_4 (PDB codes 1W9K and 1W9L (67)) were used for MD simulations of the pre- and post-recovery stroke structural states. 1W9K and 1W9L atomic structures were chosen because of resolved atoms in the relay helix and the relay loop, the subject of our study. Mutations have been replaced with native residues, according to DictyBase sequence database (68). The reconstruction of missing segments (1W9K: 22-30, 203-208, 704-716; 1W9L: 203-209, 706-714, 728-732) was done by homology modeling using Swiss-Model server (69) in multiple sequence alignment mode, with 1MMD (34) and 1FMV (35) atomic structures as additional templates. The nucleotide analog was replaced with ATP in both 1W9K and 1W9L structures. The resulting structure was placed into a 13.5 nm x 11.5 nm x 9.5 nm box, solvated with water (using the TIP3 model (70)) and ions at a concentration 0.15M. Calculations was done with NAMD molecular dynamics software (71) using periodical boundary conditions with the Ewald summation method. Simulations were performed at constant pressure and controlled temperature (NPT) using a combination of the Nose-Hoover

constant pressure method (72) and fluctuation control using Langevin dynamics(73). All bonds involving hydrogen atoms were kept rigid using the SHAKE algorithm (74). This allowed integrator time step to be set to 2 fs. Myosin structures were energy-minimized, heated to 300K and equilibrated with C□ and Mg atoms harmonically restrained to positions in the initial structure. Then, volume equilibration was performed and constraints were gradually released. Unconstrained equilibration was run for 6 ns. Finally, 12 ns trajectories were obtained by NPT simulation at 300K and 101.325 kPa. Trajectory analysis was done with VMD software (75). The per-residue RMSF values were calculated according to **Eq. 32** for all frames in the trajectory (N = 6000 frames).

$$RMSF_i = \left[\sum_{k=1}^{N} (x_i(k) - \bar{x}_i)^2 + (y_i(k) - \bar{y}_i)^2 + (z_i(k) - \bar{z}_i)^2 \right]^{\frac{1}{2}} \quad \textbf{Eq. 32}$$

where i is the residue index, (x, y, z) contains the C_α coordinates, and the overbar indicates a time average.

Chapter 4. Transient time-resolved FRET: myosin structural dynamics in real time

4.1 Overview

We have used a newly developed transient time-resolved fluorescence resonance energy transfer [$(TR)^2$FRET] technique to determine conformational changes in a single structural element of the myosin motor domain, the relay helix, in real time during the recovery stroke. $(TR)^2$FRET combines TR-FRET with a stopped-flow apparatus, providing high resolution structural data in real time during the course of a biochemical reaction. In agreement with previous steady-state measurements, two structural states of myosin during the recovery stroke, corresponding to straight and bent conformations of the relay helix were resolved. Observed structural transition was biphasic, with the first (fast) phase corresponding to the closure of the nucleotide binding pocket and bending of the relay helix; and the second (slower) phase corresponding to ATP hydrolysis. ATP hydrolysis was not associated with a specific conformational change, but it pulled the equilibrium toward the post-recovery myosin conformation (bent relay helix).

4.2 Introduction

As discussed in the previous chapter, the relay helix is a key element of the myosin force-generation domain. To investigate its role in coupling between the active site and the converter we developed a spectroscopic assay that allowed us to monitor relay helix conformation in response to nucleotide binding. Our steady-state experiments have resolved two conformation of the relay helix, and showed that both conformations can coexist in solution in the presence of ATP and ADP.P_i nucleotide analogs (**Fig. 38**, **c,f**).

At the same time of a greater interest is the question: what happens with the relay

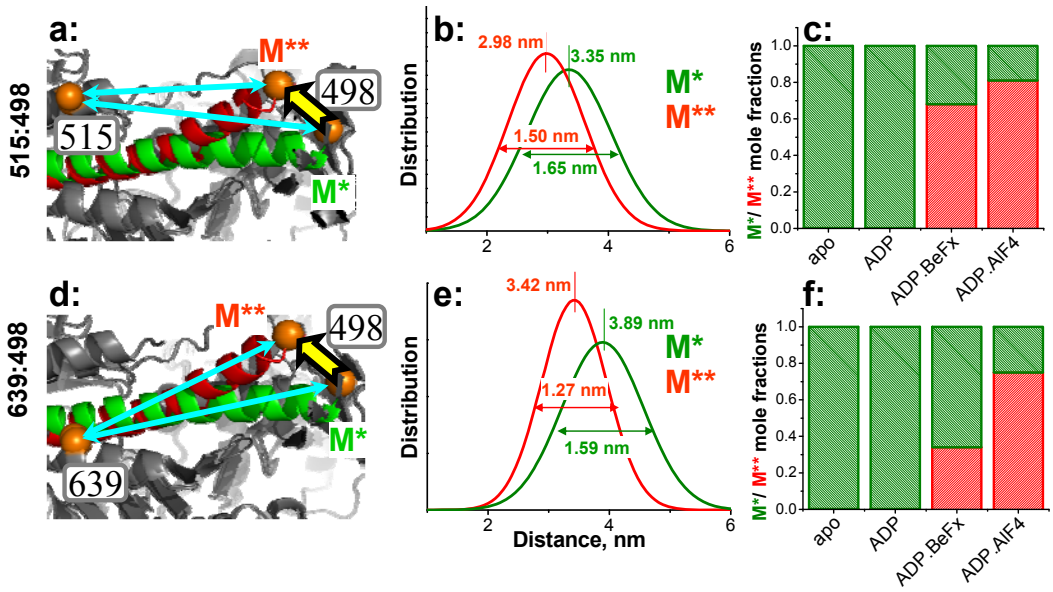

Fig. 38 Two structural states of myosin (M* and M**) with straight and bent relay helix, resolved in the steady-state experiments with nucleotide analogs. (a) and (d): labeling sites used to monitor the relay helix conformation; (b) and (e) interprobe distance distributions in M* and M** structural states; (c) and (f) mole fractions of myosin occupying the M* and M** structural states in myosin-nucleotide complexes.

helix during its transient interaction with ATP? Does it adopt a novel "transient" conformation that is not observed in crystal structures or in solution experiments with nucleotide analogs? How fast is the structural transition and at what step of the ATPase cycle does it occur? Previous kinetic studies of the force-generating region were mainly limited to observation of fluorescence of single-Trp myosin mutants that have reflected nucleotide-dependent changes in the local environment (16, 76) but did not provide direct information about the movements of structural elements within myosin. EPR (27) and

FRET (40, 76) have provided transient data or structural resolution, but not both simultaneously.

To answer these questions we took advantage of the remarkable sensitivity and structural resolution of TR-FRET. We have complemented our steady-state fluorimeter with a stopped-flow apparatus, which enabled us to perform rapid mixing experiments and observe structural evolution of the relay helix in time. The same myosin constructs (515:4908 and 639:498) and the same dye pair (IAEDANS-Dabcyl) have been used (**Fig. 38, a,d**), but instead of trapping myosin in a specific biochemical state experiments were performed during the transient phase initiated by myosin-ATP mixing. We have used transient time-resolved FRET [$(TR)^2$FRET) to obtain structural resolution and transient biochemical resolution simultaneously in a single experiment.

4.3 Results

Relay helix structural transition during myosin-ATP interaction resolved in real time. The rate of the relay helix conformational change during the myosin-ATP interaction (recovery stroke) was determined in a two dimensional $(TR)^2$FRET experiment. 5 mM ATP and 10-30 μM donor-acceptor labeled myosin (syringe concentrations) were mixed in the stopped-flow fluorimeter (77) and a complete donor fluorescence signal was acquired after each laser pulse (10kHz) immediately after myosin-ATP mixing. The result is a complete two-dimensional data set, resolved in both the nanosecond fluorescence signal time scale and the millisecond biochemical reaction time scale (**Fig. 40a**). At each time point in the millisecond-resolved transient, TR-FRET revealed the distance distribution between probes, with essentially the same high resolution and precision as in the equilibrium experiments of **Fig. 32**. Both the integral intensity and apparent lifetime of donor fluorescence decreased after myosin-ATP mixing, reflecting an increase of donor-acceptor energy transfer and a decrease of the donor-acceptor mean distance (**Fig. 39**).

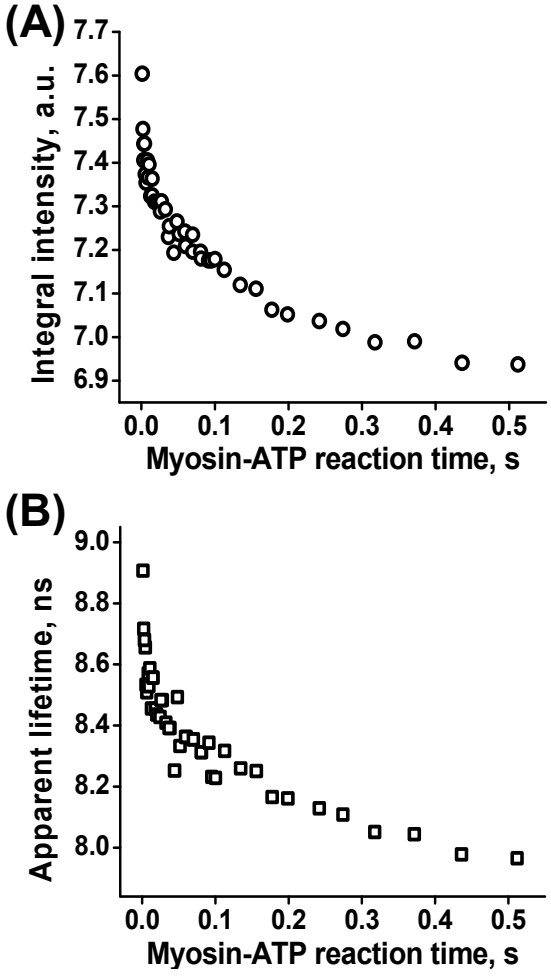

Fig. 39. Changes in donor signal intensity and life-time during $(TR)^2$FRET experiment
(A) Integral intensity of $(TR)^2$FRET signal at each reaction time point. The observed 10% decrease of fluorescence intensity indicates an increase in FRET efficiency due to decreased interprobe distance. **(B)** Apparent lifetime of $(TR)^2$FRET signal at each reaction time point. The observed 10% decrease of the apparent lifetime indicates an increase in FRET efficiency due to decreased interprobe distance.

As in TR-FRET, the donor fluorescence signals were fitted by a sum of exponentials according **Eq. 26-Eq. 27**, assuming two structural states, M* and M**, each with a distinct Gaussian distance distribution. A typical result is shown in **Fig. 40**: the fraction

$$M + T \underset{k_{-1}}{\overset{k_1}{\Leftrightarrow}} M*T \underset{k_{-2}}{\overset{k_2}{\Leftrightarrow}} M**T \underset{k_{-3}}{\overset{k_3}{\Leftrightarrow}} M**D.P$$ Scheme III

X** of myosin with bent relay helix M** increases after myosin-ATP mixing. Kinetic traces for M** population were fitted to the solution of the system of differential equations (**Eq. 35**), according to the **Scheme III**, assuming the transition from the post-recovery stroke M**.D.P state is the reaction limiting step (78):

Table 10 Rate constants (as defined in Scheme III) of ATP binding and relay helix structural transitions.

Rate constant	T=4C	T=10C	T=20C
k_1, ($\mu M^{-1}s^{-1}$)	1.3±0.5	2.4± 1.6	2.4±1.7
k_{-1}, (s^{-1})	0.4±0.4	0.5± 0.4	0.4±0.4
k_2, (s^{-1})	36.8±1.3	64± 7	152±28
k_{-2}, (s^{-1})	260±11	347± 40	559±111
k_3, (s^{-1})	7.1± 0.5	7.4± 0.6	9.9±0.7
k_{-3}, (s^{-1})	5.0± 0.6	6.4± 0.5	9.7±0.5

Uncertainties are standard deviations from 40-50 fits, started from different initial values, and having the same χ^2 at the end of the fit

Kinetic constants obtained from the fits are shown in **Table 10**.The first step in **Scheme**

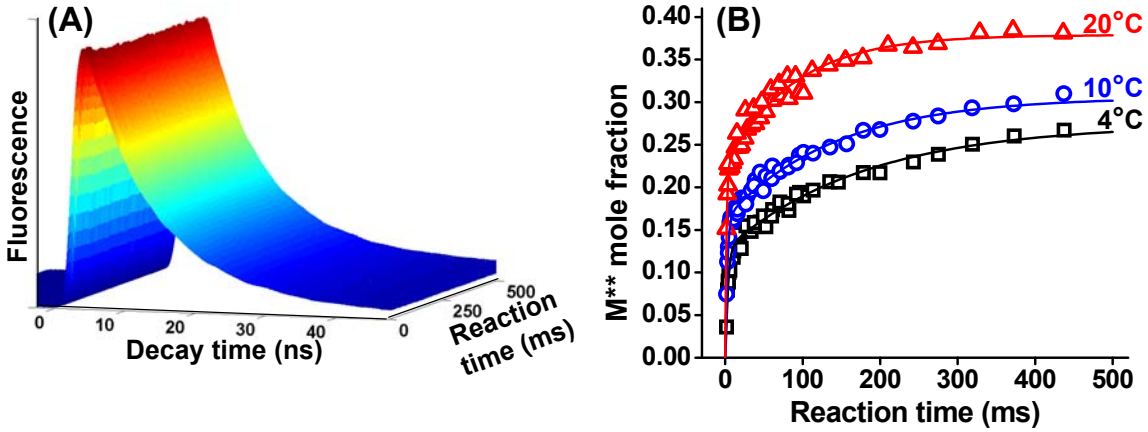

Fig. 40. Two-dimentional $(TR)^2$FRET experiment
(A) Typical data set at 20°C, with 0.125 ns resolution in the fluorescence decay time and 0.1 ms resolution in the biochemical reaction time. **(B)** Analysis of data sets at three temperatures, showing kinetics of M** formation after myosin-ATP mixing. At each temperature, curves were fit globally, assuming a linear combination of two structural states, each characterized by a Gaussian distribution of interprobe distances. Curves show the best-fit simulation of the M* → M** transition, based on **Scheme III**

III, ATP binding to myosin, is very fast, practically irreversible and temperature-

independent (k_1 and k_{-1}, **Table 10**). The recovery stroke (M*T → M**T, characterized by k_2 and k_{-2}) and the hydrolysis step (M**T → M**D.P, characterized by k_3 and k_{-3}) are temperature-dependent steps. The recovery stroke is about an order of magnitude faster than ATP hydrolysis. Using rate constants from **Table 10** we were able to determine thermodynamic properties of the system (e.g. activation energy as well as change in entropy and enthalpy during the recovery stroke and ATP hydrolysis).

Thermodynamics of the recovery stroke and ATP hydrolysis. Activation energies E_a, and changes in entropy and enthalpy during the recovery stroke and ATP hydrolysis were determined from the temperature dependence of the kinetic constants k_+ and k_- **(Table 10)**, according to the Arrhenius and van't Hoff equations:

$$k=A\cdot\exp[-E_a/(RT)] \qquad \textbf{Eq. 33}$$

$$\ln K_{eq}= \Delta S/R - \Delta H/(RT),\ K_{eq} = k_+/k_-, \qquad \textbf{Eq. 34}$$

where k_+ and k_- are rate constants, K_{eq} is an equilibrium constant, R is the universal gas constant, T is the temperature, and ΔS and ΔH are changes in the entropy and enthalpy. Arrhenius and van't Hoff's plots for the recovery stroke and ATP hydrolysis are shown in **(Fig. 41)**.

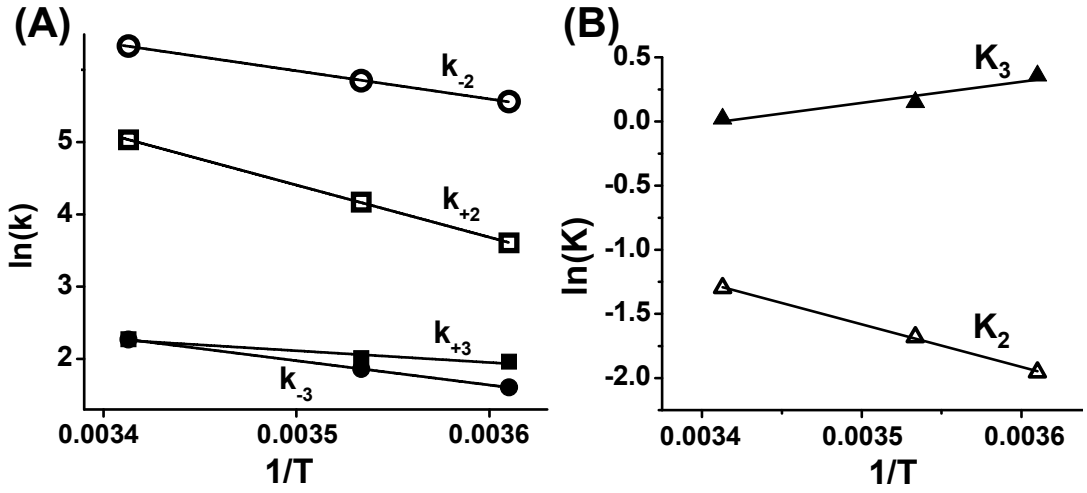

Fig. 41. Arrhenius (a) and Van't Hoff plots (b) for the recovery stroke, and the hydrolysis step,

$$M^{*}.T \underset{k_{-2}}{\overset{k_2}{\Leftrightarrow}} M^{**}.T \qquad\qquad M^{**}.T \underset{k_{-3}}{\overset{k_3}{\Leftrightarrow}} M^{**}.D.P.$$

Rate constants k (**Table 10**) were determined from the fits of $(TR)^2$FRET data, and equilibrium constants K were determined from rate constants. Lines show best fits to **Eq. 33** (E_2 = 60 kJ/mole, E_{-2} = 32.4 kJ/mole, E_3 = 13.5 kJ/mole and E_{-3} = 28 kJ/mole) and **Eq. 34** (ΔH_2 = 27.6 kJ/mol, ΔS_2 = 0.084 kJ/(mol·K), ΔH_3 = -13.7 kJ/mol and ΔS_3 = -0.047 kJ/(mol·K)).

We determined E_2 = 60 kJ/mol and E_{-2} = 32.4 kJ/mol for the recovery stroke and E_3 = 13.5 kJ/mol and E_{-3} = 28 kJ/mol for ATP hydrolysis. In the recovery stroke ΔH = 27.6 kJ/mol and ΔS = 0.084 kJ/(mol·K), which is in good agreement with the values determined previously by EPR from the temperature dependence of two myosin populations in the M.ADP.BeF_x complex (Chapter 2). For the ATP hydrolysis step, ΔH = -13.7 kJ/mol and ΔS = -0.047 kJ/(mol·K).

4.4 Discussion

In this study we have used a newly developed technique, transient time-resolved FRET, to determine simultaneously the structure and the kinetics of the relay helix during the dynamic myosin-nucleotide interaction. The goal of the study was to investigate whether myosin force-generating region alternates between the two structural states during the recovery stroke or can adopts an intermediate "transient conformation". In addition, we were interested in determining the rates of structural transitions and relating them to the known rates of other events of the myosin cycle, thus elucidating the interdomain coupling mechanisms.

Structure of the relay helix during the recovery stroke. Global fitting of several hundred fluorescent decays recorded immediately after myosin-ATP mixing revealed that only two conformation of the relay helix are present during the recovery stroke and ATP hydrolysis. These two conformations were identical to the ones identified previously in the steady-state experiments with nucleotide analogs (Chapter 3). We have shown that ATP hydrolysis is a relatively slow process, depleting the M**ATP state by formation of the M**ADP.P_i state. Although ATP hydrolysis did not result in appearance of a new structural state, thermodynamic analysis showed that hydrolysis lowered the activation energy of the M*→M** transition by approximately factor of 5, which resulted in a higher occupancy of the M** state (**Fig. 42**).

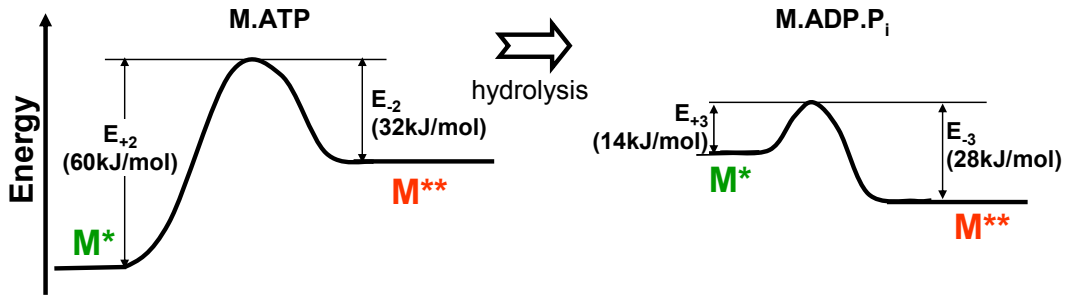

Fig. 42. Schematic representation of the myosin-nucleotide complex energy profile in the pre- and post-hydrolysis states.
ATP hydrolysis significantly lowers the activation energy of the M*→M** transition.

Relay helix structural transitions are rigidly coupled to the conformational changes in the ATP-binding pocket. Our experiments have shown that the relay helix undergoes a structural transition immediately after ATP binding, and rate of the transition is close to that of nucleotide pocket closure, as estimated previously from Trp fluorescence transients (79), indicating a direct correlation between the structure of the pocket and the structure of the relay helix. These results demonstrate that the relay helix responds to the changes in the nucleotide binding pocket and identify the relay helix as a major coupling element of the myosin structure that propagates changes from the active site to the myosin converter domain.

4.5 Conclusions

In conclusion, in this work we introduce transient time-resolved FRET [$(TR)^2$FRET] – a new tool in structural molecular biology that resolves structural transitions on the millisecond time scale. We have applied this approach to determine the nucleotide-induced dynamics of the myosin relay helix, an important structural element in the force-generating region, connecting the nucleotide binding site and the lever arm. By combining $(TR)^2$FRET with conventional biochemical techniques (protein mutagenesis, site-directed labeling), we (a) detected structural changes in the myosin relay helix in response to nucleotide binding, (b) resolved two structural states of the relay helix in a single biochemical state of myosin, and (c) observed kinetics of structural changes in the relay helix in real time during the myosin–ATP interaction. We have determined that the relay helix changes its conformation immediately upon ATP binding to myosin. ATP hydrolysis is an order of magnitude slower process required to remove the nucleotide from the active site. Our experiments demonstrate the power of the $(TR)^2$FRET technique, showing the evolution of the relay helix in real time, and revealing the dynamic mechanism that couples myosin's active site and force-generating region.

4.6 Material and Methods

Most experimental procedures, including protein preparation, labeling and functional assays, were identical to the ones described in the Chapter 3.

$(TR)^2$FRET. Transient time-resolved FRET experiments were performed with a stopped flow apparatus (SFM-20, Bio-Logic, Claix, France) that was attached to the TR-FRET fluorimeter to measure transient kinetics of the myosin-ATP reaction. Myosin and ATP solutions were loaded into 10mL syringes, the total flow rate through the mixer was 8mL/s, giving a dead time of 1.4 ms (77). Donor fluorescence signals were acquired after every laser pulse (10kHz); data of 5 to 20 stopped flow shots were averaged to increase the signal-to-noise ratio. Fluorescent waveworms were analyzed in the same way as TR-FRET data. All donor fluorescence signals were fitted globally to **Eq. 26 - Eq. 30**. Amplitudes A_i, lifetimes τ_i, distances R^* and R^{**} and the fraction of donor-only labeled myosin X_D were linked and varied simultaneously for all signals during the global fit. X** (the mole fraction of the M** structural state) was varied independently for every signal. Usually several datasets from different protein preparations were fitted simultaneously, and corresponding fractions (X**) were linked. The fraction X_D of donor-only labeled myosin mutant was varied between different protein preparations.

Analysis of the recovery stroke kinetic traces. To determine kinetic constants of myosin-ATP reaction, time dependent trace of M** fraction (X**) was fitted to the solution of the system of differential equations for M** ($M^{**} = M_T^{**} + M_{DP}^{**}$) (according to **Eq. 35**):

$$\begin{aligned}
\frac{dM}{dt} &= -k_1 MT + k_{-1} M^* \\
\frac{dM^*}{dt} &= k_1 MT - k_{-1} M^* - k_2 M^* + k_{-2} M_T^{**} \\
\frac{dM_T^{**}}{dt} &= k_2 M^* - k_{-2} M_T^{**} - k_3 M_T^{**} + k_{-3} M_D^{**} \\
\frac{dM_D^{**}}{dt} &= k_3 M_T^{**} - k_{-3} M_D^{**}
\end{aligned} \qquad \textbf{Eq. 35}$$

where M is the concentration of free myosin, M* and M** are concentrations of myosin in M* and M** structural, T is the concentration of ATP, k_i are kinetic constants, M_T** and M_{DP}** are the same structural states of myosin M**, but with ATP or ADP.P bound.

Chapter 5. The role of the relay loop in the regulation of myosin force-generation.

5.1 Overview

As discussed in the previous chapters, we have shown that the relay helix is a key element of the myosin structure responsible for communication between the active site and the force-generating region. As a next step, we have used DEER (dipolar electron-electron resonance), FRET (fluorescence resonance energy transfer) and $(TR)^2$FRET (transient time-resolved FRET) to investigate the regulatory mechanisms that affect the relay helix structural dynamics. Previous studies have shown that mutation of the phenylalanine 506 located in the myosin relay loop results in a complete loss of myosin motor function without significant effect on enzymatic activity (12). The goal of our experiments was to elucidate the effect of this mutation on structure of the relay helix and to determine the role of the relay loop in myosin force generation. In contrast to WT, where two distinct (straight and bent) conformations of the relay helix were resolved, the relay helix in the F506A mutant was significantly less ordered. The increased disorder washed out the difference between the structural states, resulting in a considerably smaller effect of nucleotide analog binding on the average interprobe distance. Transient experiments revealed that upon mixing with ATP the relay helix undergoes a structural transition, but the kinetics of the ATPase cycle is distorted. We conclude that relay loop – relay helix interactions are crucial for stabilizing the bent (post-recovery) state of the helix, and disruption of these interactions leads to the loss of the myosin's motor functions. Our experiments provide a structural explanation of the observed functional effects of the F506A mutation and identify the relay loop as a key player in myosin power stroke regulation.

5.2 Introduction

Comparison of the myosin crystal structures in the pre- and post-recovery states shows that converter domain (bearing the lever arm and controlling its position) rotates by approximately 60° between these states. From the catalytic domain side the position of the converter is controlled by the covalently bound SH1-SH2 helices and (though hydrophobic interactions) by the relay helix (**Fig. 43**). Based on molecular dynamics simulations a mechanistic model of the recovery stroke has been proposed (8). According to this model, closure of the switch II occuring after ATP binding, pulls down the N-terminal end of the relay helix and, because of the fulcrum point in the middle, it lifts the C-terminal end (adjacent to the converter domain) in a seesaw-like motion. This leads to a 25° rotation of the converter, which is followed by a second phase during which piston-like motion of the SH1 helix enables additional rotation of the converter by ~40°, completing the recovery stroke. Experiments with single Trp mutants (80) revealed that mutations within the phenylalanine cluster that forms the fulcrum (Phe 481, Phe 482 and Phe 652) result in abnormal behavior of the relay helix, demonstrating the importance of the relay helix structural integrity. At the same time direct evidence for the seesaw mechanism are lacking, and it remains unclear whether integrity of the fulcrum region and proper function of the switch II are sufficient for inducing a recovery stroke.

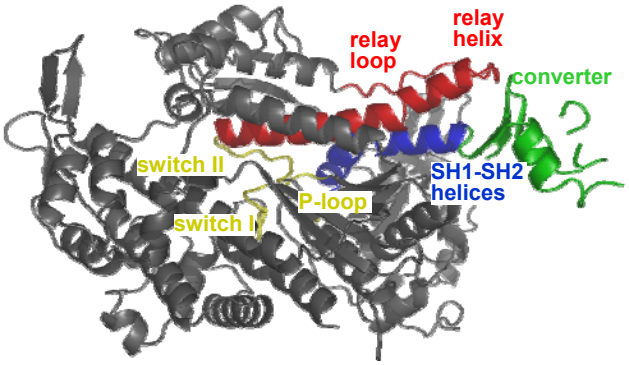

Fig. 43. Active site and force-generating-domain of the myosin catalytic domain.
Position of the converter (green) is controlled by the SH1-SH2 helices (blue) and the relay helix (red) which connects it to the switch II of the ATP-binding pocket (yellow). Relay loop (red) originates at the C-terminal end of the relay helix and connects it back to the 50k domain.

Of particular interest is the functional role of the myosin relay loop that connects the C-terminal end of the relay helix with the myosin 50k domain (**Fig. 43**). Manstein and colleagues have shown that replacing the Phe506 with Ala or Gly results in a non-functional myosin that can not support the actin sliding in in-vitro motility assays and do not support cell growth and multicellular development (12), but structural basis for this

dramatic change in phenotype is unknown. Close proximity of the relay helix and relay loop suggests that perturbation in the loop structure can also affect the structure of the helix. In addition, crystal structures show that Phe506 is located near the Phe487 of the relay helix, and potential hydrophobic interaction between the two phenylalanines can strengthen the loop-helix connection. In this case substitution of Phe506 with less hydrophobic amino acids can disrupt the interaction and change the relay helix structural dynamics.

In the current work we employ our spectroscopic approach to investigate the structural effect of F506A mutation on myosin relay helix structure and dynamics. Two double Cys mutants (515:498 and 639:498) were labeled with MSL/MSL or IAEDANS/Dabcyl probes and distance between them was measured using DEER and TR-FRET. The structural changes in the relay helix were determined in the steady-state (after mixing with saturating nucleotide concentrations) and during kinetic transient after rapid mixing with ATP. Our experiments show that the mutation destabilizes the C-terminal part of the relay helix and distort the equilibrium between bent and straight conformations. We conclude that the recovery stroke mechanism is more complex than implied by a see-saw model, and relay helix – relay loop interactions are crucial for stabilizing the bent state of the helix and proper myosin regulation.

5.3 Results.

Effect of the F506A mutation on the relay helix structure detected by DEER. As discussed in chapter 3, DEER experiments have shown that binding of ATP and ADP.P_i analogs (ADP.BeF_x and ADP.AlF_4 respectively) to the 515.498 and 639.498 double-Cys myosin constructs (referred later on as wild type or WT) increased the rate of echo decay, indicating a decrease of the average interprobe distance (**Fig. 44**, grey). In addition, in M.ADP.BeF_x and M.ADP.AlF_4 biochemical states echo oscillations were more pronounced, indicating ordering of the system (**Fig. 44**, grey). In contrast, binding of the same analogs to the F506A myosin resulted in significantly smaller changes in DEER signal (**Fig. 44**, orange). Although the decay rate increased in the same order: M (slowest) → M.ADP → M.ADP.BeF_x → M.ADP.AlF_4 (fastest), the effect was much less pronounced. Prolonged echo oscillation were not observed in any of the complexes.

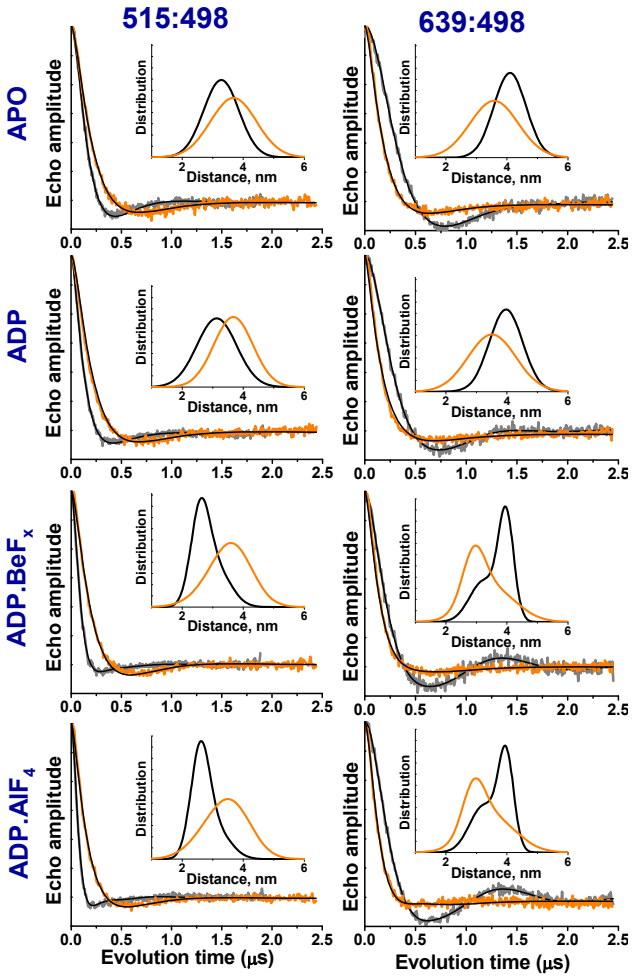

Fig. 44. DEER signals for WT (grey) and F506A (orange) myosin and corresponding distance distributions. F506A shows smaller difference in signals between different biochemical states. Shift of the mean distance suggests an abnormal conformation of the relay helix, and less pronounced echo amplitude oscillations indicate increased width of distance distribution (increased flexibility).

Analogously to WT, experimental data were fitted assuming that a single structural state (corresponding to a one-Gaussian distance distribution) is present in the apo and ADP-bound states and two structural states (M* and M**) are present in myosin-nucleotide analog complexes. DEER signals in the M.ADP, M.ADP.BeF_x and M.ADP.AlF_4 states were fitted globally using the same set of parameters: (R*, FWHM*)

and (R**, FWHM**). Analysis of both myosin constructs (515:498 and 639:498) showed a change in the mean interprobe distances in F506A compared to the WT. In the mutant the C-terminal end of the relay helix moved away from the residue 515 and closer to the residue 639 in both pre- and post-recovery structural states, indicating that the relay helix adopted a slightly distorted conformation. As suggested by the absence of visible echo oscillations in F506A DEER signals, both F506A constructs showed a significant increase in the width of distance distribution that to a large extent washed out the difference between the two structural states (M* and M**) (**Fig. 44**, orange).

Effect of the F506A mutation on the relay helix structure detected by TR-FRET. Similarly to DEER experiments, fluorescent waveforms were obtained for myosin in the apo state, with bound ADP, ATP and ADP.P_i analogs (ADP.BeF_x and ADP.AlF_4 respectively). In the 515:498 construct, F506A myosin showed a decreased rate of the fluorescence decay (**Fig. 45**) consistent with the increased interpobe distance detected by DEER. In the 639:498 construct the difference was more complex: the decay rate appeared to be faster at the beginning and slower at the end of the decay – behavior indicating an increase in the width of the distance distribution. As in DEER experiments, fluorescence decays corresponding to F506A myosin were not significantly affected by nucleotide binding.

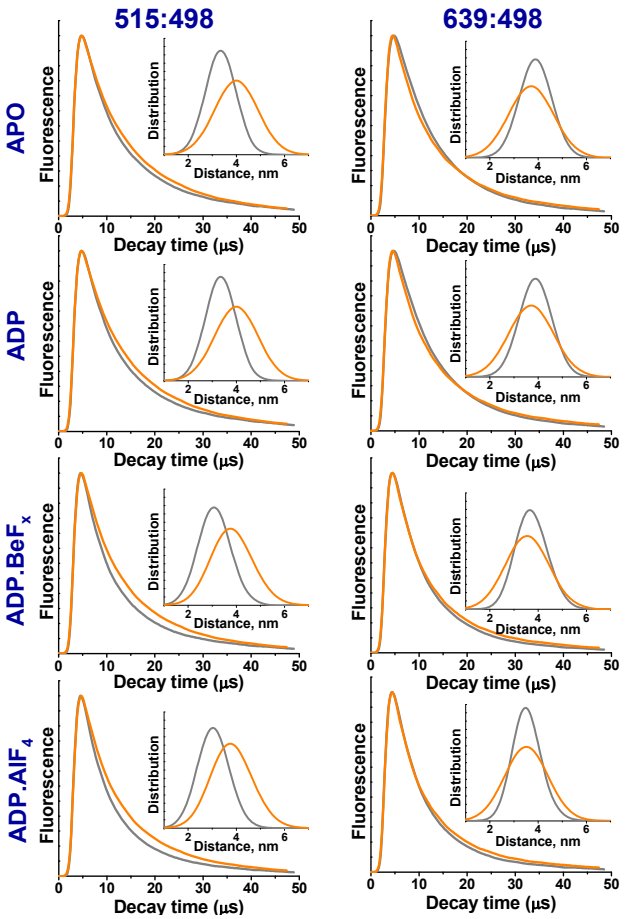

Fig. 45. FRET signals, normalized to maximum amplitude, for WT (grey) and F506A (orange) myosin and corresponding distance distributions.
F506A shows smaller (compared to WT) difference in signals between different biochemical states. F506A distance distributions are slightly shifted and have large width, indicating an increased flexibility in the relay helix.

Donor fluorescence signals for all four biochemical states were fitted globally (assuming the presence of the same two structural states: M* and M**) according to **Eq. 25 - Eq. 30**. Analogously to WT one-Gaussian distribution was used to simulate and fit apo and M.ADP biochemical states, and two-Gaussian distribution were used for M.ADP.BeF_x and M.ADP.AlF_4 states. Extracted distance distributions are shown in **Fig. 45**.

Structural changes in the relay helix resolved in time. High sensitivity of TR-FRET allowed us to perform transient time-resolved experiment [(TR^2)FRET]. In such an experiment myosin is mixed with the nucleotide and a number of fluorescent waveforms is acquired. Each waveform carries information about myosin structure and series of waveforms, recorded consequently, yields information about evolution of the structure in time (**Fig. 46, A**). As in previous experiments with WT myosin, F506A was rapidly mixed with ATP in a stopped-flow apparatus, and the obtained fluorescent signals were analyzed globally assuming that the two structural states of myosin (M* and M**, with straight and bent relay helix respectively) are present throughout the reaction. Each structural states is characterized by a distinct Gaussian interprobe distance distribution that does not change during the transient. The only variable parameters between different waveforms was the M** mole fraction.

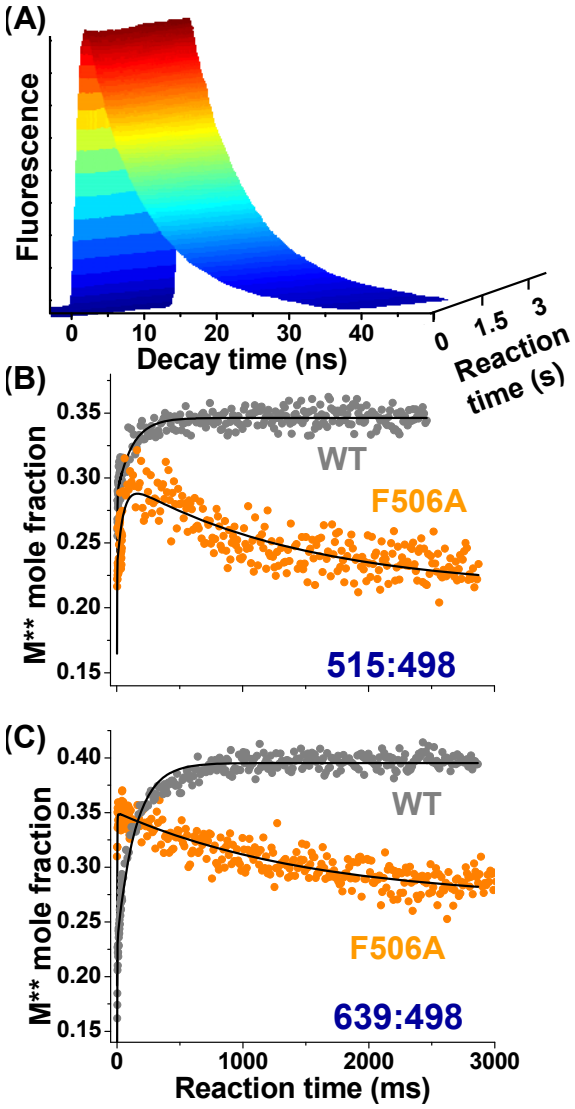

Fig. 46. Difference in the kinetic transient between WT and F506A
(**A**) typical two-dimensional dataset obtained from the transient TR-FRET experiment. (**B**) and (**C**) Time dependence of the M** mole fraction (fraction of myosin with bent relay helix) after rapid mixing with ATP. 10μM myosin was mixed with 5mM of ATP, grey circles - WT myosin, orange circles – F506A myosin, black lines best fit kinetic simulations (**Scheme III, Scheme IV**). Both construct show plateau at the end of the transient for the WT myosin and decrease of the M** conformation for F506A.

As discussed in chapter 4, after mixing of ATP with WT myosin, M** mole fraction (corresponding to the bent relay helix) increased. Three phases could be distinguished: fast initial rise (with rate constants on the order of 100s^{-1}), slower increase (with rates on the order of 10s^{-1}) and the plateau (**Fig. 46**, grey). Kinetic simulations according to the (**Scheme IV**) yielded rates of

individual steps, summarized in **Table 10**. Only the first three steps of the **Scheme IV** were needed to successfully fit the data, addition of steps 4 through 6 did not improve quality of the fit and yielded very slow k_{+4} rates ($<0.1s^{-1}$) consistent with the previous observations that M**D.P to M*D.P transition (**Scheme IV**), and accompanying phosphate release, is a rate limiting step of the cycle (78). Experiment performed on F506A myosin revealed several key differences: the second phase of the kinetic transient had smaller amplitude indicating a decrease in the forward rate for the step 3 of the reaction (**Scheme IV**), and the most dramatic change was the decrease of the M** mole fraction during the third phase (**Fig. 46**, orange). Such a decrease is a direct indication that in contrast to WT myosin, the F506A mutant does not accumulate in the M**.D.P state, but undergoes M**→M* structural transition (step 4 in the **Scheme IV**). Kinetic transients were simulated according to **Scheme IV**, $k_{\pm1}$, $k_{\pm2}$, $k_{\pm3}$ and $k_{\pm4}$ were varied, and rate constants $k_{\pm5}$ and $k_{\pm6}$ were fixed to values reported in the literature (12, 78) to decrease an uncertainty of the simulations. Kinetic constants obtained from the fit are summarized in **Table 11**.

$$M + T \underset{k_{-1}}{\overset{k_1}{\Leftrightarrow}} M*T \underset{k_{-2}}{\overset{k_2}{\Leftrightarrow}} M**T \underset{k_{-3}}{\overset{k_3}{\Leftrightarrow}} M**D.P \underset{k_{-4}}{\overset{k_4}{\Leftrightarrow}} M*D.P \underset{k_{-5}}{\overset{k_5}{\Leftrightarrow}} M*D \underset{k_{-6}}{\overset{k_6}{\Leftrightarrow}} M + D \qquad \text{Scheme IV}$$

Table 11. Rate constants of myosin ATPase cycle (according to the Scheme IV)

Rate constant	515:498		639:498	
	WT	F506A	WT	F506A
k_1, ($\mu M^{-1}s^{-1}$)	0.9±0.7	1.8±1.2	2.4±1.7	1.5±1.2
k_{-1}, (s^{-1})	2.0±1.5	1.1±1.4	0.4±0.4	0.12±0.3
k_2, (s^{-1})	92±44	176±9	152±28	345±106
k_{-2}, (s^{-1})	348±75	717±160	559±111	683±221
k_3, (s^{-1})	6.0±1.6	4.2±1.1	9.9±0.7	2.4±2.1
k_{-3}, (s^{-1})	3.5±3.9	19.5±5.5	9.7±0.5	42±11
k_4, (s^{-1})	<0.1	23±14	<0.1	16±11
k_{-4}, (s^{-1})	-	22±15	-	16±7

5.4 Discussion

The relay helix serves a communication pathway between the myosin active site and its force-generating region, as discussed in chapters 3 and 4, but the mechanism that regulates the structural transition of the helix itself is not known. The goal of the current study was to investigate the role of the relay loop in regulation of myosin force generation. The relay loop connects the C-terminal end of the relay helix with the lower 50k domain (**Fig. 43**). A previous mutagenesis study (12) revealed that replacement of Phe506 of the relay loop with Ala or Gly lead to uncoupling of myosin enzymatic and motor functions. Apart from the covalent bonds between the relay helix and relay loop, these elements may form additional contacts. In particular, Phe506, is located in a close proximity to Phe487 of the relay helix, and may affect the structure of the helix through hydrophobic interactions (**Fig. 47**). We have used our spectroscopic approach to: (a) directly compare the structure of the relay helix in the WT and F506A myosin in different biochemical states, and (b) compare the rates of structural transitions. Combination of time-resolved EPR (DEER) and time-resolved FRET was used to achieve the necessary spatial and temporal resolution. As before, two pairs of labeling sites and two pairs of probes were used to obtain a three-dimensional picture of the structural changes and eliminate the concern that probes have caused a significant perturbation of the myosin structure.

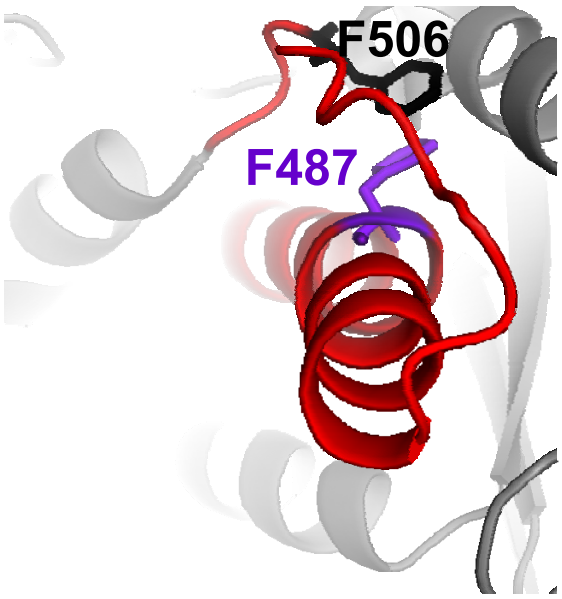

Fig. 47. Fragment of the myosin force-generating region.
In the post-recovery state hydrophobic interactions between Phe506 (black) on the relay loop (red) and Phe487 (purple) on the relay helix (red) may stabilize the bent state of the helix.

Relay helix is more disordered in the F506A myosin. We found that in F506A myosin, analogously to WT, relay helix can adopt two conformations, straight and bent, corresponding to M* and M** structural states of myosin. But in the mutant structure of

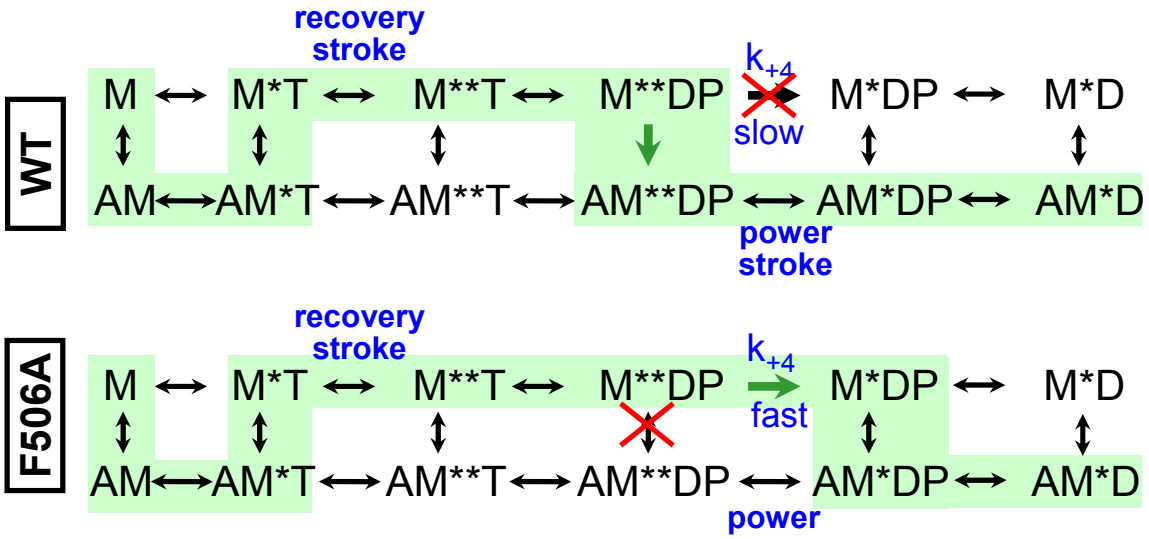

Fig. 48. Acto-myosin ATPase cycle.
M – myosin, A – actin, T - ATP, D -ADP, P - inorganic phosphate. Green shade indicates the most probably pathway. Increased rate of M**DP→M*DP transition observed in F506A myosin allows myosin to change its conformation in the absence of actin, thus "power stroke" does not lead to actin movement.

the helix was slightly distorted, as evident from changes in the mean distance (**Fig. 44** and **Fig. 45**). More importantly, the width of the distance distribution was significantly greater in F506A indicating an increase in the relay helix flexibility. This observation was particularly clear due to the high sensitivity of DEER to system disorder. WT myosin in M.ATP and M.ADP.P_i biochemical states (mimicked by ADP.BeF_x and M.ADP.AlF_4) displays oscillation of the spin echo intensity (that are particularly apparent in the 639:498 construct) indicating an ordered system, while no oscillations are observed in F506A. This result supports the hypothesis that Phe506-Phe487 interactions are important for trapping the bent conformation of the relay helix. F506A mutation may destroy this interaction, destabilizing the force-generating region and allowing the relay helix to fluctuate to a larger extent around the equilibrium states.

Increased rate of the reverse recovery stroke in F506A results in a futile ATPase cycle. Rapid mixing experiments revealed that initial steps of the myosin-ATP interactions were not significantly affected by mutation. As in WT, F506A myosin was able to bind ATP and transitioned into the M** state. However, the change in the M** mole fraction was not monotonic, and instead of a plateau a decrease in the M** population was observed at the final phase of the transient experiment. Kinetic

simulations showed that this decrease is due to a dramatic increase (by more than a factor of 100) in the k_{+4} rate constant (forward rate of the "power stroke") **Table 11**.

In agreement with this observation, the equilibrium for the hydrolysis step $K_3=k_{+3}/k_{-3}$ in **Scheme IV** was shifted to the left (toward the ATP-bound state). This shift is expected, considering that the bent relay helix (M** structural state) corresponds to a closed (catalytically active) state of the ATP-binding pocket. Premature straightening of the helix (M**→M* transition) may thus hinder the hydrolysis efficiency. Increased rate of the power stroke is also in a good agreement with the observed increase in flexibility detected in steady-state experiments. Significant overlap in conformational space, sampled in M* and M** structural states, suggests smaller activation energy and faster rate for the M**→ M* transition.

For myosin to generate force, the power stroke must occur after acto-myosin complex formation, otherwise the structural change in myosin will not result in actin movement (**Fig. 1**). In WT myosin the power stroke is a rate-limiting and very slow step that normally occurs only after actin binding (**Fig. 48**, top) (78). However, in the F506A this transition can easily occur in the absence of actin. Consequently, the normal pathway of the myosin ATPase cycle is disrupted (**Fig. 48**, bottom). Instead of binding actin and executing a productive power stroke, myosin can undergo M**→M* structural transition in the absence of actin. Such a cycle does not result in movement of actin filaments and myosin does not perform work, leading to the observed loss-of-motor-function phenotype.

Role of the relay loop in regulation of force generation.

Phe506 to Ala506 substitution results in a permanent weakening of the loop-helix interaction. Weakened interaction, in turn, leads to a premature straightening of the relay helix and a premature swing of the lever arm. This rises a question: what is the role of the relay loop in the wild type myosin? Relay loop connects the relay helix with the lower 50k domain, which rotates during actin binding and actin cleft closure (5, 81). Movement of the lower 50k domain is likely to affect the conformation of the relay loop possibly disrupting its connection with the relay helix and can trigger a power stroke. From this

perspective, relay loop appears to play an important regulatory role: in the absence of actin it stabilizes the M** conformation preventing M**→M* transition, and it triggers this transition upon actin binding.

5.5 Conclusions.

We have used a combination of spectroscopic techniques to determine the effect of F506A functional mutation on the structure of the myosin relay helix. We determined that the mutation increases flexibility of the C-terminal end of the rely helix, allowing it to undergo large fluctuation around the equilibrium states. Transient experiments revealed that mutation dramatically accelerated the rate of the power stroke, enabling myosin to undergo M**→M* structural transition in the absence of actin and resulting in a futile ATPase cycle. We conclude that (a) relay loop - relay helix interactions are crucial for stabilizing proper conformation of the relay helix and (b) relay loop plays an important role in force generation regulation.

Future directions

The main goal of this work was to investigate the coupling mechanisms between the myosin's active site and its force-generating region. We have shown that the relay helix is coupled to the nucleotide-binding pocket and responds to changes in its structure. It is likely to propagate these changes to the converter domain and further to the myosin lever arm, through the hydrophobic interactions. We have also shown that the structure of the relay helix is controlled by the relay loop, and uncoupling of these two elements results in a loss of structural organization within the force-generating region, which is the most probable cause for the loss of motor functions observed in F506A functional mutant.

Looking from a broader prospective, our experiments have unambiguously shown that there is no one-to-one correspondence between myosin structural state and its biochemical state (as defined by the bound nucleotide). EPR studies of myosin, labeled at the SH1 site, showed that the two structural states were populated when ATP and ADP.P_i analogs were bound. Direct distance measurements performed with DEER and time-resolved FRET led to the same conclusion: two conformation of the relay helix were observed in a single biochemical state. We have also found that the structural changes in myosin are not limited to changes in the mean, or most probable, conformation. Protein flexibility, or amount of disorder in the system, also changes during structural transitions. These results emphasize the dynamic nature of proteins. In addition to large-scale conformational transitions, proteins undergo transitions on a smaller scale, which result in fluctuations around the equilibrium. If the energy barriers between different structural states are small enough, the amplitude of these "fluctuations" may increase and multiple structural states become populated. Consequently structural transitions in myosin, and most likely many other enzymes, are determined by the energy landscape that defines protein structural states and rates of the transition. Precise tuning of the energy landscape is crucial for enzyme optimal performance, mutations in structure alter the energy landscape and may perturb the normal reaction pathway leading to modified functional properties or even to a loss of enzymatic activity.

The natural extension of this work is to test the interaction between the relay helix and the converter, as wells as between the converter and the SH1 helix. Mutagenesis

studies have identified a number of residues that appear to be crucial for proper myosin function. These mutations (e.g. I499A and F692A) are likely to disrupt the interaction between elements of the force-generating region and perturb the subdomain coupling. Elucidating the exact structural effect of these mutations on the structure of the relay helix (and, potentially, other elements) can provide valuable information about the mechanism of myosin function.

Another intriguing question is the mechanism of power stroke activation by actin. In the current work we have shown that the F506A mutation mimics some of the effects of actin binding (for instance, it dramatically accelerates the rate of the power stroke). DEER and TR-FRET experiments, analogous to discussed in this dissertation, but performed on the acto-myosin complex will show the effect of actin binding on the structure of the relay helix and the structure of the force-generating domain in general. Of particular interest are transient experiments. Preincubation of myosin with ATP followed by a rapid mixing with actin should provide insights into the structural dynamics of the relay helix during the power stroke and force generation. Comparing structural evolution of the wild type myosin, determined in $(TR)^2$FRET experiments, with time-resolved structural changes in various myosin mutants can be especially fruitful. Such experiments are likely to provide valuable insights into the mechanism of actin activation.

The approach developed in this work, combining a series of spectroscopic techniques, each of which provides unique information about the system, is versatile and can be readily applied to other myosin domains (e.g. actin-binding cleft, nucleotide-binding pocket). Systematic analysis of the data should reveal the interaction mechanisms within myosin and eventually lead to a detailed understanding of myosin function on the submolecular level.

Bibliography

1. Thomas, D. D., Kast, D. & Korman, V. L. (2009). **Site-directed spectroscopic probes of actomyosin structural dynamics**, *Annu Rev Biophys* **38,** 347-369.
2. Rayment, I., Rypniewski, W. R., Schmidt-Base, K., Smith, R., Tomchick, D. R., Benning, M. M., Winkelmann, D. A., Wesenberg, G. & Holden, H. M. (1993). **Three-dimensional structure of myosin subfragment-1: a molecular motor**, *Science* **261,** 50-58.
3. Prochniewicz, E., Walseth, T. F. & Thomas, D. D. (2004). **Structural dynamics of actin during active interaction with myosin: different effects of weakly and strongly bound myosin heads**, *Biochemistry* **43,** 10642-10652.
4. Geeves, M. A. & Holmes, K. C. (1999). **Structural mechanism of muscle contraction**, *Annu Rev Biochem* **68,** 687-728.
5. Klein, J. C., Burr, A. R., Svensson, B., Kennedy, D. J., Allingham, J., Titus, M. A., Rayment, I. & Thomas, D. D. (2008). **Actin-binding cleft closure in myosin II probed by site-directed spin labeling and pulsed EPR**, *Proc Natl Acad Sci U S A* **105,** 12867-12872.
6. Sasaki, N., Shimada, T. & Sutoh, K. (1998). **Mutational analysis of the switch II loop of Dictyostelium myosin II**, *J Biol Chem* **273,** 20334-20340.
7. Smith, C. A. & Rayment, I. (1996). **X-ray structure of the magnesium(II).ADP.vanadate complex of the Dictyostelium discoideum myosin motor domain to 1.9 A resolution**, *Biochemistry* **35,** 5404-5417.
8. Koppole, S., Smith, J. C. & Fischer, S. (2007). **The structural coupling between ATPase activation and recovery stroke in the myosin II motor**, *Structure* **15,** 825-837.
9. Fischer, S., Windshugel, B., Horak, D., Holmes, K. C. & Smith, J. C. (2005). **Structural mechanism of the recovery stroke in the myosin molecular motor**, *Proc Natl Acad Sci U S A* **102,** 6873-6878.
10. Shih, W. M. & Spudich, J. A. (2001). **The myosin relay helix to converter interface remains intact throughout the actomyosin ATPase cycle**, *J Biol Chem* **276,** 19491-19494.
11. Sasaki, N., Ohkura, R. & Sutoh, K. (2003). **Dictyostelium myosin II mutations that uncouple the converter swing and ATP hydrolysis cycle**, *Biochemistry* **42,** 90-95.
12. Tsiavaliaris, G., Fujita-Becker, S., Batra, R., Levitsky, D. I., Kull, F. J., Geeves, M. A. & Manstein, D. J. (2002). **Mutations in the relay loop region result in dominant-negative inhibition of myosin II function in Dictyostelium**, *EMBO Rep* **3,** 1099-1105.
13. Suzuki, Y., Yasunaga, T., Ohkura, R., Wakabayashi, T. & Sutoh, K. (1998). **Swing of the lever arm of a myosin motor at the isomerization and phosphate-release steps**, *Nature* **396,** 380-383.
14. Johnson, K. A. & Taylor, E. W. (1978). **Intermediate states of subfragment 1 and actosubfragment 1 ATPase: reevaluation of the mechanism**, *Biochemistry* **17,** 3432-3442.

15. Bagshaw, C. R. & Trentham, D. R. (1974). **The characterization of myosin-product complexes and of product-release steps during the magnesium ion-dependent adenosine triphosphatase reaction**, *Biochem J* **141,** 331-349.
16. Malnasi-Csizmadia, A., Woolley, R. J. & Bagshaw, C. R. (2000). **Resolution of conformational states of Dictyostelium myosin II motor domain using tryptophan (W501) mutants: implications for the open-closed transition identified by crystallography**, *Biochemistry* **39,** 16135-16146.
17. Naber, N., Purcell, T. J., Pate, E. & Cooke, R. (2007). **Dynamics of the nucleotide pocket of myosin measured by spin-labeled nucleotides**, *Biophys J* **92,** 172-184.
18. Henzler-Wildman, K. & Kern, D. (2007). **Dynamic personalities of proteins**, *Nature* **450,** 964-972.
19. Campbell, I. D. & Dwek, R. A. (1984). ***Biological Spectroscopy*** (Benjamin-Cummings.
20. Freed, J. H. (1976). in **Spin labeling: theory and applications**, ed. Berliner, L. J. (Academic Press, pp. 53-132.
21. Pannier, M., Veit, S., Godt, A., Jeschke, G. & Spiess, H. W. (2000). **Dead-time free measurement of dipole-dipole interactions between electron spins**, *J Magn Reson* **142,** 331-340.
22. Fajer, P. G., Brown, L. & Song, L. (2006). ***Practical Pulsed Dipolar EPR (DEER)*** (Springer, Berlin).
23. Jeschke, G., Chechik, V., Ionita, P., Godt, A., Zimmermann, H., Banham, J., Timmel, C. R., Hilger, D. & Jung, H. (2006). *Appl. Magn. Reson.* **30,** 473-498.
24. Lakowicz, J. R. (2006). ***Principles of Fluorescent Spectroscopy*** (Springer.
25. Seidel, J., Chopek, M. & Gergely, J. (1970). **Effect of nucleotides and pyrophosphate on spin labels bound to S1 thiol groups of myosin.**, *Biochemistry* **9(16),** 3265-3272.
26. Barnett, V. A. & Thomas, D. D. (1987). **Resolution of conformational states of spin-labeled myosin during steady-state ATP hydrolysis**, *Biochemistry* **26,** 314-323.
27. Ostap, E. M., White, H. D. & Thomas, D. D. (1993). **Transient detection of spin-labeled myosin subfragment 1 conformational states during ATP hydrolysis**, *Biochemistry* **32,** 6712-6720.
28. Nesmelov, Y. E., Agafonov, R. V., Burr, A., Weber, R. T. & Thomas, D. D. (2008). **Structure and dynamics of the force generating domain of myosin probed by multifrequency electron paramagnetic resonance**, *Biophysical Journal* **accepted**.
29. Phan, B. C., Cheung, P., Stafford, W. F. & Reisler, E. (1996). **Complexes of myosin subfragment-1 with adenosine diphosphate and phosphate analogs: probes of active site and protein conformation**, *Biophys Chem* **59,** 341-349.
30. Maruta, S., Aihara, T., Uyehara, Y., Homma, K., Sugimoto, Y. & Wakabayashi, K. (2000). **Solution structure of myosin-ADP-MgFn ternary complex by fluorescent probes and small-angle synchrotron X-ray scattering**, *J Biochem* **128,** 687-694.

31. Cheung, H. C., Gonsoulin, F. & Garland, F. (1985). **An investigation of the SH1-SH2 and SH1-ATPase distances in myosin subfragment-1 by resonance energy transfer using nanosecond fluorimetry**, *Biochim Biophys Acta* **832,** 52-62.
32. Mizukura, Y. & Maruta, S. (2002). **Analysis of the conformational change of myosin during ATP hydrolysis using fluorescence resonance energy transfer**, *J Biochem* **132,** 471-482.
33. Park, S., Ajtai, K. & Burghardt, T. P. (1996). **Optical activity of a nucleotide-sensitive tryptophan in myosin subfragment 1 during ATP hydrolysis**, *Biophys Chem* **63,** 67-80.
34. Fisher, A. J., Smith, C. A., Thoden, J. B., Smith, R., Sutoh, K., Holden, H. M. & Rayment, I. (1995). **X-ray structures of the myosin motor domain of Dictyostelium discoideum complexed with MgADP.BeFx and MgADP.AlF4**, *Biochemistry* **34,** 8960-8972.
35. Bauer, C. B., Holden, H. M., Thoden, J. B., Smith, R. & Rayment, I. (2000). **X-ray structures of the apo and MgATP-bound states of Dictyostelium discoideum myosin motor domain**, *J Biol Chem* **275,** 38494-38499.
36. Dominguez, R., Freyzon, Y., Trybus, K. M. & Cohen, C. (1998). **Crystal structure of a vertebrate smooth muscle myosin motor domain and its complex with the essential light chain: visualization of the pre-power stroke state**, *Cell* **94,** 559-571.
37. Holmes, K. C. (1998). **Muscle contraction**, *Novartis Found Symp* **213,** 76-89; discussion 89-92.
38. Manstein, D. J., Titus, M. A., De Lozanne, A. & Spudich, J. A. (1989). **Gene replacement in Dictyostelium: generation of myosin null mutants**, *Embo J* **8,** 923-932.
39. Schroder, R. R., Manstein, D. J., Jahn, W., Holden, H., Rayment, I., Holmes, K. C. & Spudich, J. A. (1993). **Three-dimensional atomic model of F-actin decorated with Dictyostelium myosin S1**, *Nature* **364,** 171-174.
40. Shih, W. M., Gryczynski, Z., Lakowicz, J. R. & Spudich, J. A. (2000). **A FRET-based sensor reveals large ATP hydrolysis-induced conformational changes and three distinct states of the molecular motor myosin**, *Cell* **102,** 683-694.
41. Ritchie, M. D., Geeves, M. A., Woodward, S. K. & Manstein, D. J. (1993). **Kinetic characterization of a cytoplasmic myosin motor domain expressed in Dictyostelium discoideum**, *Proc Natl Acad Sci U S A* **90,** 8619-8623.
42. Bobkov, A. A., Sutoh, K. & Reisler, E. (1997). **Nucleotide and actin binding properties of the isolated motor domain from Dictyostelium discoideum myosin**, *J Muscle Res Cell Motil* **18,** 563-571.
43. Liang, W. & Spudich, J. A. (1998). **Nucleotide-dependent conformational change near the fulcrum region in Dictyostelium myosin II**, *Proc Natl Acad Sci U S A* **95,** 12844-12847.
44. Sleep, J. A., Trybus, K. M., Johnson, K. A. & Taylor, E. W. (1981). **Kinetic studies of normal and modified heavy meromyosin and sto even ubfragment-1**, *J Muscle Res Cell Motil* **2,** 373-399.

45. Werber, M. M., Peyser, Y. M. & Muhlrad, A. (1992). **Characterization of stable beryllium fluoride, aluminum fluoride, and vanadate containing myosin subfragment 1-nucleotide complexes**, *Biochemistry* **31,** 7190-7197.
46. Woodward, S. K., Geeves, M. A. & Manstein, D. J. (1995). **Kinetic characterization of the catalytic domain of Dictyostelium discoideum myosin**, *Biochemistry* **34,** 16056-16064.
47. Reynoso, J. R., Jr., Bobkov, A., Muhlrad, A. & Reisler, E. (2001). **Solution properties of full length and truncated forms of myosin subfragment 1 from Dictyostelium discoideum**, *J Muscle Res Cell Motil* **22,** 657-664.
48. Van Dijk, J., Furch, M., Derancourt, J., Batra, R., Knetsch, M. L., Manstein, D. J. & Chaussepied, P. (1999). **Differences in the ionic interaction of actin with the motor domains of nonmuscle and muscle myosin II**, *Eur J Biochem* **260,** 672-683.
49. Kuhlman, P. A. & Bagshaw, C. R. (1998). **ATPase kinetics of the Dictyostelium discoideum myosin II motor domain**, *J Muscle Res Cell Motil* **19,** 491-504.
50. Thomas, D. D., Ramachandran, S., Roopnarine, O., Hayden, D. W. & Ostap, E. M. (1995). **The mechanism of force generation in myosin: a disorder-to-order transition, coupled to internal structural changes**, *Biophys J* **68,** 135S-141S.
51. Urbanke, C. & Wray, J. (2001). **A fluorescence temperature-jump study of conformational transitions in myosin subfragment 1**, *Biochem J* **358,** 165-173.
52. Himmel, D. M., Gourinath, S., Reshetnikova, L., Shen, Y., Szent-Gyorgyi, A. G. & Cohen, C. (2002). **Crystallographic findings on the internally uncoupled and near-rigor states of myosin: further insights into the mechanics of the motor**, *Proc Natl Acad Sci U S A* **99,** 12645-12650.
53. Takagi, Y., Shuman, H. & Goldman, Y. E. (2004). **Coupling between phosphate release and force generation in muscle actomyosin**, *Philos Trans R Soc Lond B Biol Sci* **359,** 1913-1920.
54. Korman, V. L., Anderson, S. E., Prochniewicz, E., Titus, M. A. & Thomas, D. D. (2006). **Structural dynamics of the actin-myosin interface by site-directed spectroscopy**, *J Mol Biol* **356,** 1107-1117.
55. Nesmelov, Y. E., Agafonov, R. V., Burr, A. R., Weber, R. T. & Thomas, D. D. (2008). **Structure and dynamics of the force-generating domain of myosin probed by multifrequency electron paramagnetic resonance**, *Biophys J* **95,** 247-256.
56. Squier, T. C. & Thomas, D. D. (1989). **Selective detection of the rotational dynamics of the protein-associated lipid hydrocarbon chains in sarcoplasmic reticulum membranes**, *Biophys J* **56,** 735-748.
57. Lanzetta, P. A., Alvarez, L. J., Reinach, P. S. & Candia, O. A. (1979). **An improved assay for nanomole amounts of inorganic phosphate**, *Anal Biochem* **100,** 95-97.
58. Fiske, C. H. S., Y (1925). **The calorimetric determination of phosphorus**, *J Biol Chem* **LXVI,** 375-400.
59. Baker, J. E., Brust-Mascher, I., Ramachandran, S., LaConte, L. E. & Thomas, D. D. (1998). **A large and distinct rotation of the myosin light chain domain occurs upon muscle contraction**, *Proc Natl Acad Sci U S A* **95,** 2944-2949.

60. Yengo, C. M., Chrin, L. R., Rovner, A. S. & Berger, C. L. (2000). **Tryptophan 512 is sensitive to conformational changes in the rigid relay loop of smooth muscle myosin during the MgATPase cycle**, *J Biol Chem* **275,** 25481-25487.
61. Agafonov, R. V., Nesmelov, Y. E., Titus, M. A. & Thomas, D. D. (2008). **Muscle and nonmuscle myosins probed by a spin label at equivalent sites in the force-generating domain**, *Proc Natl Acad Sci U S A* **105,** 13397-13402.
62. Milov, A. D., Ponomarev, A. B. & Tsvetkov, Y. D. (1984). **Electron-Electron Double Resonance in Electron Spin Echo: Model Biradical Systems and the Sensitized Photolysis of Decalin**, *Chem. Phys. Lett.* **110,** 67-72.
63. Lakowicz, J. R., Gryczynski, I., Wiczk, W., Laczko, G., Prendergast, F. C. & Johnson, M. L. (1990). **Conformational distributions of melittin in water/methanol mixtures from frequency-domain measurements of nonradiative energy transfer**, *Biophys Chem* **36,** 99-115.
64. Cecchini, M., Houdusse, A. & Karplus, M. (2008). **Allosteric communication in myosin V: from small conformational changes to large directed movements**, *PLoS Comput Biol* **4,** e1000129.
65. Malnasi-Csizmadia, A., Pearson, D. S., Kovacs, M., Woolley, R. J., Geeves, M. A. & Bagshaw, C. R. (2001). **Kinetic resolution of a conformational transition and the ATP hydrolysis step using relaxation methods with a Dictyostelium myosin II mutant containing a single tryptophan residue**, *Biochemistry* **40,** 12727-12737.
66. Velapoldi, R. A. & Tonnesen, H. H. (2004). **Corrected emission spectra and quantum yields for a series of fluorescent compounds in the visible spectral region**, *J Fluoresc* **14,** 465-472.
67. Morris, C. A., Coureux, P.-D., Wells, A. L. & Sweeney, H. L. (2006). **Structure-Function Analysis of Myosin II Backdoor**, *to be published*.
68. Chisholm, R. L., Gaudet, P., Just, E. M., Pilcher, K. E., Fey, P., Merchant, S. N. & Kibbe, W. A. (2006). **dictyBase, the model organism database for Dictyostelium discoideum**, *Nucleic Acids Res* **34,** D423-427.
69. Gasteiger, E., Gattiker, A., Hoogland, C., Ivanyi, I., Appel, R. D. & Bairoch, A. (2003). **ExPASy: The proteomics server for in-depth protein knowledge and analysis**, *Nucleic Acids Res* **31,** 3784-3788.
70. Jorgensen, W. L., J., C., Madura, J. D., Impey, R. W. & Klein, M. L. (1983). **Comparison of simple potential functions for simulating liquid water**, *J Chem Phys* **79,** 926-935.
71. Phillips, J. C., Braun, R., Wang, W., Gumbart, J., Tajkhorshid, E., Villa, E., Chipot, C., Skeel, R. D., Kale, L. & Schulten, K. (2005). **Scalable molecular dynamics with NAMD**, *J Comput Chem* **26,** 1781-1802.
72. Martyna, G. J., Tobias, D. J. & Klein, M. L. (1994). **Constant pressure molecular dynamics algorithms**, *J. Chem. Phys* **101,** 4177-4189.
73. Feller, S. E., Zhang, Y., Pastor, R. W. & Brooks, B. R. (1995). **Constant pressure molecular dynamics simulation: The Langevin piston method**, *J. Chem. Phys* **103,** 4613-1621.
74. Andersen, H. C. (1983). **RATTLE: a "velocity" version of the SHAKE algorithm for molecular dynamics calculation**, *J. Comp. Phys* **52,** 952-962.

75. Humphrey, W., Dalke, A. & Schulten, K. (1996). **VMD: visual molecular dynamics**, *J Mol Graph* **14,** 33-38, 27-38.
76. Yengo, C. M., De La Cruz, E. M., Chrin, L. R., Gaffney, D. P., 2nd & Berger, C. L. (2002). **Actin-induced closure of the actin-binding cleft of smooth muscle myosin**, *J Biol Chem* **277,** 24114-24119.
77. Negrashov, I. V., Nesmelov, Y. E., Gillispie, G. & Thomas, D. D. (2009). **Transient time-resolved fluorescence: subnanosecond-resolved photophysics and submillisecond-resolved biochemistry**, *submitted to RSI*.
78. Gyimesi, M., Kintses, B., Bodor, A., Perczel, A., Fischer, S., Bagshaw, C. R. & Malnasi-Csizmadia, A. (2008). **The mechanism of the reverse recovery step, phosphate release, and actin activation of Dictyostelium myosin II**, *J Biol Chem* **283,** 8153-8163.
79. Kovacs, M., Malnasi-Csizmadia, A., Woolley, R. J. & Bagshaw, C. R. (2002). **Analysis of nucleotide binding to Dictyostelium myosin II motor domains containing a single tryptophan near the active site**, *J Biol Chem* **277,** 28459-28467.
80. Kintses, B., Yang, Z. & Malnasi-Csizmadia, A. (2008). **Experimental investigation of the seesaw mechanism of the relay region that moves the myosin lever arm**, *J Biol Chem* **283,** 34121-34128.
81. Reubold, T. F., Eschenburg, S., Becker, A., Kull, F. J. & Manstein, D. J. (2003). **A structural model for actin-induced nucleotide release in myosin**, *Nat Struct Biol* **10,** 826-830.